DEFECT ENGINEERING FOR SILICON PHOTONIC APPLICATIONS

DEFECT ENGINEERING FOR SILICON PHOTONIC APPLICATIONS

by

DAVID WALTERS

B. Eng. & Mgt. (McMaster) 2004

A Thesis
Submitted to the School of Graduate Studies
in Partial Fulfilment of the Requirements
for the Degree
Master of Applied Science (M. A. Sc.)

McMaster University

MASTER OF APPLIED SCIENCE (2008) McMaster University
(Engineering Physics) Hamilton, Ontario

TITLE: Defect Engineering for Silicon Photonic Applications

AUTHOR: David Walters

SUPERVISOR: Dr. Andrew Knights

NUMBER OF PAGES: xiii, 122

Abstract

The work described in this thesis is devoted to the application of defect engineering in the development of silicon photonic devices. The thesis is divided into simulation and experimental portions, each focusing on a different form of defect engineered silicon: ion implantation induced amorphous silicon and solid-phase epitaxial regrowth suppressed polycrystalline silicon.

The simulations are directed at silicon rib waveguide Raman laser applications. It is shown that a uniform, divacancy defect concentration will not enhance Raman gain. The excess optical loss and free carrier lifetime of rib waveguides with remote amorphous silicon volumes were simulated. Net gain was demonstrated depending on the geometry of the structure. For a waveguide structure with rib width, rib height and slab height of $W = 1.5$, $H = 1.5$ and $h = 0.8$ μm respectively, the optimal separation between the edge of the rib and the amorphous region is $\sim$2.0 μm. Surface recombination velocity modification was shown to be an effective means to reduce free carrier lifetime.

Experimental work was devoted to the characterization of a novel form of polycrystalline silicon created by amorphizing the entire silicon overlayer of a silicon-on-insulator wafer. Solid-phase epitaxial regrowth of the amorphous silicon is suppressed upon annealing due to the lack of a crystal seed and results in polycrystalline silicon. This material was characterized with ellipsometry, positron annihilation spectroscopy and x-ray diffraction. The material properties are shown to be heavily dependent on the annealing conditions. Ellipsometry showed that the refractive index at 1550 nm is comparable to crystalline silicon. Positron annihilation spectroscopy showed that the polycrystalline material exhibits a high concentration of vacancy-type defects while

vertically regrown crystalline silicon does not. X-ray diffraction showed that the polycrystalline silicon is non-textured, strained in tension and is characterized by grain sizes less than 300 nm.

Defect etching and optical measurements using a waveguide geometry were performed in order to characterize the lateral regrowth and the optical loss of the polycrystalline material. Lateral regrowth in the [011] direction was 1.53 and 0.96 μm for 10 minute anneals at 750 and 900 °C respectively, and at least 2.5 μm at 650 °C. Waveguide optical loss measurements with adjacent polycrystalline regions separated from the rib by at least 5.5 μm showed no separation dependence. The intrinsic optical loss of the polycrystalline material was estimated to be 1.05 and 1.57 dB/cm for TM and TE polarizations after a 900 °C anneal. Vertically regrown *c*-Si was shown to exhibit less than 3.0 dB/cm optical loss after annealing at 550 °C.

Acknowledgements

This work has been a collaborative effort on the part of many individuals, all of which deserve mention and thanks for their valuable contribution. First, I would like to thank Dr. Andrew Knights for giving me the opportunity to pursue this work. His guidance and leadership has made it a success.

I would also like to thank the numerous staff members who helped in many aspects of the experimental portion. Doris Stevanovic and Zhilin Peng were always available and willing to help in clean-room related matters. Dr. Jacek Wojcik provided an enormous service in modeling the ellipsometer results. Graham Pearson's help was paramount in the x-ray diffraction and annealing experiments. Much of the fabrication was performed at the University of Western Ontario and the staff there deserves much thanks. Jack Hendricks and Dr. Todd Simpson were incredibly helpful for the ion implantation and silicon etching steps. Dr. Paul Coleman at the University of Bath is indebted for his positron measurements.

Thanks also go to my fellow graduate students who helped me along the way. Chris Brooks, Joel Milgram, Mike Bulk and Jon Doylend were always willing to discuss and help whenever a problem was encountered.

Finally, my parents deserve the most credit for their incredible support throughout this work.

Contents

Contents

List of Figures

List of Figures

List of Tables

List of Abbreviations

2D Two dimensional

***a*-Si** Amorphous silicon

***a*-Si:H** Hydrogenated amorphous silicon

BOX Buried oxide

BPM Beam propagation method

c*/*a Crystalline/amorphous

***c*-Si** Crystalline silicon

CMOS Complementary metal-oxide semiconductor

CVD Chemical vapor deposition

CW Continuous-wave

DLTS Deep level transient spectroscopy

EIM Effective index method

EOR End-of-range

EPR Electron paramagnetic resonance

IC Integrated circuit

III Ion implantation induced

FCA Free carrier absorption

L-SPER Lateral solid-phase epitaxial regrowth

PAS Positron annihilation spectroscopy

PECVD Plasma enhanced chemical vapor deposition

***poly*-Si** Polycrystalline silicon

RNG Random nucleation and growth

RTA Rapid thermal annealer

SEM Scanning electron microscopy

SRH Shockely-Read-Hall

SOI Silicon-on-insulator

SPER Solid-phase epitaxial regrowth

TEM Transmission electron microscopy

TIR Total internal reflection

TPA Two-photon absorption

UV Ultra-violet

VEPAS Variable energy positron annihilation spectroscopy

XRD X-ray diffraction

Chapter 1

Introduction

1.1 Silicon Photonics

Integrated optics was introduced by Miller in 1969, who realized that optical systems could take advantage of planarization in a manner similar to the microelectronics industry [1]. Curiously, the field never actively pursued devices that used the same base material and instead focused on developing alternative material systems, such as InP, GaAs, silica and lithium niobate. Silicon photonics rectifies this situation by developing integrated optical systems using processes and materials that are compatible with complementary metal-oxide semiconductor (CMOS) technology [2]. This allows current microelectronic fabrication facilities to produce integrated optical devices without significant capital costs. The last 50 years of silicon processing have created a high yield, high volume, low cost production environment, from which silicon photonics can thus reap the benefits.

Silicon-on-insulator (SOI) is the base material used in the majority of silicon photonic applications. It is a layered structure that consists of a silicon substrate with a buried oxide and top silicon film. SOI allows light to be confined and controlled in the

uppermost silicon layer. SIMOX , SmartCut® and Bond and Etch-Back are various techniques used to make SOI [3] [4] [5]. Wafers fabricated using all of these techniques have been applied in the formation of silicon photonic devices. Current trends in the microelectronics industry have required a shift to SOI from bulk silicon substrates to accommodate the need of high-speed devices [6]. This has furthered the cost-benefit of silicon photonics and has created a seamless transition for manufacturers wishing to extend their capability to include photonic functionality.

For many years, silicon was ignored by the majority of researchers as a viable option for integrated optics in favor of other materials such as lithium niobate, for its large electro-optic response, and direct bandgap semiconductors, such as GaAs, for their high optical emission efficiency. However, the need of the electronics industry to develop optical interconnects has brought about a change in attitudes. Interconnects serve as the communication pathway between components of a microelectronic system. They range in scope from those used to connect different circuit boards (inter-board) to those used within an integrated circuit (IC) (intra-chip). Optical interconnect technology is the leading candidate to replace current copper technology and allow Moore's law growth to continue. Although research is being done to improve current metal/dielectric interconnect speeds, they are predicted to be limited to data rates less than 20 Gbits/s due the finite resistance and capacitance of the lines. The International Technology Roadmap for Semiconductors (ITRS) has estimated that interconnect technology will be a limiting factor as early as 2010 [7]. If utilized, optical interconnects allow higher transmission rates and lower power consumption that will exceed interconnect requirements for the next two decades.

One of the primary benefits of silicon photonics is the ability to integrate both electrical and optical components onto a single substrate. The addition of signal processing technology to optical systems adds both functionality and cost savings. Over

the past 15 years, silicon photonics has progressed to the point where complete integration is now a reality and companies such as Kotura Inc. (who licensed Bookham Inc. Technology's silicon photonics intellectual property), Enablence Technologies Inc., and Luxtera Inc. have devices in production [8] [9] [10]. Much of the required functionality for CMOS integration has been demonstrated to date, including low-loss waveguides [11], optical couplers [12], high-speed modulators [13], detectors [14] and amplifiers [15], with the notable exception of an efficient, electrically pumped optical source.

Silicon provides an inefficient light source due to its indirect bandgap. Many novel approaches have been reported in recent years to circumvent this property which include: porous silicon, silicon nanocrystals, III-V hybridization and Raman based devices [16] [17] [18] [19]. Although much publicized, none of these approaches has met with any commercial success whether due to the lack of robustness, difficulty in electrically pumping, the failure of CMOS compatibility or the large optical pump power required.

Regardless of the need for an integrated light source, silicon photonics is being applied to many technological areas. Telecommunication applications were the initial driving force behind silicon photonics research and remain a steady source of interest. With the recent demonstration of a 40 Gb/s modulator, silicon photonics has finally reached the capabilities of the currently deployed telecommunication technology and will perhaps spur the industry to convert to silicon based devices [20]. Lab-on-a-chip and bio-sensor applications are prominent areas of research and many bio-sensing applications based on either porous-silicon or evanescent wave coupling have been demonstrated [21] [22]. Silicon photonics has the potential to have a significant impact on the world around us in the near future.

1.2 Defect Engineering

High quality silicon is a requirement for modern day electronics and the thought of deliberately introducing defects is somewhat counter-intuitive. Defects are typically assumed to be detrimental to any material and manufacturers have spent a great deal of effort understanding and minimizing those formed during device fabrication. In the previous two decades, defect engineering has emerged as an area of research that focuses on purposefully introducing and controlling defect formation for specific applications [23]. Defects can most easily be introduced via ion implantation since it is destructive by its very nature and allows accurate control of defect concentration and location.

Defects come in many forms ranging from simple point defects, such as vacancies and interstitials, to more complex ones, such as dislocation loops and grain boundaries [24]. Although studied for many years, understanding the precise nature and role these defects play can be very difficult to achieve. Defect studies typically involve correlating their effect, for example optical or electrical, to their predicted concentration and profile. Common characterization techniques include transmission electron spectroscopy (TEM), deep level transient spectroscopy (DLTS), electron paramagnetic resonance (EPR) and positron annihilation spectroscopy (PAS) [25] [26] [27] [28].

Defect engineering can be applied to a variety of situations compatible with CMOS processing. Gettering, a process used to remove impurities from the active layer, has been improved by defect engineering. For example, voids created through hydrogen implants act as sinks for some impurities [29]. Also, shallow junctions, a requirement for continued device scaling, have been realized with defect engineering. By implanting a dopant into a pre-amorphized region, enhanced dopant activation can

be achieved at lower annealing temperatures [30]. Further, improved switching speeds in high-power diodes and a reduction of free body effects in transistors fabricated in SOI have been realized by introducing defects to reduce carrier lifetime [31] [32].

Recently, several direct applications of defect engineering to silicon photonics have been developed. Most prominently, it was observed that dislocation loops enhanced the optical emission from a silicon light emitting diode (LED) [33]. This was attributed to confinement of carriers within strain fields created by the defect and a reduction of non-radiative recombination. Enhancement of absorption at the telecommunication wavelengths due to defect engineering has allowed integrated detectors to be fabricated by several groups using proton, Si^+ and He^+ implants [14] [34] [35]. Net Raman gain has been achieved in a He^+ implanted silicon waveguide due to the reduction of free carrier absorption [36]. Finally, ion implantation has been used to improve temporal response of optical modulators in a ring resonator structure [37].

Applying defect engineering to silicon photonics is not a trivial matter since it impacts both optical and electrical properties. These effects must be understood and taken into consideration for efficient opto-electronic design. Although their effect is not completely quantified, defects add another degree of freedom that engineers can use to optimize device performance. Recent speed improvements of silicon photonic devices have relied on clever structural design and have avoided the limitations of the intrinsic material. To fully utilize the bandwidth of optical telecommunications, material design will eventually be required and therefore defect engineering is expected to be a fundamental part of the future of silicon photonics.

1.3 Thesis Objective and Interest

The objective of this research is to further the understanding of defect engineering in silicon photonics. It is divided into two distinct sections. The first attempts to model the effects of defect engineering on a silicon Raman laser. The second part looks at the properties of a novel form of polycrystalline silicon (*poly*-Si), particularly suited for silicon photonic applications.

The performance of a silicon Raman laser is limited by two-photon absorption (TPA) induced free carrier absorption (FCA) [38]. Therefore it is extremely sensitive to the free carrier lifetime and typically an integrated, reverse biased *p-i-n* diode is required for gain to be achieved [39]. Defects permit lifetime engineering and potential performance enhancements. Some potential defect configurations for a rib waveguide are shown in figure 1.1. The optical and electrical characteristics of a defect engineered rib waveguide were modeled to examine the potential benefits on Raman gain. Ideally, amorphous silicon (*a*-Si) could be used for lifetime reduction due to its high defect concentration, however, its poor optical properties (i.e. high loss and refractive index) prevent its use without careful consideration. Understanding and balancing the electrical and optical impact defects have on a rib waveguide is critical for optimizing device performance. Using defects potentially offers fewer processing steps, zero-power functionality and improved performance of silicon Raman lasers.

To alleviate the constraints imposed by the optical properties of *a*-Si, a novel *poly*-Si fabrication process was devised, the idea being that it would maintain a high defect concentration and low carrier lifetime but would have optical properties much closer to crystalline silicon (*c*-Si). This required determining the properties of ion implantation induced (III) *a*-Si and solid-phase epitaxial regrowth (SPER) suppressed *poly*-Si. This type of *poly*-Si has received little attention from the academic community and

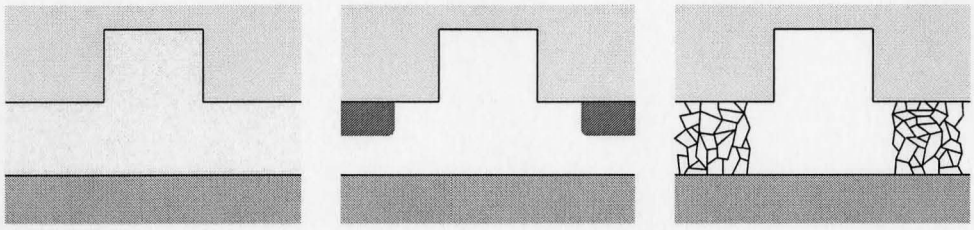

Figure 1.1: Possible structures for a defect engineered rib waveguide utilizing a uniform point defect distribution (left), remote *a*-Si volumes (centre) and adjacent *poly*-Si regions (right).

is a novel material for silicon photonic applications. It is created by completely amorphizing the top layer of SOI and annealing at a sufficiently high temperature to induce recrystallization. Figure 1.2 illustrates the process and the different possible regrowth mechanisms. Depending on the amorphization process, the recrystallization is either mediated through SPER or random nucleation and growth (RNG) and results in either regrown crystalline silicon or *poly*-Si. By masking the amorphization implant and annealing, regions of *poly*-Si can form adjacent to *c*-Si.

The interest in this material system and process is three-fold. First, the process itself is elegant in its simplicity. The relatively low temperatures required for regrowth make it amenable to device processing. More importantly, it allows *a*-Si and *poly*-Si to be used without a deposition step. This is beneficial because device topology remains unchanged, it reduces processing steps, and allows the fabrication of devices that could not be realized otherwise. The second area of interest arises from the uniqueness of the SPER suppressed *poly*-Si material system. Because the material is *pure* and only contains impurities from the original SOI, it allows fundamental study of a wide array of subjects such as grain growth kinetics, grain boundary properties, electrical conduction, and dopant diffusion; all of which are dependent on impurity/dopant concentration and are very important to the semiconductor community. The final area of interest in *a*-Si and *poly*-Si arises from the need for silicon photonics to develop

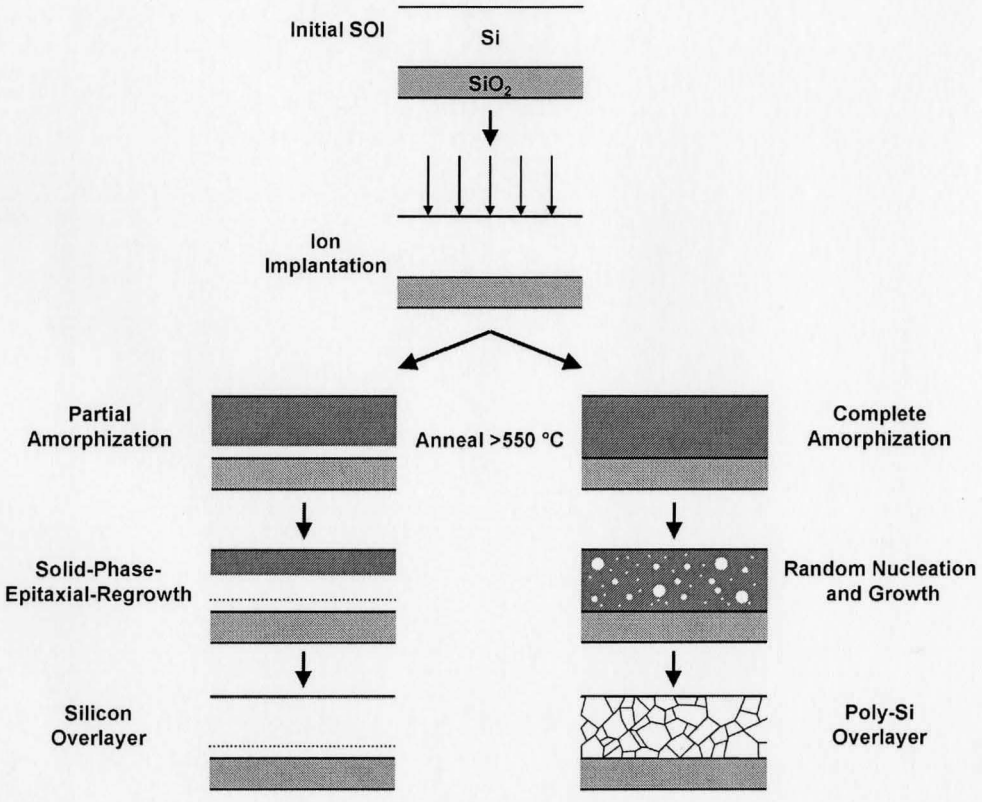

Figure 1.2: Fabrication process of SPER suppressed *poly*-Si. The regrowth process, mediated through SPER or RNG, depends on the completeness of the amorphization step.

fast modulators and detectors. Due to the lack of a linear electro-optic effect in unstrained silicon, modulators are commonly based on the thermo-optic effect and plasma dispersion effect. The speed of these modulators are essentially dictated by material properties (i.e. thermal conductivity and free carrier lifetime). Only with innovative thinking and unique device design have modulator speeds reached 40 Gb/s [20]. However, the next generation of high-speed modulators for optical interconnect applications will virtually be impossible to fabricate without the use of defect engineering and low free carrier lifetime materials such as *a*-Si and *poly*-Si.

1.4 Thesis Outline

Chapter 2 of this work focuses on the pertinent background information. First, ion implantation, damage creation and amorphization are discussed. The properties of *a*-Si and *poly*-Si are reviewed as well as the basics of recrystallization and solid-phase epitaxial regrowth. Finally, basic optical waveguide theory and computational methods are examined so that the ramifications of applying *a*-Si and *poly*-Si to silicon photonic devices can be understood.

Modeling and simulation results for the silicon Raman laser are described in chapter 3. It begins by providing background information on the Raman effect and silicon Raman lasers. Two cases are examined that use defect engineering in an attempt to improve Raman laser performance. Optical simulation results performed with BeamPROP are given and compared with modeling using the Effective Index Method (EIM). Carrier lifetime is modeled for a defect engineered rib waveguide using both analytical and simulation based approaches. Based on the optical loss and carrier lifetime simulations the Raman gain of a defect engineered waveguide is estimated.

Chapter 4 describes the experimental methods, procedures and results for the characterization of ion implantation induced *a*-Si and *poly*-Si. Defect etching, ellipsometry, positron annihilation spectroscopy (PAS) and X-ray diffraction (XRD) are all used to examine the properties of the *a*-Si and *poly*-Si material. The application of *poly*-Si and *a*-Si to rib waveguides is qualitatively discussed.

Chapter 5 focuses on possible future work and applications as well as providing a summary and some concluding remarks.

Chapter 2

Background Theory

2.1 Ion Implantation

Ion implantation is an essential process for CMOS device fabrication and has been used over the past 30 years to electrically dope semiconductors. It has dominated over diffusion based doping methods since it can produce shallower junctions with higher impurity concentrations; an essential criteria for small scale devices. Although commonly associated with electrical doping, ion implantation can also be used for other applications since it can affect many material properties such as the refractive index, optical absorption, surface hardness, surface roughness and thermal conductivity [40].

2.1.1 Fundamental Concepts

At its heart, ion implantation is a destructive process. Accelerated ions impinge on a target and cause damage as they randomly scatter off atoms in the target material. This damage can be repaired, typically through an annealing process in the range of 800-1100 °C. An implantation step is primarily described by two key parameters: dose and energy. Dose refers to the areal density of impurity ions introduced and varies

widely, between 1×10^{11} to 1×10^{17} cm^{-2}, depending on the specific application. The implant energy refers to the energy of the accelerated ions and determines the depth to which an ion can travel in the target. Values can range from 1 keV to several MeV depending on the required application, yielding approximate implantation depths in the range of 1 to 5000 nm [41].

From an atomic perspective, ion implantation simplifies to a mechanical collision problem and can be modeled by determining the contributions of the individual interactions. This is accomplished by determining the energy loss rate of an ion, termed the stopping power, which is given by [41]

$$\frac{dE}{dx} = -N[S_n(E) + S_e(E)] \tag{2.1}$$

where N is the target atomic density, $S_n(E)$ is the contribution due to nuclear stopping and $S_e(E)$ is due to electronic stopping. Nuclear stopping is the resulting energy loss due to elastic collisions between an ion and the core of a target atom. Electronic stopping refers to the energy loss due to the interaction between an ion and the target's electrons. This can be a local effect, resulting from a direct interaction between overlapping electron wavefunctions, or it can be non-local effect, as in the case of the drag force induced by the local electric field surrounding an ion in a dielectric. The relative contribution of each stopping power type is dependent on the ion, the target and the implant energy. The average depth of the implanted ions, termed the range, can be estimated by [41]

$$R = \int_0^{E_0} dx = \frac{1}{N} \int_0^{E_0} \frac{dE}{S_n(E) + S_e(E)} \tag{2.2}$$

where E_0 is the implant energy. Figure 2.1 shows the electronic and nuclear stopping

power for 500 keV implants of He^+, Si^+ and Xe^+ into silicon as a function of depth. The lightest ion, He^+, loses most of its energy through electronic stopping, whereas heavier ions tend to lose it through nuclear stopping. Nuclear stopping is most efficient at low ion velocities due to the longer interaction times between an ion and a target atom. This results in a peak stopping power that occurs slightly before the estimated ion range. The large difference between the nuclear stopping power of light and heavy ions will significantly change the damage profile and therefore the choice of implantation species is a critical parameter in damage and defect studies.

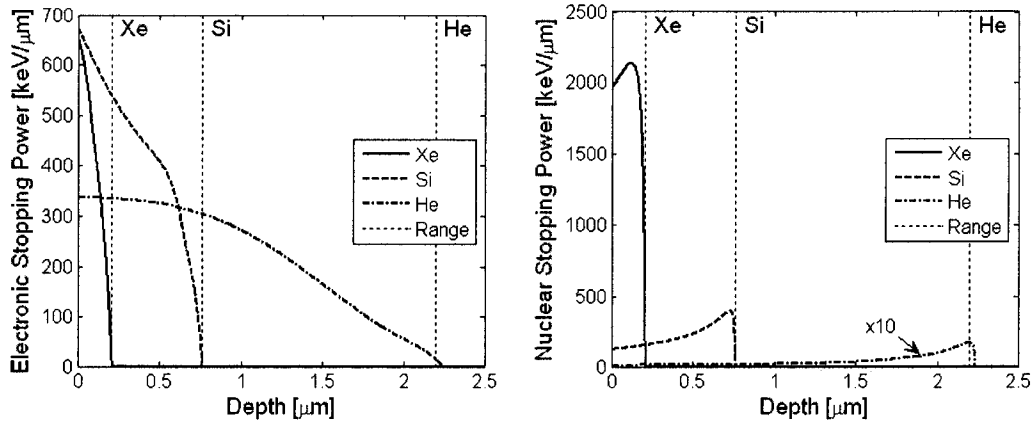

Figure 2.1: Electronic (left) and nuclear (right) stopping power as a function of depth for a 500 keV implant of He^+, Si^+ and Xe^+ into Si. Also shown is the predicted ion range for each implant. Generated using SRIM and equation 2.1 [42].

The large number of ions implanted allows statistical methods (recall the lowest dose is 1×10^{11} cm^{-2}) to describe the resulting concentration profile. Range and straggle are the most commonly used parameters. As previously mentioned, range is the average penetration depth for a collection of ions with a given energy, while straggle refers to the standard deviation or spread of ions around this value. The kurtosis and the skewness are higher order moments of the distribution that refer to the peakedness and asymmetry of the profile respectively. Monte Carlo techniques that take into account more complex interaction phenomena can also be used for

implant simulation when statistical methods cannot be applied, such as in the case of ion channeling.

Channeling is an effect observed in crystalline materials. The lattice structure creates clear pathways for ions to travel along, with few nuclear collisions, which results in a profile distorted from simple statistical distributions. Channeling is mitigated by tilting the sample to minimize the number of ions entering a channel at shallow angles or by depositing a thin, typically 20 nm, screen oxide that serves to scatter ions in random directions as they first enter the sample [43].

2.1.2 Damage Production

Damage production is the primary disadvantage of using ion implantation over other doping technologies. Although annealing can recover most of the damage, it comes at the cost of diffusion and dopant profiles are modified from their as-implanted states. Implantation damage in crystalline materials has many forms but common to each is a distortion of lattice.

The bulk of implantation damage is created via nuclear collisions that cause target nuclei to be displaced. This process can create a stable vacancy and an interstitial, also called a Frenkel pair [44]. For silicon, the energy required is typically quoted as 15 eV [45].

The relatively high energy used for implantation when compared to the threshold energy for Frenkel pair production, means that a single ion can cause thousands of displacements as it travels through the target material. In a nuclear collision, energy is transferred between ion and target. If the ion energy is large enough, sufficient energy can be transferred to the target atom such that it can displace other target atoms. This process can continue and is referred to as a cascade. For heavy ion

implants, a single ion will thus leave behind a wake of damage much larger than it could produce on its own.

Figure 2.2 shows the simulated damage and defect concentration profile for a Si^+ implant with energy=500 keV and dose=1×10^{15} cm^{-2}. Several key features can be observed. First, lattice damage can saturate at high doses owing to the fact that the number of displacements is equal to the target atomic density. This implies that higher doses will only serve to increase the width of the saturation region and not produce further damage. Secondly, the saturated damage region occurs before the peak of the Si^+ profile. This corresponds to the previously mentioned peak in the nuclear stopping power. The figure also shows that an excess of vacancies exists near the surface, while an excess of interstitials remain beyond the range.

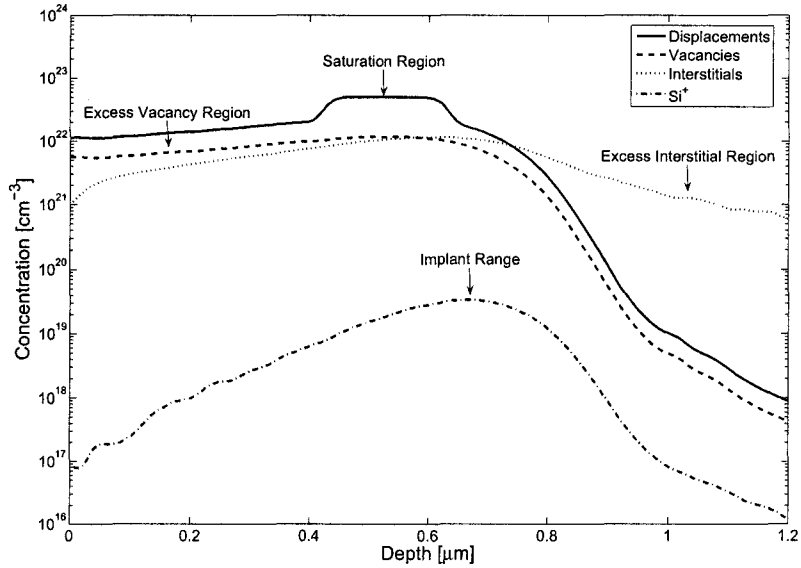

Figure 2.2: Displacement, vacancy, interstitial and Si^+ concentration profile simulated using SILVACO for a Si^+ implant into Si with energy=500 keV and dose=1×10^{15} cm^{-2}.

Damage production is affected by the temperature of the substrate during implantation and the pre-existing damage level of the target. The lack of thermal equilibrium

in an implanted material means that defects will tend to migrate. This is most apparent for isolated vacancies and interstitials during room temperature implants due to their relatively high mobility. Annihilation of vacancies and interstitials with each other and isolated point defects at the target's surface will result in a reduction in damage retention. Target temperature significantly changes the diffusivity of defects and therefore low temperature implants are used to maximize retained damage. High energy implants with high beam currents can induce a large amount of sample heating and careful temperature control is required to avoid self-annealing effects. Damage introduction is also dependent on the level of pre-existing damage. A dramatic rise in damage accumulation occurs as one goes to higher implant doses. This is explained by a reduction in threshold energy due to the damage, stress, and impurity related effects that occur as an implantation progresses [40].

2.1.3 Ion Implantation Induced Defects

Damage is often referred to as primary or secondary. Primary damage is the direct result of ion implantation whereas secondary damage occurs after annealing. Primary damage, with the exception of high dose effects, tends to be more local and usually includes point defects and defect clusters. Secondary damage can be localized, in the form of defect-impurity complexes, or broad, in the case of extended defects like dislocation loops.

Defect concentration and defect type are significantly affected by the implanting species. For this study, self-irradiated silicon was chosen to eliminate any possible chemical effects in the observed results. Some of the defects produced by this implant are vacancies, divacancies, vacancy clusters consisting of three of more vacancies, interstitials and di-interstitials [26]. Impurity related defects, due to the carbon,

oxygen and initial doping of the silicon, often appear in the form of oxygen-vacancy complexes, divacancy-oxygen complexes, carbon-oxygen-vacancy complexes, as well as others [26]. Besides the wide array of defect types, each particular defect may have different charge states and different energy levels within the bandgap. Table 2.1 lists some of the most common defects along with their energy levels and required annealing temperature to remove them. Annealing a damaged material provides thermal energy to allow defects to diffuse, dissociate, annihilate and recombine. Defect clusters tend to dissociate into point defects and annihilate with other point defects or at sinks. Implantation induced voids are also possible with a high energy Si^+ implant due to the large physical separation between the vacancy-rich and interstitial-rich regions that prevents recombination [46].

Table 2.1: Common implantation induced point defects in silicon.

Name	Charge State	Energy Level(s) [eV]	Annealing Temperature [°C]
Vacancy	V^{--}	E_c-0.11	Present above
	V^-	E_c-0.57	-273 [41]
	V^+	E_v+0.05	
	V^{++}	E_v+0.13	
Divacancy	V^{--},V^-	E_c-0.24	300-350 [31]
	V^-,V^0	E_c-0.43	
	V^0,V^+	E_v+0.20	
Vacancy Cluster	V_4,V_5	E_c-0.43	450-500 [31]
Oxygen-Vacancy	OV^0	E_c-0.169	250-300 [31]
Oxygen-Divacancy	V_2O	E_c-0.43	275-355 [31]
Carbon-Oxygen-Vacancy	$COVV^0$	E_v+0.35	400-450 [31]

Although typically associated with damage reduction, annealing can also cause implantation defects to evolve, particularly into so-called $\langle 311 \rangle$ defects. In principle, annealing an implanted sample will remove most of the excess vacancy/interstitial point defects and clusters. However, the implanted ions themselves will act as inter-

stitials and conglomerate on the ⟨311⟩ plane to form rod-like clusters during annealing [47]. For low dose implants these rods tend to dissolve at reasonably high annealing temperatures. At higher doses and higher damage levels, the rods will evolve into stable dislocation loops that can significantly affect device performance.

2.1.4 Ion Implantation Induced Amorphization

Damage in ion implanted crystalline materials can accrue to the point where long range order of the crystal lattice is no longer preserved. This is a commonly used description of the amorphous phase. For silicon, this would mean that the atoms would maintain four nearest neighbours (on average), however the bond angles would be significantly distorted and other bond types (i.e. floating and dangling) would be more prevalent than found in *c*-Si [48].

The mechanism behind ion-beam induced amorphization is still subject to debate. For the most part, two models seem to dominate: homogeneous and heterogenous amorphization. Homogeneous amorphization refers to the uniform accumulation of stable defects until a critical point is reached. Heterogenous amorphization is caused by the creation of small amorphous pockets. Total amorphization then proceeds by the overlapping of a large number of amorphous regions or by the growth of a small number of pockets that eventually coalesce. Experimental results seem to validate both models depending on the implant conditions. Light ions that tend to produce point defects result in a homogeneous mechanism, whereas heavier ions tend to trigger heterogeneous amorphization [48]. Amorphization of silicon with a Si^+ implant is considered to follow the homogeneous model [49].

Knowing the point at which the crystalline to amorphous transition occurs is critical to optimize implant conditions and minimize defect formation in non-amorphous

regions. Also, the annealing and damage recovery behaviour is distinctly different for highly damaged silicon and *a*-Si, with the former requiring higher annealing temperatures to reduce defects to the same extent as found in regrown *a*-Si [41]. With this in mind, many authors have expressed an amorphization threshold in terms of defect concentration. Table 2.2 lists the more common criteria and their values for amorphizing silicon. Since defect production is heavily dependent on implant parameters, a more universal criterion is the energy deposited by the implanted ions. The critical energy represents the energy required to induce a phase transformation. By defining a critical energy, the critical dose, Φ, is calculated by [48]

$$\Phi = \frac{E_c}{E_{dep}} \tag{2.3}$$

where E_c is the critical energy [eV/cm^3] and E_{dep} is the energy deposited per unit length [eV/cm]. E_{dep} is essentially the nuclear stopping power. The critical dose is a much more practical value than the critical energy and therefore appears more often in implantation studies. As shown in figure 2.1, the nuclear stopping power varies dramatically for different ion species and also throughout the implanted volume. Using the peak nuclear stopping power, estimates of the critical dose for 500 keV He^+, Si^+ and Xe^+ implants in silicon are 2.9×10^{15}, 1.3×10^{14} and 2.4×10^{13} cm^{-2}, respectfully. In theory, these doses will only produce *a*-Si at the peak stopping power location. Higher doses will increase the width of the amorphized zone. A dose of 1×10^{15} cm^{-2} is commonly used to produce *a*-Si in many Si^+ implantation studies [50].

Beside implant species dependency, ion implantation induced amorphization is dependent on other implantation parameters such as energy, target temperature and beam current. Primarily, implant energy controls the depth of the amorphous layer

Table 2.2: Threshold criteria for amorphization of silicon.

Parameter	Value	
Energy Deposited	5×10^{23} eV cm^{-3}	[51]
Vacancy Concentration	1×10^{22} cm^{-3}	[51]
Interstitial Concentration	0.5-1.25$\times 10^{22}$ cm^{-3}	[52]
Total Point Defect Concentration	1.15×10^{22} cm^{-3}	[53]
Frenkel Pair Concentration	5×10^{21} cm^{-3}	[54]
Displacements	5×10^{21} cm^{-3}	[55]
Divacancy/Di-interstial pairs	1×10^{22} cm^{-3}	[48]

and allows for the formation of both continuous and buried a-Si regions. Energy has little effect on the amorphization threshold although some minor dependence was observed based on ion mass due to the differences in electronic stopping power [56]. Temperature effects alter critical dose because dynamic annealing occurs as previously described in section 2.1.2. For light ions, a critical temperature exists above which amorphization cannot occur regardless of dose. For a Si^+ implant, temperature effects on critical dose are minimal below 0 °C [57]. Related to this effect is the change in threshold due to ion beam current. A higher beam current results in a smaller critical dose due to the prevention of dynamic annealing. However, at low temperatures beam current has little effect [57].

2.1.5 End-of-Range Defects

Although damage production occurs throughout the implanted volume, particular attention is given to those formed beyond the range, termed End-Of-Range (EOR) defects. Typically, the most concerning EOR defects are extended defects, such as $\langle 311 \rangle$ interstitial clusters and dislocation loops, which form after annealing. In amorphized silicon, these defects are significant since they are predominant in concentration after solid-phase epitaxial regrowth of the a-Si region [41].

Some differences exist between the formation of extended defects in SOI and those

formed in bulk silicon. This is caused by the buried oxide (BOX) which acts as a sink for interstitials and reduces the concentration of interstitials and dislocation loops by at least an order magnitude in SOI relative to bulk silicon [58]. This effect is primarily governed by the proximity of the EOR region to the Si/SiO_2 interface and requires at least 15% of the dose to be implanted into the BOX [58]. Also, it has been shown that the amorphizing species can impact the EOR defects. Larger mass ions result in a reduction in EOR defects due to their lower straggle and higher fraction of nuclear energy deposited versus lighter ions [59].

2.2 Properties of Disordered Materials

Many properties of semiconductors are the direct result of the crystal lattice. Disturbing this periodicity with defects can cause serious modifications to the semiconductor's behaviour. In this work, the materials of interest are *c*-Si, *poly*-Si and *a*-Si, which are schematically shown in figure 2.3. These three solid phases of silicon have distinctly different properties that cover a wide range of values. Crystalline and amorphous silicon lie at opposite ends of the disordered spectrum, whereas *poly*-Si can behave similar to either one depending on its microstructure. By understanding the origin of these changes, materials can be tailored for specific applications.

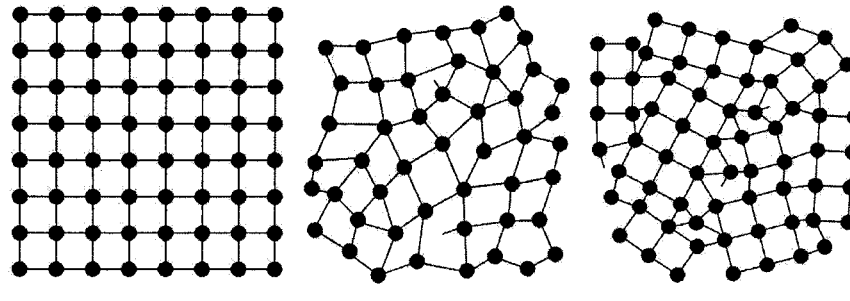

Figure 2.3: Schematic of *c*-Si (left), *a*-Si (middle) and *poly*-Si (right). Adapted from [60].

2.2.1 Phase Definition

Before discussing the details and properties of each material, it helps to define what constitutes each phase. In section 2.1.4, amorphous materials were described as having no long range order but a limited order at short range. This is evident in figure 2.3 where most atoms in the amorphous structure have four nearest neighbours, however dangling, floating and distorted bonds limit the long range order. This long vs. short range order definition of the amorphous phase leaves a wide margin for interpretation when trying to define whether a material is amorphous. How can we distinguish between highly damaged material and amorphous material? In general, authors have defined the amorphous phase with reference to a particular property under investigation (e.g. refractive index, density, etc.) [40]. As the material undergoes a phase transition, the measured change will typically follow an S-like behaviour and initially undergo slow changes, followed by a fast transition and finally saturation. The point at which saturation occurs is defined as the amorphization point. To complicate matters, it has been shown that both different material properties and different measurement techniques saturate at different values yielding no absolute amorphous definition [40] [61]. It is even possible to observe Si nanocrystals (10 - 20 Å in size) using TEM in ion implanted silicon for doses well above the critical threshold dose [62].

For many applications, the distinction between highly damaged and amorphous materials is practically irrelevant as long as the material behaves as desired. However, from a scientific perspective, the lack of a distinct definition provides uncertainty when comparing results from other institutions, measurement techniques or fabrication processes. The a-SOI material system used in this study allows a unique definition of amorphous material since it is binary in nature. By implanting and

damaging the top layer of a SOI substrate, the material phase can be defined based on its regrowth properties. As discussed in section 2.3, by annealing the damaged material and determining whether it is crystalline or polycrystalline, the disordered state of the initial silicon layer can be determined. For a silicon overlayer that is heavily damaged but not completely amorphous, solid-phase epitaxial regrowth will result in the reconstruction of the crystalline material. For layers that are completely amorphous, SPER will be suppressed and the annealing step will induce regrowth via a random nucleation and growth model. This results in the formation of a *poly*-Si layer. This definition of the amorphous phase is preferred because i) it is binary in nature and has no phase transition region, ii) it is based directly on the structural disorder of the material and not on a correlated value (i.e. defect density, optical absorption, etc.), and iii) it ensures a complete distribution of amorphous material and not a large number of amorphous pockets.

Regardless of the definition of the amorphous phase, experiments indicate that there are two types of *a*-Si: as-implanted (that formed immediately following ion implantation) and relaxed. The relaxed variety results from a low temperature anneal that is believed to allow bond rearrangement and defect annihilation, although it yields no change in material density [48]. Annealing between 300-500°C induces this relaxed phase [48].

Between the two phases of perfect crystallinity and complete disorder, lies a third solid phase of silicon: polycrystalline. *Poly*-Si is an agglomerate of *c*-Si volumes, called grains or crystallites, that are clustered together. It is commonly characterized by the grain size and texture. Grain size can vary from the nano-scale to the micro-scale and is usually reflected by its name (i.e. nano-crystalline, micro-crystalline, etc.). The crystal fraction represents the ratio of crystalline material to amorphous material. Texture refers to the distribution of grain orientations. If there is a propensity for

grains to be oriented along a particular crystallographic plane, the material is said to be textured. Although difficult to quantify, the grain boundary is also a critical property of *poly*-Si that can alter optical, electrical and chemical behaviour [41].

2.2.2 Fabrication of *a*-Si and *poly*-Si

Detailing the exact properties of *a*-Si and *poly*-Si is difficult since it is heavily dependent on the fabrication process. The most common methods used are various forms of chemical vapor deposition (CVD) and r.f. sputtering [41]. Deposition temperature is typically used to govern the solid-phase of the film; low temperatures for *a*-Si, high temperatures for *poly*-Si. By default, the process incorporates impurities into the film; some of which are desired, as in the case of hydrogenated *a*-Si, while others are not, such as oxygen due to chamber contamination.

Fabrication of ion implanted *a*-Si was described in section 2.1.4. In the current work, a Si^+ implant was used to amorphize silicon to minimize impurity effects. A benefit of using the *a*-SOI system is that the *a*-Si and *poly*-Si formed are relatively pure and contamination is dominated by the impurities in the initial SOI substrate and not the fabrication process. This gives the material consistency over many fabrication runs and allows impurity related effects to be measured in a controlled manner since they can also be introduced through ion implantation. Other group-IV elements have been used to amorphize silicon and no structural (i.e. density and dangling bond density) differences were reported when compared to those formed via self-irradiation [63].

2.2.3 Optical Properties

Refractive Index

For integrated optics applications, the refractive index is a critical parameter that determines the fundamental guiding properties of the device. It is a frequency dependent property that relates the electronic response of a material to an applied electromagnetic field. For telecommunication applications, the typical wavelength of interest is 1550 nm, for which the refractive index of *c*-Si is 3.48 [64].

In general, the refractive index of *a*-Si is higher than *c*-Si. Exceptions to this rule are due to microstructure (i.e. voids) and impurity related effects (i.e. *a*-Si:H) [65]. Spectroscopic ellipsometry results from Fried *et al.* indicate that the origin of the index difference is the structural disorder of the amorphous state and a concomitant change in the bandstructure of the material [66]. Comparing as-implanted and relaxed *a*-Si samples it was estimated that disorder was reduced by 1.5%, which explains the lower refractive index of the relaxed state. Other postulated causes for the index change include the photo-refractive effect and the increase in polarizability of dangling bonds. The photo-refractive effect can be discarded as the origin of this increase since the density of the amorphous phase is actually lower than that of the crystalline phase and would therefore be expected to yield a lower index [48]. The increased dangling bond polarizability density was discounted since it required the polarizability to increase by a factor of 2500; a physically unreasonable value [63]. Disorder is therefore the most likely cause of refractive index modification in *a*-Si.

The refractive index of *a*-Si and *poly*-Si is heavily dependent on the fabrication process. Deposited films can vary significantly depending on the deposition temperature and impurities within the film. For example, the index of *a*-Si:H can vary from 4.5 to 2.5 at 2.5 μm for a hydrogen content of 0% to 60% [65]. For *poly*-Si, the values

also span a large range, reported to be between 3.83 to 4.87 at 632.8 nm depending on the deposition parameters [67][68].

The refractive index of ion implanted *a*-Si differs from deposited films in that the microstructure of the amorphous phase is much less dependent on process parameters and therefore more reproducible. Estimated refractive indices for as-implanted and relaxed *a*-Si at 1550 nm are 3.90 and 3.75 [63] [69]. de Dood *et al.* have explicitly stated the value for relaxed *a*-Si at 1550 nm to be 3.73 [70]. The refractive index value of *a*-Si has been shown to be independent of the implant species used to form the amorphous layer, at least for other group IV ions and noble gases [63] [71].

Optical Absorption

Optical absorption in *c*-Si at the telecommunication wavelengths is relatively small due to its 1.11 eV bandgap [41]. Common absorption mechanisms for silicon are shown in figure 2.4 and include interband, free carrier, defect and two-photon absorbtion.

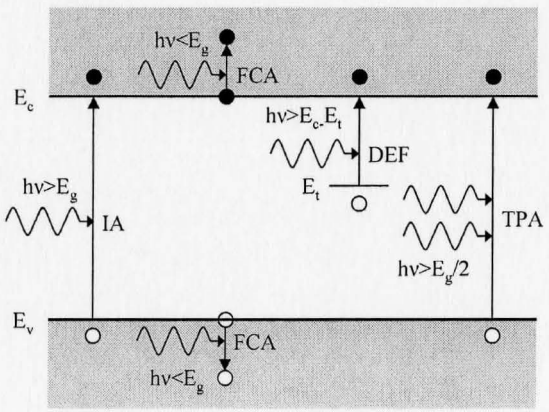

Figure 2.4: Absorption mechanisms in crystalline and defected silicon include interband absorption (IA), free carrier absorption (FCA), defect absorption (DEF) and two-photon absorption (TPA).

Interband or band-to-band absorption results in the transition of an electron from the valence band to the conduction band. For crystalline silicon, this mechanism is

negligible for photons with energies less than the bandgap. In amorphous materials, the lack of long-range order makes the concept of bandstructure and a bandgap somewhat tenuous, however a-Si is still usually described as having a bandgap. The most commonly used definition is given by the Tauc formula [72]

$$\alpha E = K(E - E_G)^2 \tag{2.4}$$

where α is the optical absorption, E is the energy of the incoming photon, K is a constant and E_G is the optical or Tauc bandgap. Plotting $(\alpha E)^{1/2}$ vs. E, gives E_G as the x-intercept of a linear fit. The bandgap for ion implanted a-Si is thus determined to be $\sim 1.2-1.3$ eV, whereas for a-Si:H it is $\sim 1.5-1.7$ eV [73]. Interband absorption in a-Si is higher than c-Si near the bandedge due to the presence of a large number of extended band tail states [74].

Free carrier absorption, or intraband absorption, results in the promotion of conduction(valence) band electrons(holes) to higher energy levels. Also called the plasma dispersion effect, free carriers affect both the real and imaginary component of the refractive index. This is the basis for many modulators in silicon. The increased absorption in a semiconductor can be estimated using the Drude model given by [75]

$$\Delta\alpha = \frac{e^3\lambda_0^2}{4\pi^2 c^3 \epsilon_0 n}\left(\frac{\Delta N_e}{\mu_e m_e^{*2}} + \frac{\Delta N_h}{\mu_h m_h^{*2}}\right) \tag{2.5}$$

where e is the electric charge, λ_0 is the wavelength of light, c is the speed of light, ϵ_0 is the permittivity of free space, n is the refractive index of silicon, ΔN_e and ΔN_h are the excess electron and hole concentrations, μ_e and μ_h are the electron and hole mobility, m_e^* and m_h^* are the conductivity effective mass of the electrons and holes. Although this results in values in reasonable agreement with observation, Soref *et al.*

empirically defined excess absorption at 1550 nm based on experimental results as [75]

$$\Delta\alpha = \Delta\alpha_e + \Delta\alpha_h = 8.5 \times 10^{-18}\Delta N_e + 6.0 \times 10^{-18}\Delta N_h \tag{2.6}$$

Free carrier effects are negligible in low-doped silicon and are primarily of concern for devices using integrated *p-i-n* diodes.

In defected materials, trap-assisted or defect absorption can be severely detrimental. Defects in the crystal lattice create energy levels within the bandgap. This allows electronic transitions (i.e. absorption) with sub-bandgap photon energies. For defect rich and amorphous silicon, this will cause significant absorption depending on the concentration and energy level of the traps as well as the wavelength of the light.

For silicon photonic applications the most prominent defect is the divacancy, which has an absorption peak at 1.8 μm [76]. In dose dependent studies, the divacancy concentration has been shown to saturate at $\sim 2.8\times10^{14}$ cm^{-2} leading to a divacancy concentration of $\sim 10^{20}$ cm^{-3} [73]. This saturation effect was attributed to a quenching of divacancies, which at higher concentrations interact to form clusters and other complexes that have different optical properties than a single, isolated divacancy. It should be noted that although divacancy attributed absorption saturates and decreases at high doses, total absorption continually increases [77]. Empirically, the optical loss due to the divacancy has been thoroughly analyzed by several authors [78][79]. At 1550 nm, the excess loss due to divacancies, α_{def}, is given by [78]

$$\alpha_{\text{def}} = \frac{4.34 \times N_t}{7.7 \times 10^{16}} \text{ [dB/cm]} \tag{2.7}$$

where N_t is the divacancy concentration.

Two-photon absorption is (as the name suggests) the simultaneous absorption

of two photons, a phenomenon which allows the absorption of sub-bandgap light. It is not usually associated with integrated optical devices except when extremely high intensities are required, as in the case of a silicon Raman laser. Two-photon absorption is proportional to the intensity of the light and is given by $\Delta\alpha_{TPA} = \beta_{2P} I$, where $\Delta\alpha_{TPA}$ is the increased optical absorption, β_{2P} is the two-photon absorption coefficient. For silicon, values for β_{2P} range from 0.4 to 0.9 cm/GW [38].

Poly-Si has been extensively studied as a low-cost alternative to *c*-Si and SOI. As previously mentioned, fabrication and processing have a dramatic effect on device performance. One particular study that focused on using *poly*-Si for silicon photonic applications reported optical propagation losses ranging from 9 to >40 dB/cm at 1550 nm for various annealing conditions [80]. The lowest loss waveguides resulted from a high temperature anneal at 1100 °C and hydrogen passivation. Passivation is a processing technique that introduces an impurity (often hydrogen) to terminate dangling bonds. Annealing in O_2 and N_2 ambient environments without hydrogen have been reported to result in relatively higher optical losses.

Generally, *a*-Si is not used for photonic applications due to its high bulk loss. The study by de Dood *et al.* showed that Xe^+ implant induced, relaxed *a*-Si had a loss of 115 cm^{-1} at 1550 nm [70]. No value was given for the as-implanted case. As with *poly*-Si, hydrogen passivation is commonly used to reduce the optical absorption and improve electrical performance of deposited *a*-Si. The decrease in optical attenuation is thought to originate from the reduction of disorder and strain in the *a*-Si:H film [74]. In contrast to deposited films, the implanted *a*-Si films used by de Dood did not benefit from hydrogen passivation.

2.2.4 Carrier Recombination and Lifetime

Carrier recombination refers to the self-annihilation of electrons and holes. For bulk materials the three basic mechanisms are direct, Shockley-Read-Hall (SRH) and Auger recombination. In an optical context, direct is commonly referred to as radiative since it releases a photon after recombination, while SRH and Auger are non-radiative processes.

The indirect bandgap of silicon means that direct recombination of electron-hole pairs requires a phonon to conserve momentum. This third particle makes radiative recombination an unlikely process. SRH theory postulates that defects help mediate recombination due to their energy levels that lie deep within the bandgap. These defects can originate from either impurity related (i.e. Au or Fe contamination) or structurally related (i.e. vacancy, divacancy, etc.) effects. Electrons and holes become trapped at these defect sites which facilitates the recombination process. The SRH lifetime is given by [31]

$$\frac{1}{\tau_{SRH}} = \frac{np - n_i^2}{\tau_p(n + n_i \exp(\frac{E_t - E_i}{k_B T})) + \tau_n(p + n_i \exp(\frac{E_i - E_t}{k_B T}))} \tag{2.8}$$

where n and p are the electron and hole concentrations, n_i is the intrinsic carrier concentration given by $n_i = 3.1 \times 10^{16} T^{3/2} \exp(-0.603/k_B T)$, τ_n and τ_p are the electron and hole minority carrier lifetimes, E_t is the energy level of the trap, E_i is intrinsic Fermi energy, k_B is the Boltzmann constant and T is the temperature. In thermal equilibrium, the recombination rate is zero since $np = n_i^2$. However in non-equilibrium conditions (i.e. $n = n_0 + \Delta n$), the SRH lifetime is dependent on the injection level, Δn. For the case of low-level injection (i.e. $\Delta n \ll n_0$) and n-type silicon (i.e. $n_0 \gg p_0$),

equation 2.8 reduces to [31]

$$\frac{1}{\tau_{\text{SRH-low}}} = \frac{n_0}{\tau_p(n + n_i \exp(\frac{E_t - E_i}{k_B T})) + \tau_n(n_i \exp(\frac{E_i - E_t}{k_B T}))} \tag{2.9}$$

In this case, the efficiency of recombination is governed by several factors including the energy level of the trap. The carrier lifetime is minimized when $E_t \approx E_i$ and results in $\tau_{\text{SRH-low}} \approx \tau_p$. In the case of high-level injection (i.e. $\Delta n \gg n_0, n_i \exp(\frac{E_t - E_i}{k_B T}), p_0, n_i \exp(\frac{E_i - E_t}{k_B T})$), equation 2.8 reduces to [31]

$$\tau_{\text{SRH-high}} = \tau_n + \tau_p = \frac{1}{\sigma_n \nu_{th,n} N_t} + \frac{1}{\sigma_p \nu_{th,p} N_t} \tag{2.10}$$

where $\sigma_{n,p}$ are the capture cross-sections of the electrons and holes, $\nu_{th,n,p}$ are the thermal velocities and N_t is the trap concentration. Using the SRH model in the high-injection case, the carrier lifetime is independent of the trap energy level and is determined solely by the trap concentration and capture cross-section.

Finally, Auger recombination occurs when the energy resulting from the electron-hole recombination is transferred to another free carrier in the form of kinetic energy. Auger recombination becomes apparent at high carrier concentrations (e.g. $> 10^{18}$) since this process requires the third body to be relatively close to the recombination site.

The density of states in amorphous materials is commonly modeled using two exponential tails at the bandedges, known as Urbach tails, and two mid-gap Gaussian distributions [81]. This is described in figure 2.5. The mid-gap states are attributed to defects such as dangling bonds. The mobility gap, which is close to the optical bandgap defined using the Tauc formula (see equation 2.4), separates the regions of low and high mobility, or alternatively localized vs. extended states. Due to the

localized nature of electrons in trap states, conduction in an amorphous material at low temperatures is mediated through variable range hopping [81]. This conduction mechanism involves an electron in a localized state *jumping* to a nearby state by absorbing a phonon. Even though termed the high mobility region, the extended states of a-Si have a mobility of $\sim$6 cm^2/Vs whereas the value for c-Si is $\sim$500-1300 cm^2/Vs depending on doping levels [82]. For a-Si, the high concentration of defects greatly reduces the carrier lifetime. Experimentally determined values for as-implanted and relaxed a-Si are 0.8 and 9 ps respectively [83]. This density of states

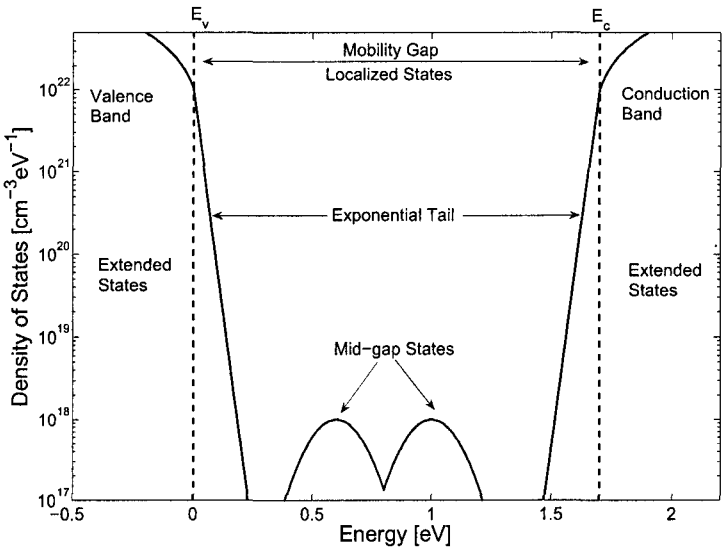

Figure 2.5: Density of states for an amorphous material.

model can also be applied to *poly*-Si, although the magnitude of defect states is comparatively smaller than for a-Si. The lower defect density means longer lifetimes should be expected. The majority of recombination occurs at highly defective grain boundaries that largely consist of dangling bonds [84]. An estimated carrier lifetime for small-grain *poly*-Si (i.e. grain size $\sim$100nm) is $\sim$0.1 ns, although it is heavily dependent on the fabrication process [85]. These lifetimes are considerably shorter

than in bulk silicon, where they usually range between 1-20 μs.

The carrier lifetime of thin films can differ significantly from the bulk material due to recombination at layer interfaces. In SOI, both the Air/Si surface and Si/SiO_2 interface can reduce carrier lifetime. Most interfaces are a source of dangling bonds, traps and defects that act as recombination centers in a manner similar to the previously described SRH model. The quality of an interface is commonly described by its surface recombination velocity. An interface that results in no excess recombination has a surface velocity of zero, whereas a surface with an infinitely large surface velocity is limited by the rate with which carriers can reach it. For a high-quality, thermally grown oxide, the surface velocity can be as low as 10 cm/s, while that of an ion-implanted surface can reach $\sim 10^6$ cm/s [86] [87]. For *poly*-Si, the grain boundaries behave similar to interfaces and modeling gives a maximum surface recombination velocity of $\sim 10^5$ cm/s for the case of low-doped silicon [88].

The effective carrier lifetime of a thin film due to both bulk and surface recombination is given by [89]

$$\frac{1}{\tau_{\text{eff}}} = \frac{1}{\tau_{\text{bulk}}} + \frac{S_1}{L} + \frac{S_2}{L} \tag{2.11}$$

where τ_{bulk} is the lifetime of the bulk material, $S_{1,2}$ are the surface recombination velocities of the interfaces and L is the film thickness. From equation 2.11 it is apparent that the surface parameters and SOI thickness are important in determining carrier lifetime and therefore the type of SOI and the fabrication processes used should be carefully chosen. The reported carrier lifetime for SIMOX wafers ranges between 0.1-1.0 μs for various overlayer thicknesses [89][90].

2.3 Regrowth Kinetics

Amorphous silicon has a greater free energy compared to its crystalline counterpart which provides a constant driving force for phase transformation. Thus, annealing amorphous materials accelerates the reversion back to the crystalline phase. This section discusses the details behind the two regrowth mechanisms presented in this study: solid-phase epitaxial regrowth and random nucleation and growth.

2.3.1 Solid-Phase Epitaxial Regrowth of Silicon

Solid-phase epitaxial regrowth (SPER) is the atomic level restructuring and conversion of an amorphous material into the crystalline phase [91]. Its primary requirement is the presence of an initial crystal, known as a seed. It acts as a nucleus for growth since the local atoms will rearrange themselves into the energetically more favorable lattice sites. Upon annealing, regrowth initiates at the crystalline/amorphous (c/a) interface and proceeds sequentially in a layer by layer manner from the seed until all amorphous material is converted or the thermal energy is used up. It can occur in both implanted a-Si or a-Si films deposited on a silicon substrate; although care must be taken to ensure no native oxide is present for deposited films. Because the amorphous material rearranges itself relative to the seed, the initial and regrown regions will have the same crystallographic orientation.

The regrowth rate or interface velocity exhibits an Arrhenius behaviour (i.e. $v = v_0 \exp(\frac{-E_a}{kT})$) [91]. In earlier works, the activation energy, E_a, for this process ranged from 2.38 to 2.9 eV [91] [92]. Recent results have yielded a value of $\sim$ 2.7 eV [93]. Figure 2.6 shows the regrowth velocity of Si^+ implant induced a-Si as a function of annealing temperature for various crystallographic directions. The Arrhenius behaviour is valid over a temperature range of 500-1400 K, although temperatures

between 550-650 °C are most commonly used to allow for well controlled regrowth [93].

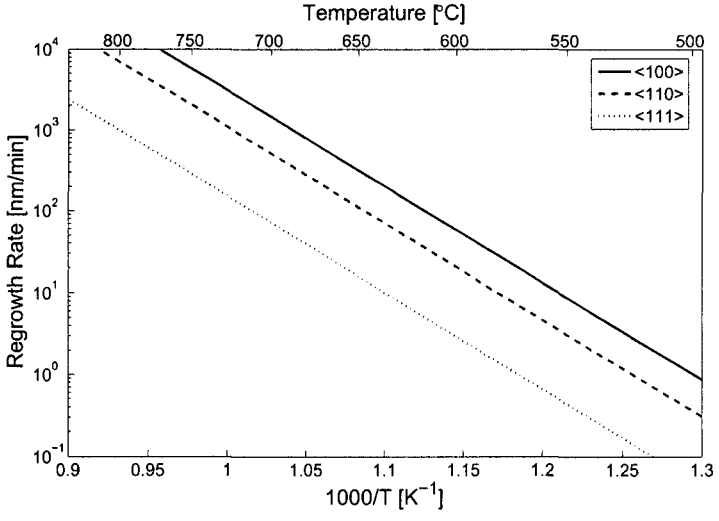

Figure 2.6: Temperature dependence of regrowth velocity for various crystallographic directions. Adapted from [91].

Regrowth in the [100] direction has the highest velocity, while growth in the [111] direction is the slowest. All other orientations fall between these two extremes. The $\langle 110 \rangle$ and $\langle 111 \rangle$ planes regrow 2.5 and 25 times slower than the $\langle 100 \rangle$ planes [48]. The activation energy of each orientation is identical, indicating that a single mechanism drives regrowth independent of crystal orientation. This mechanism is usually modeled as a simple bond breaking and rearrangement process (i.e. self-diffusion). The origin of the orientation dependence is silicon's diamond lattice structure [92]. Figure 2.7 depicts the unit cell of silicon and the restructuring order for vertical regrowth in (100) (left) and (111) (right) oriented substrates. To be considered part of the crystalline phase, an atom is required to form at least two undistorted bonds. In the case of [100] directed growth, any atom arriving at the c/a interface can easily form two undistorted bonds with the underlying crystalline material. For [111] directed

growth, it can be seen from figure 2.7 that to form two undistorted bonds requires the simultaneous arrival of 3 atoms from the amorphous phase. This multi-atom process makes [111] growth much slower than [100]. Although not shown, [110] growth requires two atoms to form crystalline material further validating this simple model of the orientation dependent rate of SPER.

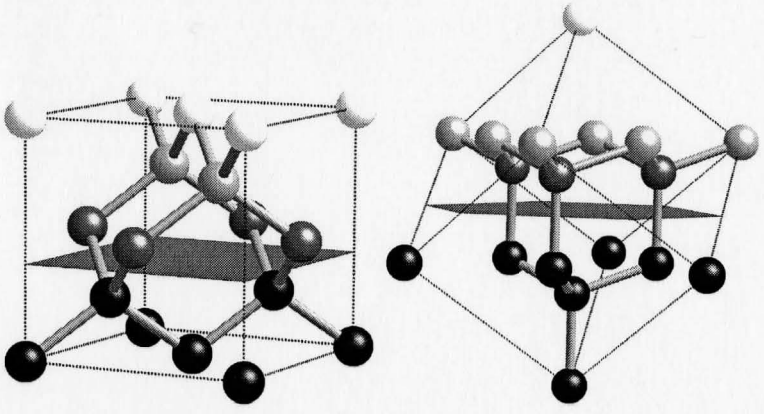

Figure 2.7: Unit cell of silicon depicting vertical regrowth for (100) (left) and (111) (right) oriented substrates. Regrowth proceeds from darkest to lightest, where black indicates atoms already positioned in the lattice.

Besides temperature and orientation, regrowth is dependent on other factors. In particular, doping type and concentration can strongly influence the regrowth rate. This dependence is important when amorphized regions are employed in the fabrication of shallow junctions. Active doping tends to increase the regrowth velocity, a phenomenon attributed to the creation of a local electric field that attracts charged defects, which in turn have been postulated to accelerate the regrowth process [94]. Inert impurities have been shown to retard the regrowth rate, particularly hydrogen, which can be unintentionally introduced by annealing the a-Si in air. The hydrogen is the byproduct of silicon oxidation with water vapour and can rapidly diffuse in silicon. Hydrogen has been shown to retard the SPER velocity by 40% [95].

The interest in, and applicability of, SPER for device applications is the direct

result of the high quality silicon that forms in the regrown region. Transmission electron microscopy studies of the regrown layer describe the regrown region as *defect free*, however it is evident from the same studies that EOR defects persist beyond the original crystalline/amorphous interface [96]. More recently, positron annihilation studies have revealed the presence of divacancy-oxygen complexes in the regrown region [97]. Further annealing resulted in the formation of higher order vacancy clusters, in particular V_6 near the EOR. Thus, the recrystallized material is not in fact *defect free*, but is characterized by vacancy-like defects and dislocations at the EOR. These results are typical of (100) oriented silicon. For (111) silicon, regrowth is characterized by a large number of microtwin defects owing to the previously described difficulty in [111] directed regrowth [98].

2.3.2 Lateral Solid-Phase Epitaxial Regrowth

In most SPER experiments, the c/a interface under study is parallel to the substrate surface since this is readily fabricated via deposition or implantation methods. However, a smaller number of investigations into SPER have looked at regrowth in both vertical and lateral directions [98] [99] [100]. There are two significant applications where lateral SPER is of interest (see figure 2.8). First, is the development of low-cost silicon devices formed from amorphous films. Second, for shallow CMOS junctions that require a pre-amorphization step, the lateral regrowth must be quantified to ensure proper placement of the doped region and optimal device performance.

The fundamental mechanism behind lateral solid-phase epitaxial regrowth (L-SPER) is identical to vertical SPER and therefore many of the underlying principles are similar. The distinction lies in the simultaneous regrowth in multiple crystallographic directions and the boundary conditions imposed by the sample. During

regrowth of an implanted junction, the c/a interfaces from each regrowth direction collide resulting in a grain boundary-like defect at the corners of the amorphous region [98]. This high defect density area is characterized by dislocation loops and prevents further regrowth at that point. Furthermore, a second high concentration of defects has been observed below the mask edges that is the result of stress from the masking film [101].

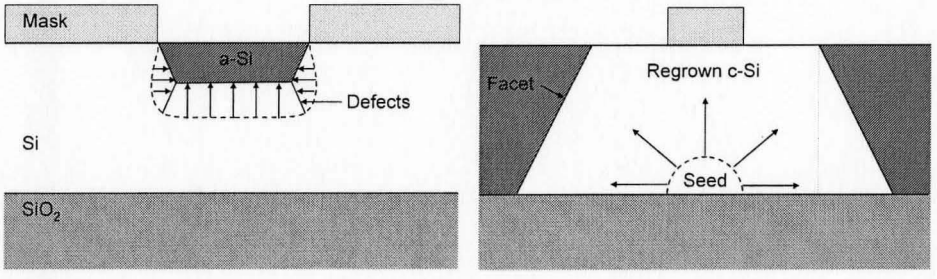

Figure 2.8: Lateral SPER for the case of an implanted junction (left) and a buried seed (right). Adapted from [98].

Unlike the previous case, regrowth of a buried seed is bounded by the upper and lower interfaces and results in some distinctive features. In particular, is the observance of facet formation at the c/a interface [102]. Faceting occurs because the bounding interfaces locally prevent SPER since the atoms cannot form two undistorted bonds. Similar to vertical SPER, the faceting is dependent on substrate orientation and lateral regrowth direction. Table 2.3 shows some possible combinations.

Table 2.3: Facet orientation for different substrate orientations and regrowth directions [102].

Substrate Orientation	Regrowth Direction	Facet Orientation
(100)	[010]	(110)
	[011]	(111)
(110)	[001]	(111)
	$[\bar{1}11]$	$(\bar{1}11)$

For (100) substrates and [011] directed regrowth, facets appear on the (111) plane, similar to the situation shown in figure 2.8 [100]. Therefore growth along the [011] direction actually occurs by [111] growth, yielding growth rates and microtwin defects comparable to the vertical case. Unfortunately, the high microtwin density due to (111) facet formation is inadequate for MOSFET devices [103]. A short, high temperature anneal (i.e. 1100 °C for 30 seconds) has been shown to effectively remove these defects [104]. Alternatively, [010] directed regrowth initially proceeds with (110) facets before transforming into the slow growing (111) facets [104]. The initial region regrown through (110) faceting produces fewer defects and well-performing MOSFET devices [103]. Undesirably for low-cost SOI applications, lateral regrowth will not proceed indefinitely. As will be discussed further below, random nucleation occurs in the *a*-Si films, generating *poly*-Si. The grain boundaries stop lateral regrowth and limit the amount of *c*-Si formed, with a maximum reported value of 44 μm for lateral regrowth [105].

2.3.3 Random Nucleation and Growth

Even without a crystal seed, recrystallization of an amorphous film can still proceed via random nucleation and growth (RNG). This method involves the spontaneous nucleation of a seed that continues to grow in a manner similar to SPER. The creation of a large number of crystal seeds means that the resulting film will recrystalize into *poly*-Si as opposed to *c*-Si.

Like SPER, RNG is understood by thermodynamic considerations. The higher free energy of the amorphous phase means that it is constantly trying to revert back to its crystalline form. So in *a*-Si, small crystals (i.e. consisting of a handful of atoms) are constantly forming. However the high surface to volume ratio prevents the majority

of these small crystals from growing due to the energy required to maintain the c/a interface. There exists a critical size ($\sim$ 1-2 nm) at which adding another atom to the cluster is energetically more favorable [106]. Thus clusters smaller than the critical size tend to shrink while those larger grow and form nanocrystals and grains.

The RNG process follows an Arrhenius behaviour and is characterized by an overall activation energy of $\sim$4 eV [93]. In thin films, nucleation can originate in the bulk or at an interface, termed homogenous and heterogeneous nucleation respectively. A study by Olsen *et al.* of *a*-Si annealed in air or in the vacuum chamber in which they were grown, revealed a higher activation energy for those exposed to air [93]. In that case, the native oxide reduced surface nucleation sites and limited nucleation to the bulk material. Other studies have selectively altered surface nucleation by using a patterned film or an ion implantation step [107]. This method allows fabrication of *poly*-Si with predetermined grain boundary locations.

The difference in activation energy between SPER and RNG processes means that at low temperatures, SPER is the dominant regrowth mechanism. At higher temperatures, each method will contribute to the regrowth of the *a*-Si film.

2.4 Optical Waveguide Theory

Optical confinement and guiding is a fundamental requirement for integrated optical devices that is accomplished by optical waveguides. Waveguides come in many forms, which include optical fibres, photonic crystals, planar slabs and three dimensional structures. Many texts have been written on the basic principles of optical waveguides and only a brief description follows, based on the works of Ref. [2] and [108].

2.4.1 Light Propagation and Maxwell's Equations

Maxwell's equations define the spatial and temporal relationship between electric fields, magnetic fields, static charge and dynamic charge. They can be used to derive the wave equation, which describes the propagation of an electromagnetic wave (i.e. light). Maxwell's equations are given by

$$\nabla \cdot \mathbf{D} = \rho \tag{2.12}$$

$$\nabla \cdot \mathbf{B} = 0 \tag{2.13}$$

$$\nabla \times \mathbf{E} = -\frac{\partial \mathbf{B}}{\partial t} \tag{2.14}$$

$$\nabla \times \mathbf{H} = \frac{\partial \mathbf{D}}{\partial t} + \mathbf{J} \tag{2.15}$$

where $\mathbf{D}$ is the electric flux density, ρ is the charge density, $\mathbf{B}$ is the magnetic field, $\mathbf{E}$ is the electric field, $\mathbf{H}$ is the magnetic flux density and $\mathbf{J}$ is the current density. For a linear, isotropic medium, the corresponding fields and flux densities are related by

$$\mathbf{D} = \epsilon_0 \mathbf{E} + \mathbf{P} = \epsilon_0 \mathbf{E} + \epsilon_0 \chi \mathbf{E} = \epsilon_0 (1 + \chi)\mathbf{E} = \epsilon \mathbf{E} \tag{2.16}$$

$$\mathbf{B} = \mu_0 (\mathbf{H} + \mathbf{M}) = \mu_0 (1 + \chi_m)\mathbf{H} = \mu \mathbf{H} \tag{2.17}$$

where ϵ_0 and μ_0 are the electric permittivity and the magnetic permeability of free space, χ and χ_m are the electric and magnetic susceptibility of the material and $\mathbf{P}$ and $\mathbf{M}$ are the electric and magnetic dipole moment. For silicon, $\mathbf{M} = 0$.

Using Maxwell's equations, the wave equation is derived in the following manner.

$$\nabla \times \mathbf{E} = -\frac{\partial \mathbf{B}}{\partial t} \tag{2.18}$$

$$\nabla \times \nabla \times \mathbf{E} = -\frac{\partial}{\partial t}(\nabla \times \mathbf{B}) \tag{2.19}$$

$$\nabla \times \nabla \times \mathbf{E} = -\mu \frac{\partial}{\partial t}(\nabla \times \mathbf{H}) \tag{2.20}$$

$$\nabla \times \nabla \times \mathbf{E} = -\mu \frac{\partial}{\partial t}(\mathbf{J} + \frac{\partial \mathbf{D}}{\partial t}) \tag{2.21}$$

By using Ohm's law, $\mathbf{J} = \sigma \mathbf{E}$, where σ is the conductivity, and applying the vector identity, $\nabla \times \nabla \times \mathbf{E} = \nabla(\nabla \cdot \mathbf{E}) - \nabla^2 \mathbf{E}$, equation 2.21 can be re-written as

$$\nabla(\nabla \cdot \mathbf{E}) - \nabla^2 \mathbf{E} = -\mu \frac{\partial}{\partial t}(\sigma \mathbf{E} + \epsilon \frac{\partial \mathbf{E}}{\partial t}) \tag{2.22}$$

For simplicity, $\rho = 0$ and $\sigma = 0$ are assumed and equation 2.12 is substituted into equation 2.22 to give the familiar wave equation,

$$\nabla^2 \mathbf{E} = \epsilon \mu \frac{\partial^2 \mathbf{E}}{\partial t^2} \tag{2.23}$$

The wave equation describes the propagation of light through a medium. Although typically described using the electric field, similar analysis can yield the wave equation in terms of the orthogonal magnetic field. The light's velocity is given by

$$v = \frac{1}{\sqrt{\epsilon \mu}} = \frac{c}{n} \tag{2.24}$$

where c is the speed of light in a vacuum and n is the refractive index of the material. The general solution of the wave equation is given by

$$\mathbf{E}(\mathbf{r}, t) = \mathbf{E}_0(\mathbf{r}, t) e^{i(\mathbf{k} \cdot \mathbf{r} - \omega t)} \tag{2.25}$$

where only the real part is considered physical. In this context, the phase ϕ of the

electromagnetic wave is $\phi = \mathbf{k} \cdot \mathbf{r} - \omega t$, where $\mathbf{k}$ is the wavevector and points in the direction of propagation with a magnitude of $k = \frac{2n\pi}{\lambda} = nk_0$, with λ being the wavelength of the light. The wavevector, the electric field and the magnetic field are mutally perpendicular. The amplitude of the field $\mathbf{E}_0$ is a function of both the position vector $\mathbf{r}(x, y, z)$ and time t. The angular frequency ω is given by $\omega = \frac{2\pi c}{\lambda}$. If we had assumed $\sigma \neq 0$ then the plane-wave solution would still exist except $\mathbf{k}$ would have an imaginary component that would correspond to the attenuation of the wave. Typically, low doped silicon is used for optical applications and the imaginary component due to the base material is negligible.

2.4.2 Planar Waveguides

A planar or slab waveguide is a layered system that forms the foundation of planar optical devices. Analysis of a simple 3 layer slab (see Figure 2.9) leads to a basic understanding of waveguide fundamentals that can be extended to more complicated situations. For all waveguides discussed here, optical guiding is based on total internal reflection (TIR), which requires $n_1 > n_0 \geq n_2$. Two approaches are usually taken to analyze the 1D system: the ray method and the wave method.

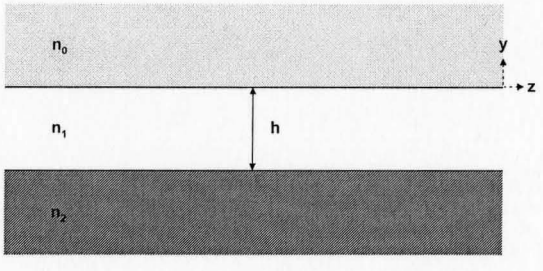

Figure 2.9: Structure of a 3-layer, planar waveguide.

The ray approach assumes that light in a waveguide can be described as a simple

ray that reflects off the interfaces as it travels along the waveguide. It is guided in the middle layer, known as the core, assuming the TIR condition is met, that is, the angle of propagation, θ, defined relative to the surface normal, is greater than the critical angle, $\theta_c = \sin^{-1}(\frac{n_{0,2}}{n_1})$. By extending the model and assuming that the ray is the direction vector of a plane wave, the ray model can be adapted to include modes.

The Fresnel equations describe the magnitude and phase of light transmitted and reflected at an interface. For rays that meet the TIR condition, a phase change will occur at each interface that is dependent on its polarization and angle of incidence. Also, while propagating through the medium, the light will undergo a phase change of $\phi = 2hn_1 \cos\theta$. In order for the wave to maintain phase along the waveguide, the total phase shift after two reflections and propagation through the material must equal $2m\pi$, where m is an integer. This results in a discrete set of propagation angles, each one being designated as a mode.

The wavevector, $\mathbf{k}$, can be broken down into its constituent components. The component aligned with the propagation direction is called β, by convention. It is defined as $\beta = n_1 \sin\theta k_0 = N_{\text{eff}} k_0$ where N_{eff} is called the effective index. The TIR condition requires $n_1 > N_{\text{eff}} > n_{2,3}$.

By using the previously derived wave equation (equation 2.23), the 3-layer system can be analyzed more rigorously in terms of the electric fields instead of a simple ray. Equation 2.23 can be simplified by assuming propagation is restricted to the z-direction and the x-direction is assumed to be infinite. Furthermore, the light is assumed to be TE polarized, meaning the electric field is limited to the x-direction (i.e. $E_{y,z} = 0$), although there is no fundamental reason why the TM case cannot be solved for in a similar manner. Using these assumptions, the wave equation can be

written as

$$\frac{\partial^2 E_x}{\partial y^2} + \frac{\partial^2 E_x}{\partial z^2} = \epsilon\mu \frac{\partial^2 E}{\partial t^2} \tag{2.26}$$

The electric field then takes the form

$$E_x = E_x(y)e^{\imath(k_z z - \omega t)} = E_x(y)e^{\imath(\beta z - \omega t)} \tag{2.27}$$

Substituting the partial derivatives of Equation 2.27 into Equation 2.26 and simplifying yields

$$\frac{\partial^2 E_x}{\partial y^2} = (\beta^2 - k^2)E_x \tag{2.28}$$

For a guided mode, the solution of 2.28 takes the form of a decaying exponential in the cladding, termed the evanescent wave, and a sinusoidal function in the core. These fields are given by

$$E_x(y) = \begin{cases} E_0 e^{-k_{y0} y}, & y \geq 0 \\ E_1 e^{-\imath k_{y1} y}, & 0 \geq y \geq -h \\ E_2 e^{-k_{y2}(y+h)}, & y \leq -h \end{cases} \tag{2.29}$$

The boundary conditions require the electric field and its derivative to be continuous. Applying these conditions to equations 2.29 and simplifying yields the eigenvalue equation

$$\tan^{-1}\left(\frac{k_{y0}}{k_{y1}}\right) + \tan^{-1}\left(\frac{k_{y2}}{k_{y1}}\right) = k_{y1}h + m\pi \tag{2.30}$$

This equation is identical to that generated by the ray model, however this method is preferred since it includes the electric field distribution and mode profiles. The number of guided modes supported by a slab is dependent on many parameters, such as the wavelength, slab thickness and refractive indices of the layers. To determine

whether a mode is supported, the cut-off condition (i.e. $\beta = \max(k_0 n_0, k_0 n_2)$) can be applied to equation 2.30. Assuming $n_2 > n_0$, the mode cut-off value is given by

$$\tan^{-1}\sqrt{a} + m\pi = \frac{2\pi h}{\lambda}\sqrt{n_1^2 - n_2^2} \tag{2.31}$$

$$\text{where } a = \frac{n_2^2 - n_0^2}{n_1^2 - n_2^2} \text{ for TE, } a = \frac{n_1^4}{n_2^4}\left(\frac{n_2^2 - n_0^2}{n_1^2 - n_2^2}\right) \text{ for TM}$$

2.4.3 Two Dimensional Confinement

Although planar waveguides allow simple design and analysis, optical confinement is restricted to a single dimension and prevents the creation of high density optical integrated circuits. To remedy this, horizontal confinement can be achieved by creating a two dimensional (2D) refractive index profile. A wide array of 2D geometries exist that have been used for integrated optics such as strip, strip-loaded, diffused, channel and rib waveguides.

The rib waveguide is one of the more popular methods used in silicon photonic applications since it is very flexible in terms of fabrication methods, waveguide geometry and optical properties. The high index contrast of the SOI system induces strong vertical confinement, whereas weaker horizontal confinement is achieved through the relatively small effective index difference between the rib and slab regions. The confinement factor describes the ratio of power in the core to the total power of the guided mode.

Modal dispersion is important in integrated optics and many devices require single-mode behaviour of the waveguide. The modal characteristics of rib waveguides have been analyzed by several authors [109][110]. The initial work of Soref *et al.* showed the possibility of large-area single-mode rib waveguides by demonstrating that higher-

order modes eventually leak into the slab region. After propagating several thousand microns, the fundamental mode is all that remains. The single-mode condition most commonly used is given by [110]

$$\frac{W}{H} \leq \frac{r}{\sqrt{1-r^2}} \tag{2.32}$$

where W is the waveguide width, H is the waveguide height and $r = \frac{h}{H}$, where h is the slab height.

2.4.4 Numerical Methods Applied to the Modeling of Rib Waveguides

Analytical solutions of Maxwell's equations are generally not possible for complex 2D and 3D geometries and approximate methods are required to determine the guiding behaviour of a waveguide. Two popular methods include the Effective Index Method (EIM) and the Beam Propagation Method (BPM).

Rib waveguides and other rectangular structures are commonly analyzed using the effective index method [111]. This method decomposes the rib structure into planar devices and allows the solutions of 1D slab waveguides to be applied to 2D problems. The solving procedure is shown in figure 2.10. The structure is laterally divided into three regions and the effective index, as defined in section 2.4.2, is determined for the vertical rib and slab sections. These values are then used to define an index profile in the horizontal direction. A final slab waveguide calculation leads to the effective index and propagation constant of the guided modes. Although the effective index method is an approximation, the coupling of the vertical and horizontal components leads to a reasonable level of accuracy for simple 2D profiles [108].

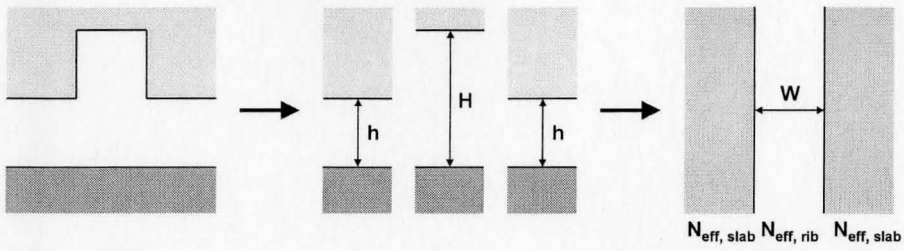

Figure 2.10: Depiction of the EIM method for a rib waveguide. First, the effective index for the vertical slab and rib region is solved, then the coupled, horizontal slab is solved.

The beam propagation method provides a simple simulation technique used to analyze 2D and 3D structure [112]. The algorithm numerically solves the 3D Helmholtz equation given by $\nabla^2 E + k^2 E = 0$. It assumes the electric field to be scalar (i.e. no polarization) and that the rapidly varying phase can be approximated by a slow-moving average function. By defining an index profile and input field, the guiding properties of the structure can be determined. However, because of the slow-varying approximation, high index contrast and wide angle structures pose problems since the refractive index changes rapidly in the propagation direction. Extensions of this basic technique have allowed polarization effects, wide-angle structures and bidirectional coupling to be taken into account.

Chapter 3

Modeling and Simulations: Towards a Defect Engineered Silicon Raman Laser

Interest in silicon photonics has dramatically increased since the first demonstration of a continuous-wave (CW) silicon Raman laser [39]. This work unequivocally confirmed optical gain and eventually lasing in silicon; an idea once thought impossible. The work in this thesis attempts to improve the performance of silicon Raman lasers by using defect engineering. In particular, two cases are examined, which are shown in figure 3.1. The first consists of a rib waveguide with a uniform defect distribution in the silicon overlayer. The second uses remote defect volumes placed adjacent to the waveguide core with varying proximity and depth. Although much of the simulation work is geared towards a Raman laser, many of the results can be used in a broader context for future silicon photonic and defect engineered applications.

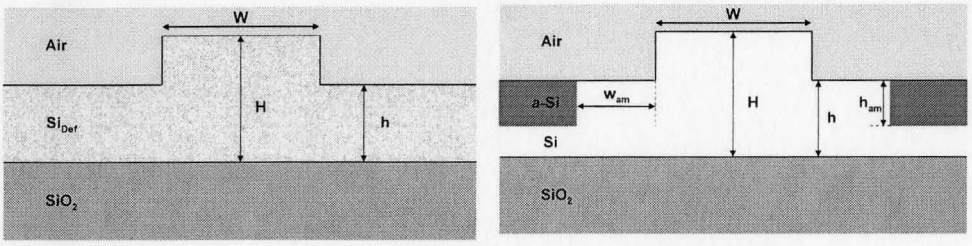

Figure 3.1: The defect engineered waveguides modeled in this analysis consist of a uniformly distributed defect concentration (left) and remote defect volumes (right).

3.1 Silicon Raman Laser Background

The physics of Raman scattering and its application to Raman lasers is well established [113] [114] [115]. The Raman effect is the result of an incident photon, referred to as the pump, inelastically scattering from an optical phonon. The emitted light is shifted in wavelength depending on whether a phonon is emitted or absorbed, termed Stokes and anti-Stokes scattering. The shifted amount is based on the material dependent optical phonon frequency. For silicon, this is 15.6 THz and results in 1434 and 1686 nm light assuming a 1550 nm optical pump. The intensity of Stokes and anti-Stokes scattering is proportional to the number of scattering centers. Since the anti-Stokes scattering requires a pre-existing phonon, it is always less intense than the Stokes line; specifically it can be calculated using Boltzmann statistics that the anti-Stokes intensity is around 8% of the Stokes intensity. For most silicon Raman applications, only the Stokes line is of concern. Stimulated Raman scattering is a nonlinear effect that results in coherent emission of scattered light and occurs when a large number of Stokes photons exist.

The Raman scattering efficiency is over four orders of magnitude stronger in crystalline silicon than silica, which allows the long, optical fibre based amplifiers used in telecommunication applications to be scaled to sizes appropriate for integrated optics [116]. For crystalline materials, the Raman scattering efficiency exhibits polarization

dependence on the pump and probe beam due to the symmetry of the lattice. Polarization selection rules for (100) oriented silicon have been worked out by Liu *et al.* and maximum efficiency is obtained when pump and probe polarizations are crossed or the waveguide is oriented in the [011] direction and both pump and probe are TE polarized [115].

Silicon-based Raman lasers have been demonstrated by several groups [39][117]. Most prominently, the group at Intel has demonstrated CW operation as well as high-speed amplification [15]. This is in contrast to the initial Raman lasers that were pulsed (thus mitigating the susceptibility to free carrier effects). Initial attempts at CW operation highlighted the dominant loss mechanism due to two-photon absorption induced free carrier absorption, which effectively quenched net gain [38]. To overcome this problem, a reverse biased *p-i-n* diode was integrated into the waveguide [39]. The electric field swept carriers from the waveguide core and allowed CW operation, however due to the large number of carriers, significant electrical power was dissipated and a saturation effect was observed due to carrier velocity limiting in high fields [118].

Defect engineering allows an alternative solution for CW Raman lasing since defects are known to reduce free carrier lifetime [31]. The method potentially allows zero-power dissipation, fewer fabrication steps and possibly an increased maximum Raman gain since large electric fields are not required. During the course of the research leading to this thesis, a group in Hong Kong observed net Raman gain in a defect engineered rib waveguide created by a low dose helium implant, however in that case a *p-i-n* diode was still required to reduce the effect of free carriers [36].

3.1.1 Carrier Recombination in a Rib Waveguide

The free carrier lifetime in a rib waveguide is distinctly different than in a planar SOI since it is a function of both the material and the device structure. This is illustrated in figure 3.2. For waveguide applications, free carrier absorption is only significant if there is overlap between the optical mode and the carrier distribution. Therefore the previously described recombination mechanisms (i.e. direct, SRH and interface) are mediated significantly by carrier diffusion. In other words, the slab region of a rib waveguide acts as a conduit for carriers to flow from the waveguide core and reduces optical absorption. The diffusion process is driven by the low carrier concentrations in regions outside the rib volume. Further, in the case of carrier generation via two-photon absorption (TPA), the highly non-uniform generation profile due to the Gaussian-like optical mode profile enhances the carrier concentration gradient.

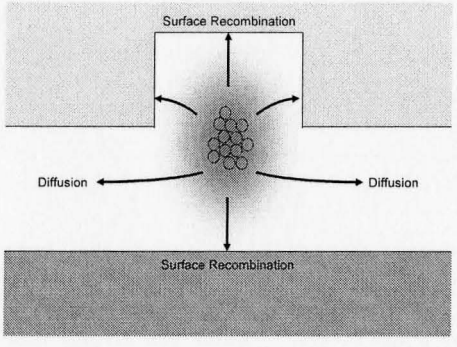

Figure 3.2: Carrier lifetime reduction mechanisms in a rib waveguide.

The silicon rib device structure has been shown to have direct implications on carrier lifetimes in silicon Raman lasers [119]. For instance, the etch depth and the size of the rib core can alter carrier lifetime. As the core size decreases, the ratio of core interface to core area increases. Thus, surface effects are enhanced and shorter lifetimes should be expected for smaller devices. The role diffusion plays is dependent on the rib etch depth since a thicker slab region allows carriers to diffuse more readily.

Reducing the slab height to negligible dimensions essentially pinches-off the diffusion process, as in the extreme case of a channel waveguide.

The role each mechanism has on reducing carrier lifetime is largely governed by the device structure and interface parameters. For small devices, interface recombination dominates due to the increased surface area to volume ratio. For large area waveguides, diffusion of carriers away from the waveguide core is more likely to be the preferred mechanism unless extreme surface recombination parameters are present.

3.2 Case 1: Uniform Defect Distribution

The initial approach modeled to reduce free carrier lifetime is the creation of a uniform defect distribution (see figure 3.1). Experimentally, this structure could be achieved using a carefully designed multiple ion implantation process and standard rib waveguide fabrication techniques. Modeling the Raman gain requires estimating both the optical and electrical effects of the applied defect distribution. For this analysis, the defects were assumed to be divacancies since they are stable at relatively high temperatures (up to ~300°C) and are well characterized with respect to their creation (i.e. implant parameters) and properties (i.e. optical and electrical effects).

Initial estimates of the impact of defects on carrier lifetimes in rib waveguides can be made by adapting the model of Dimitropoulos et al. [119]. There, an analytical solution to the steady-state continuity equation for a rib waveguide was given. An effective carrier lifetime, τ_{eff}, was defined as [119]

$$\frac{1}{\tau_{\text{eff}}} = \frac{G}{n} = \frac{1}{\tau_{\text{bulk}}} + \frac{S_{\text{Si/SiO}_2}}{H} + \frac{W + 2(H-h)}{WH} S_{\text{Air/Si}} + 2\frac{h}{WH}\sqrt{D\left(\frac{1}{\tau_{\text{bulk}}} + \frac{S_{\text{Si/SiO}_2} + S_{\text{Air/Si}}}{h}\right)} \tag{3.1}$$

where G is the generation rate, n is the carrier density, τ_{bulk} is the bulk silicon lifetime, $S_{\text{Si/SiO}_2}$ and $S_{\text{Air/Si}}$ are the surface recombination velocities at the buried oxide and air interface, D is the carrier diffusion coefficient and W, H and h are the waveguide width, height and slab height. In the case of the high carrier concentrations in Raman applications ($\sim 10^{18}$ cm^{-3}), $S \sim S/2$ and D is the ambipolar diffusion coefficient (assumed to be 16 cm^2/s) [119].

The bulk carrier lifetime in the presence of deep-level traps, τ_{def}, can be calculated using the SRH model. In the high-injection case, the carrier lifetime is independent of the trap energy level and is given by [31]

$$\frac{1}{\tau_{\text{def}}} = \frac{1}{\tau_{\text{bulk}}} + \sigma_t \nu_{th} N_t \tag{3.2}$$

where $\tau_{\text{bulk}} \approx 2.3\mu$s, $\sigma_t \approx 1 \times 10^{-16}$ cm^{-2}, ν_{th} is the thermal velocity of the carriers and N_t is the trap concentration.

Figure 3.3 shows the solution for equation 3.1 assuming waveguide dimensions of $W = 1.5$, $H = 1.5$, $h = 0.8$ with various defect concentrations and surface recombination velocities. The relative effectiveness of the defects is dependent on the surface recombination velocities. As expected, ribs with high quality surfaces are more responsive to defects since diffusion and bulk recombination play a larger role in the recombination/removal process. When the interfaces are of poor quality, the lifetime is dominated by surface effects and the relative reduction due to defects is minimal. As the defects reach high levels, the carrier lifetime approaches the lifetime of bulk silicon, indicating that bulk recombination is the limiting factor. Overall, this analysis shows that for all free carrier based devices, it is imperative to know the surface properties of the initial and processed SOI if optimal device performance and accurate simulation is to be achieved.

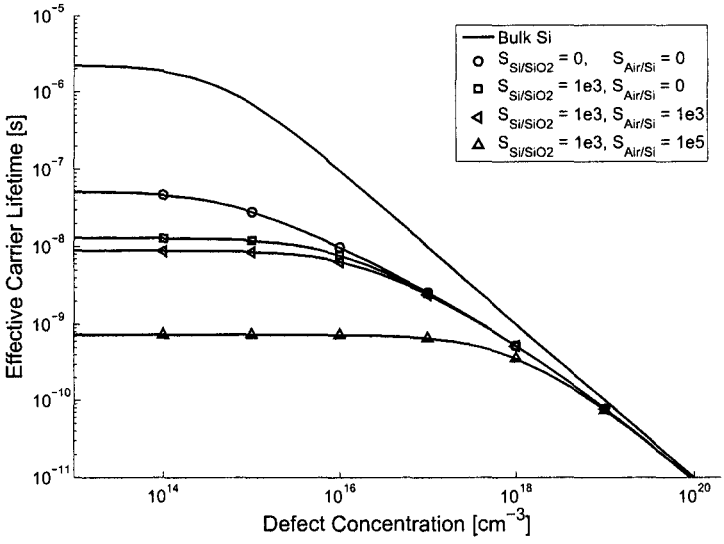

Figure 3.3: Effective carrier lifetime for a waveguide with dimensions $W = 1.5$, $H = 1.5$, $h = 0.8$ μm and various surface recombination velocities.

Ion implantation induced defects, and divacancies in particular, impair the optical properties of a waveguide. An implant process will affect both the real and imaginary components of the refractive index. In this case, the real component of the refractive index change is assumed to have negligible impact on the guiding properties due to its uniform distribution. Therefore defects are only assumed to induce optical attenuation. The excess loss due to divacancies is [78]

$$\alpha_{\text{def}} = \frac{4.34 \times N_t}{7.7 \times 10^{16}} \text{ [dB/cm]} \tag{3.3}$$

Knowing the optical and electrical effects of a uniform defect distribution, the net Raman gain of the structure can be calculated using a modified version of the model developed by Liu *et al.*[120]. The original model compared well with experimental results. It assumes the optical power of the pump and probe signals are described by a one-dimensional propagation equation. The pump power, $P(z)$, can be calculated

at a distance, z, using the following

$$\frac{dP(z)}{dz} = -\alpha P(z) - \alpha_{\text{def}} P(z) - \frac{\beta_{2P}}{A_{\text{eff}}} P^2(z) - \sigma N(z) P(z) \tag{3.4}$$

where α is the linear absorption of the waveguide, σ is the free carrier absorption cross-section, β_{2P} is the two-photon absorption coefficient, A_{eff} is the effective area of the mode and $N(z)$ is the carrier concentration.

The effective area of the optical mode is given by [116]

$$A_{\text{def}} = \frac{(\int\int |E(x,y)|^2 dxdy)^2}{\int\int |E(x,y)|^4 dxdy} \tag{3.5}$$

where $E(x,y)$ is the electric field profile of the optical mode. This was calculated using commercial software based upon the beam propagation technique.

The carrier density, $N(z)$, is given by

$$N(z) = \frac{\beta_{2P} \lambda_{\text{pump}} \tau_{\text{eff}}}{2hc} \frac{P^2(z)}{A_{\text{eff}}^2} + \frac{\alpha_{\text{def}} \lambda_{\text{pump}} \tau_{\text{eff}}}{hc} \frac{P(z)}{A_{\text{eff}}} \tag{3.6}$$

With reference to equation 3.4, the optical loss of the pump is comprised of several factors. First is the optical attenuation due to the waveguide as a result of surface roughness and scattering. For Raman applications, waveguides with losses <0.5 dB/cm are typically used [115]. Second is the excess loss due to the defects (see equation 3.3). The third and fourth terms represent the loss due to two-photon absorption and free carrier absorption, respectively. For a defect engineered rib waveguide, carriers are generated via two-photon absorption and defect absorption. These terms are reflected in the carrier density (see equation 3.6). It is assumed that all carriers can be described with the same effective lifetime regardless of the mechanism by which they were generated.

Knowing the pump power, the probe power (or Stokes power), $dP_s(z)$, can be determined using the following expression

$$\frac{dP_s(z)}{dz} = -\alpha P_s(z) - \alpha_{\text{def}} P_s(z) - \frac{2\beta_{2P} - g_r}{A_{\text{eff}}} P(z) P_s(z) - \sigma_s N(z) P_s(z) \tag{3.7}$$

where g_r is the Raman gain coefficient and σ_s is the free carrier absorption cross-section at the Stokes wavelength. Table 3.1 lists the parameters used in these simulations. The defect absorption coefficient was assumed to be equal at both pump and probe wavelengths and polarization independent.

Table 3.1: Simulation parameters in this work.

Parameter	Value	Reference
W, H, h	1.5, 1.5, 0.8 μm	
α	0.5 dB/cm	
β_{2P}	0.5 cm/GW	[115]
σ	1.45×10^{-17}cm^2	[121]
σ_s	1.71×10^{-17}cm^2	[121]
$A_{\text{eff,TE}}$	1.49 μm^2	
λ_{pump}	1550 nm	
g_r	9.5 cm/GW	[115]
τ_{eff}	see equation 3.1	

The coupled pump-probe equations were numerically solved using the parameters in Table 3.1. The peak net gain, where gain is defined as $G = 10\log(P_{\text{out}}/P_{\text{in}})$, is shown in figure 3.4 for the uniformly defected rib waveguide. Each curve represents different surface parameters and consists of two distinct regions. The high defect region, in which all curves converge, is simply the loss of the probe beam due to defect absorption. At such a high divacancy concentration, the lifetime reduction is irrelevant and the defect induced optical loss dominates. As one goes to lower defect concentrations, optical losses are reduced, carrier lifetimes rise and an improvement in net gain is observed. However, it should be noted that the net gain of a defected

waveguide never exceeds that of an intrinsic waveguide. Although the carrier lifetime could be reduced with defects, the concomitant optical attenuation mitigates any increased gain. Further, only in the case of high surface recombination velocities does net gain occur. From this analysis, it would appear that altering surface parameters is the most efficient way to improve performance assuming that optical attenuation is minimal.

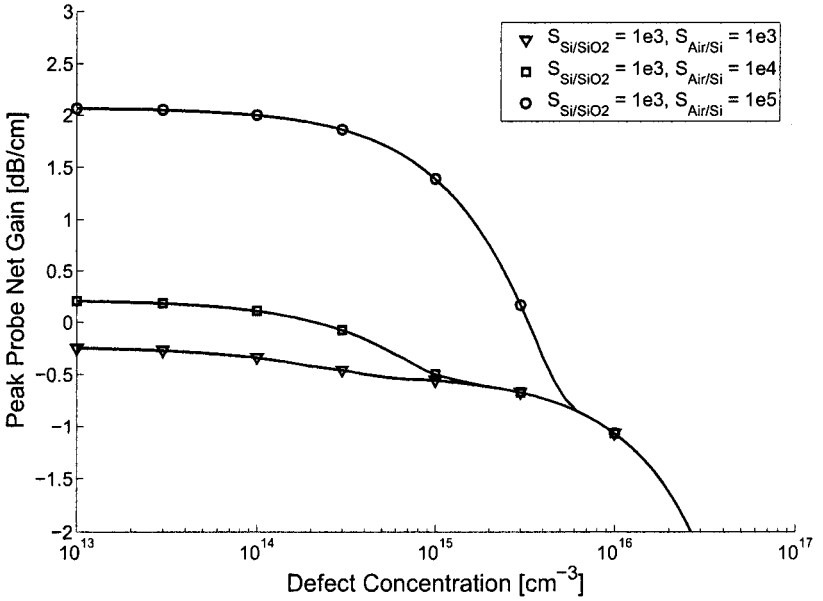

Figure 3.4: Peak probe net gain for various defect concentrations and surface recombination velocities.

3.3 Case 2: Remote Defect Volumes

The second structure examined the effect of remote defect volumes located adjacent to the rib core (see figure 3.1). In this analysis the defect volumes are assumed to be relaxed *a*-Si produced by ion implantation followed by a low temperature anneal. The principle behind this method was to maintain the low lifetime of the defected

rib, but reduce optical losses by minimizing the overlap between the optical mode and the defects. To analyze this structure, several techniques were used. From an optical standpoint, the effective index method (EIM) and beam propagation method (BPM) were used to examine the optical properties of the waveguide. The carrier lifetime could not be analyzed using the previously described analytical means, so commercial software (Silvaco) was used to calculate these values. After determining the optical and electrical properties, the results can again be applied to the coupled pump-probe equations.

3.3.1 Effective Index Method Analysis

The effective index method is a simple approach that allows quick analysis of an optical waveguide. It is valid for simple rib waveguides, however the accuracy of this technique is questionable for more complex structures and large refractive index changes [2].

Although the optical loss associated with a-Si is too high to be used as a basis for integrated optics, it can potentially be used if strategically applied in remote locations. Unlike the uniform defect case, the non-uniform perturbations of the refractive index profile of a structure with remote defective regions necessitates consideration in any optical model. The a-Si was assumed to be relaxed with a refractive index of $n_{a\text{-Si}} = 3.73$ and a loss of $\alpha_{a\text{-Si}} = 115\ \text{cm}^{-1}$ [70]. Three different waveguide structures, described in Table 3.2, were studied to observe the dependence on device geometry. The first one closely resembles the structures used by Intel for Raman laser fabrication [35]. Although, it does not meet the single-mode condition as determined by equation 2.32, it was experimentally verified to be single-mode. The two largest waveguides meet the single-mode condition.

Table 3.2: Waveguide structures used for remote defect simulations. Dimensions in microns.

Name	Width	Height	Slab Height
WG-1	1.5	1.5	0.8
WG-2	3.0	2.5	2.0
WG-3	3.0	5.0	3.0

To a first approximation, the EIM method was used to determine if a waveguide with localized a-Si regions could support guided modes. The height, $h_{a\text{-Si}}$, and proximity, $d_{a\text{-Si}}$, of the a-Si was varied. To use the EIM method the structure was reduced in a fashion similar to figure 2.10 and resulted in 3, 4 and 5-layer slab waveguides. The analytical solutions for these slab structures can be found in Ref. [108]. This structure is sometimes referred to as a 'W' waveguide due to the shape of the index profile. It can have an increased single-mode regime as well as a higher confinement factor depending on the structure [108].

With reference to the total internal reflection condition, guided modes can only be supported if the effective index of the rib region is greater than that of the 4-layer a-Si region (i.e. $n_{\text{eff,rib}} > n_{\text{eff},a\text{-Si}}$). This provides the cut-off condition for a guided mode. Considering lateral confinement in rib waveguides is weak (i.e. $n_{\text{eff,rib}} - n_{\text{eff,slab}} \approx 0$), even minor effective index changes can significantly perturb guiding. This is evident in figure 3.5, which plots the effective index of the 4-layer slab for different values of $h_{a\text{-Si}}$ and TE and TM polarizations. For comparison, figure 3.5 also shows the effective index of the 3-layer rib region. Relatively speaking, the 4-layer structure of WG-1 can support a much thicker amorphous layer due to its lower r value (i.e. $\frac{h}{H}$). For WG-2 and WG-3, there is a sudden effective index change and very little a-Si is needed to make $n_{\text{eff},a\text{-Si}} > n_{\text{eff,rib}}$.

Figure 3.6 shows the cut-off condition for guided modes in a defected rib waveguide using the EIM model. For $h_{a\text{-Si}}$ and $d_{a\text{-Si}}$ values that fall inside the cut-off value, guided

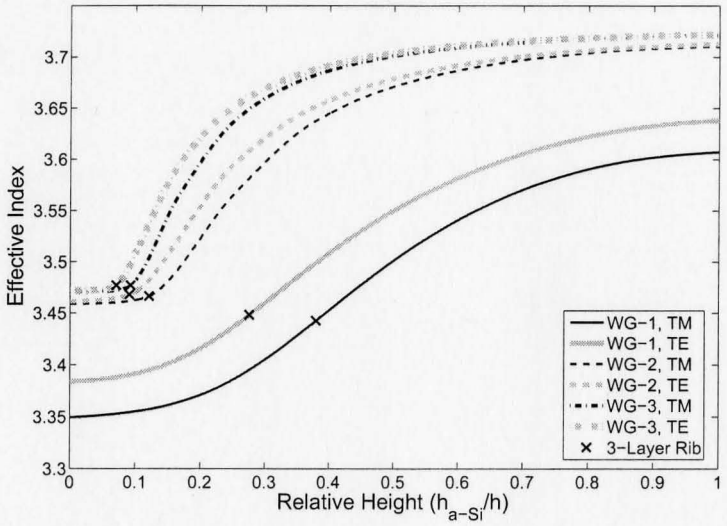

Figure 3.5: Effective index of a 4-layer slab with layers (Air/a-Si/Si/SiO_2). The effective index of the rib region, $n_{\text{eff,rib}}$, is also marked.

modes are supported. The height of the a-Si region appears to be the most critical parameter, whereas proximity has only minor influence for small $d_{a\text{-Si}}$ values. From the results of the three different structures, it is apparent that the critical waveguide parameter in determining the critical a-Si thickness is the etch depth of the rib. By etching deeper, the effective index difference between the slab and rib region increases, thus allowing thicker amorphous layers.

The results of the EIM analysis elicit a simplified approach to viewing the guiding behaviour of the waveguide with remote defect volumes. The a-Si height dependence can be understood by realizing that the a-Si region acts as a slab waveguide on its own. By approximating the 4-layer slab as an asymmetric 3-layer slab (i.e. Air/a-Si/Si) the cutoff condition for the fundamental mode is given by equation 2.31. This gives a critical amorphous thickness of 0.218 and 0.227 μm for the TE and TM modes, which coincides well with the guided mode regime shown in figure 3.6. The guiding behaviour can thus be described in two parts. For waveguides with thin amorphous

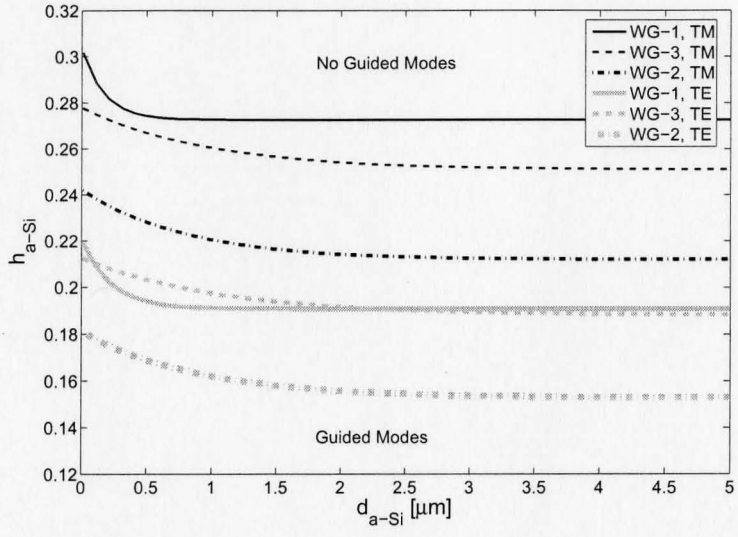

Figure 3.6: Cut-off condition for guided modes of a rib waveguide with remote defect volumes of varying height and proximity.

regions that can't support a guided mode, the excess optical loss should be relatively low and dictated by the overlap of the mode with the lossy a-Si region. Once $h_{a\text{-Si}}$ is large enough to support a slab mode, light in the rib region will couple into this mode. The proximity of the amorphous region determines the ease with which this coupling takes place. At large distances, even though guided modes are supported in the a-Si layer, low loss is expected since there is little overlap between the optical mode of the rib and the amorphous slab. According to equation 2.31, the larger Stokes wavelength should allow for a thicker a-Si region since the critical thickness is larger; possibly creating shorter free carrier lifetimes.

The EIM analysis shows that rib waveguides are very sensitive to a-Si regions. However, it should be emphasized that this method only determines the guided modes of the structure. Low-loss leaky modes have been shown to exist in the 'W'-guide that potentially can be useful for integrated optics applications [108]. Therefore, although it appears that according to the EIM analysis the use of a-Si is limited, a

more accurate simulation method that can determine the loss of the structure may yield greater insight.

3.3.2 Beam Propagation Method Analysis

As opposed to the simplified EIM analysis, the Beam Propagation Method (BPM) allows for the determination of the attenuation of guided and leaky modes. Again, the structures previously defined in Table 3.2 were used to compare the losses for differently sized waveguides. The optical parameters of the a-Si were fixed at $n_{a\text{-Si}} = 3.73$ and $\alpha_{a\text{-Si}} = 115$ cm^{-1} unless otherwise stated. The simulation was conducted by launching the fundamental mode of the undefected waveguide into the defected structure. Loss was calculated by a least-squares fit of the data to an exponential function.

The optical loss for the three structures and the corresponding TE and TM polarizations is shown in figure 3.7. In this case, the amorphous height was assumed to be equal to the slab height (i.e. $h_{a\text{-Si}} = h$). These results indicate that low-loss behaviour is possible in the defect engineered waveguide. The discrepancy between the TE and TM polarizations is a direct result of the increased confinement of the TM mode. This essentially makes coupling to the amorphous region more difficult. For silicon Raman laser applications, the excess loss must be particularly low in order to maintain net gain. Dimitropouplos *et al.* subjectively defined this as < 0.02 dB/cm [118]. For the smallest waveguide, the low-loss condition occurs when $d_{a\text{-Si}} > 2.3$ μm for the TM case and $d_{a\text{-Si}} > 3.2$ μm for the TE case. For WG-2, the required separation is 7.3 and 8.4 μm for TM and TE polarizations respectively. WG-3 requires 9.9 μm for the TM case, while the loss for TE polarization never reduced below 0.02 dB/cm within the 10 μm simulation range. The differences between structures can

be explained by the varying confinement factor.

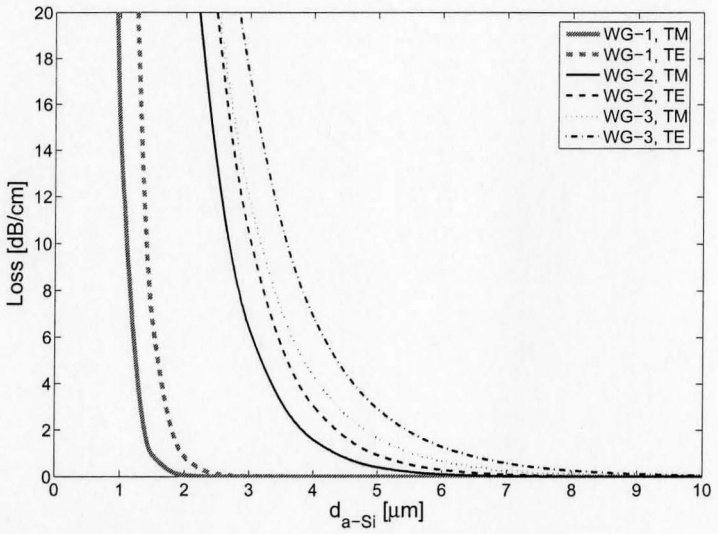

Figure 3.7: Optical loss of the TE and TM mode due to remote a-Si volumes for various waveguide dimensions in the case of $h_{a\text{-Si}} = h$.

The effect of $h_{a\text{-Si}}$ on loss was simulated using WG-1 and by assuming a constant proximity, $d_{a\text{-Si}}$ =1 μm. Figure 3.8 shows the results of the simulations. In agreement with the EIM analysis, the low-loss condition remains intact until the thickness of the amorphous region approaches that of the equivalent cutoff condition, after which the attenuation increases dramatically. Also shown in figure 3.8 is the optical loss for the Stokes and anti-Stokes wavelengths. Again, the results are in agreement with the simplified EIM approach, providing the critical thickness wavelength dependency of the a-Si layer (i.e $t_{c,1686} > t_{c,1550} > t_{c,1434}$). Once this threshold is reached, the loss has an opposite relationship with wavelength (i.e $\alpha_{1686} > \alpha_{1550} > \alpha_{1434}$), owing to the enhanced coupling efficiency at the longer wavelengths. The high loss of the TE polarization and the difference in losses between different wavelengths, allows for simple polarization and wavelength filtering applications. Although not shown, WG-2 and WG-3 have similar behaviour.

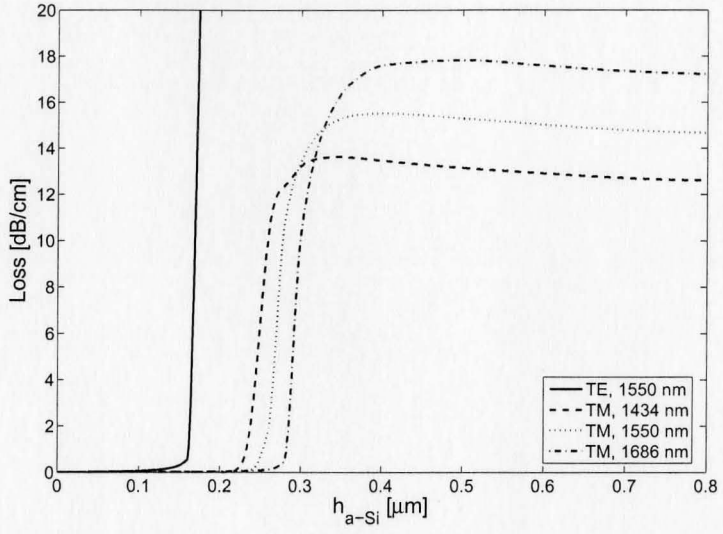

Figure 3.8: Optical loss of WG-1 due to remote a-Si volumes for different $h_{a\text{-Si}}$ values with $d_{a\text{-Si}} = 1$ μm.

3.3.3 Carrier Lifetime Simulations

For continuous-wave (CW) silicon Raman lasers, performance is limited by two-photon absorption induced free carrier absorption. The high optical intensities used in these applications can generate excess carrier concentrations on the order of $10^{17}-10^{18}$ cm^{-3} [119]. The analytical modeling of the carrier lifetime used previously cannot be applied in the case of a rib waveguide with remote defect volumes. Therefore, to estimate the effective carrier lifetime in the waveguide, Silvaco, a semiconductor device processing and testing simulator, was used.

Modeling the device consisted of defining the waveguide structure, creating a free carrier profile and determining the effective lifetime based on the simulation results. The extensive flexibility of the software allows a large number of physical parameters to be defined. The excess carriers due to two-photon absorption were simulated by defining a carrier generation rate profile. The generation rate, G, resulting from TPA

is given by

$$G = \frac{dN}{dt} = \frac{1}{2hc}\beta_{2P} I^2 \tag{3.8}$$

where N is the free carrier density, hc is the photon energy, β_{2P} is the TPA coefficient and I is the optical intensity. The intensity distribution of the mode was approximated by a Gaussian distribution with standard deviations (both height and width) that matched the actual fundamental mode. This resulted in a negligible difference from using the actual mode profile. The peak of the Gaussian distribution was chosen so that

$$G = 10^{25}\text{cm}^{-3}\text{s}^{-1} = \frac{\iint_{\text{core}} N dxdy}{W \times H} \tag{3.9}$$

This normalized the generation rate in the waveguide core for different structures. The effective carrier lifetime was then defined as the average of the electron and hole lifetimes, $\tau_{\text{eff}} = \frac{\tau_{\text{eff,e}} + \tau_{\text{eff,h}}}{2}$, where

$$\tau_{\text{eff,e,h}} = \frac{N}{G} = \frac{\iint_{\text{core}} N dxdy}{\iint_{\text{core}} G dxdy} \tag{3.10}$$

This numerical simulation allowed physical phenomena to be taken into account that were not included in the analytical model, such as Auger recombination and carrier concentration dependent mobility. The silicon was modeled as being p-type, with $p = 5 \times 10^{14}$ cm^{-3} and the buried oxide was assumed to have 1×10^{11} cm^{-2} fixed charges. While acknowledging the limitations of the analytical model, it is useful to compare the results of the analytical model and the numerical-based, Silvaco model for the undefected waveguide. The effective lifetime difference between the two methods was $< 1\%$ when surface recombination parameters, $S_{\text{Air/Si}}$ and $S_{\text{Si/SiO}_2}$, were ≥ 1000 cm/s. However, when no interface recombination was taken into account (i.e.

$S_{\text{Air/Si}} = S_{\text{Si/SiO}_2} = 0$), the numerical simulation method gave lifetimes marginally less than the analytical model. This can most likely be attributed to Auger recombination that is apparent when no surface recombination takes place and carrier concentrations are maximized.

As in the optical simulations, the a-Si was assumed to be relaxed. It was electrically modeled by a trap energy distribution consisting of two exponential tails near the bandedge and two Gaussian distributions for the mid-gap states. The parameters were chosen to match the measured results by Stolk *et al.* [83]. The mobility of the a-Si was assumed to be 20 and 1.5 $\text{cm}^2\text{V}^{-1}\text{s}^{-1}$ for electrons and holes, respectively [52]. Unless otherwise stated, the surface recombination parameters were assumed to be $S_{\text{Air/Si}} = S_{\text{Si/SiO}_2} = 1000$ cm/s. Unlike the optical simulations, very little discrepancy existed between the lifetime of TE and TM modes and so carrier generation profiles were based on the TM modes.

The effective lifetime for the three structures is shown in figure 3.9 for various $d_{a\text{-Si}}$ values (distance of the amorphous region to the waveguide edge). Again the the amorphous height is assumed to be $h_{a\text{-Si}} = h$, the height of the slab region. The lifetime reduction due to the a-Si is apparent and all waveguide lifetimes can be reduced to values less than 2 ns. Interestingly, the effects of the a-Si are far reaching and none of the waveguide structures reach their maximum lifetime even when $d_{a\text{-Si}}$ =12 μm. This effect is more pronounced in the larger waveguides that rely more heavily on diffusion for carrier removal since the a-Si regions effectively increase diffusion, through the creation of a large carrier concentration gradient.

Similar to the optical simulations, the height dependence of the amorphous silicon ($h_{a\text{-Si}}$) on carrier lifetime was modeled assuming a constant $d_{a\text{-Si}}$. The proximity was chosen so that the $\tau_{\text{eff}} \approx \frac{\tau_{\text{eff,max}}}{2}$, which resulted in $d_{a\text{-Si}} = 5, 5.5, 6\mu$m for WG-1, WG-2 and WG-3, respectively. The results are shown in figure 3.10. Unlike the optical

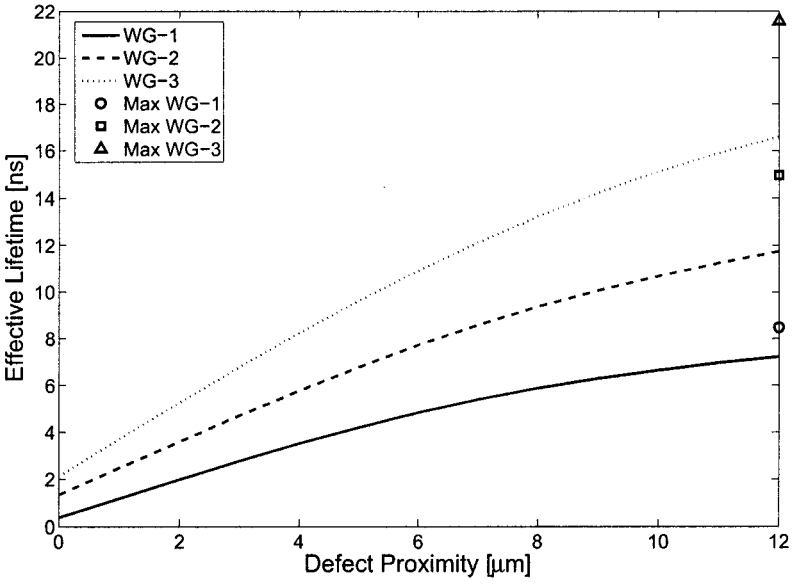

Figure 3.9: Effective lifetime due to remote a-Si volumes for various waveguide dimensions in the case of $h_{a\text{-Si}} = h$. Also shown is the maximum lifetime for an intrinsic rib waveguide.

case, the effective lifetime has very little dependency on the height of the amorphous region for all three simulated structures. The sudden rise for $h_{a\text{-Si}} \approx 0$ μm does not represent actual simulation results (i.e. a lifetime between 0 and 0.05 has not been simulated). Although a similar result is expected, simulating thin amorphous layers proved unpractical and figure 3.10 simply shows the sudden shift from a defected structure to the intrinsic waveguide.

The simulations indicate that the a-Si regions can reduce carrier lifetime in two ways. Primarily, the regions behave similar to an interface with a high surface recombination velocity. This can be seen by observing extremely high recombination rates near the interfaces and not in the bulk of the defected volume. The low mobility of a-Si and the high effective surface recombination velocity result in a low carrier concentration in the bulk of the defected volume. The concentration difference between the core and slab enhances the effects of diffusion over the intrinsic waveguide. Thus,

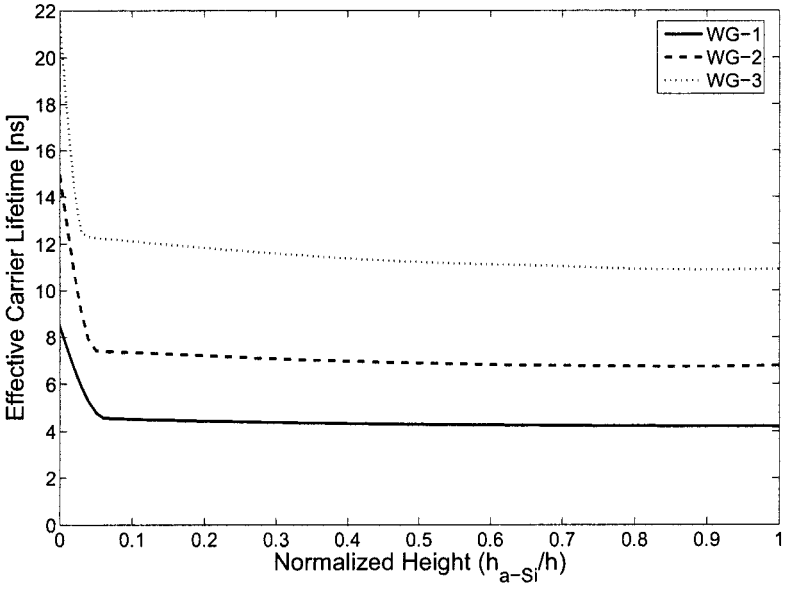

Figure 3.10: Effective lifetime due to the height of remote a-Si volumes for various waveguide dimensions. The proximity $d_{a\text{-Si}} = 5, 5.5, 6\mu$m for WG-1, WG-2 and WG-3.

lifetime reduction is accomplished directly via increased recombination which in turn enhances diffusion.

The final set of simulations examined the effect of optical pump power on carrier lifetime. The results are shown in figure 3.11 for WG-1 with $h_{a\text{-Si}} = h$ (amorphous silicon throughout the slab region) and various $d_{a\text{-Si}}$ values. The effective carrier lifetime reaches a minimum at a pump power of $\sim$0.5 W for all configurations. The initial decrease at low powers is due to the increased diffusion that occurs at higher carrier concentrations. It should be recognized that even though the carrier lifetime decreases, the carrier density continually increases since the carrier concentration is proportional to the square of the pump intensity. At high powers the lifetime increases except in the case of $d_{a\text{-Si}} = 0$ μm. This suggests that the limiting factor in lifetime reduction is not the number of trapping centers of the defected region but the rate at which carriers reach these centers. As $d_{a\text{-Si}}$ increases, the transit

time for carriers increases due to both, the increased distance and reduced diffusion resulting in higher carrier concentrations and increased lifetimes. The insensitivity of the lifetime to $h_{a\text{-Si}}$ also reflects this phenomenon. Although beyond the scope of this study, further carrier lifetime reduction can likely be obtained if remote defect volumes are combined with a reverse biased, integrated *p-i-n* diode so that carriers can be swept to the recombination centers faster.

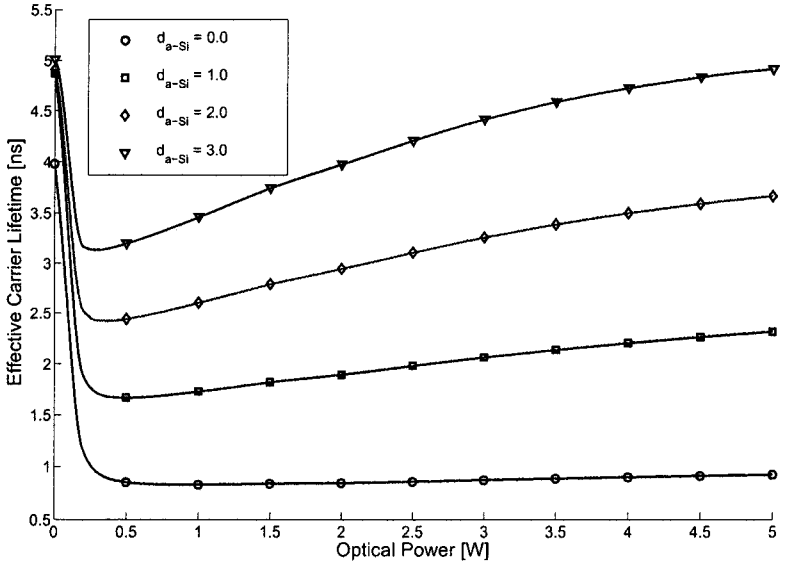

Figure 3.11: Effective lifetime of WG-1 as a function of optical power for $h_{a\text{-Si}} = h$.

3.3.4 Raman Gain Calculations for Waveguides with Remote Defect Volumes

By combining the results of the optical loss and carrier lifetime simulations, the net Raman gain of a silicon waveguide can be calculated. The analysis is similar to that previously used for the uniform defect distribution in section 3.2, however in equation 3.6 the carriers generated due to defect absorption was omitted (i.e. there

is no overlap of the optical mode and the defects). Also, the optical absorption of the a-Si at the Stokes signal was assumed to be equal to that of the pump.

The net Raman gain for WG-1 and several remote defect configurations is shown in figure 3.12. As can be seen, net gain cannot be achieved in the case of the intrinsic waveguide. When remote defect volumes are applied, net gain is obtained for several defect volume positions. For the case of $h_{a\text{-Si}} = h$, maximum gain is achieved when $d_{a\text{-Si}} \approx 2.0$ μm. Although not shown, marginally better performance can be achieved for $h_{a\text{-Si}} \neq h$, due to the reduced optical loss. For the larger structures under consideration, defects improve the overall performance but net gain is never achieved.

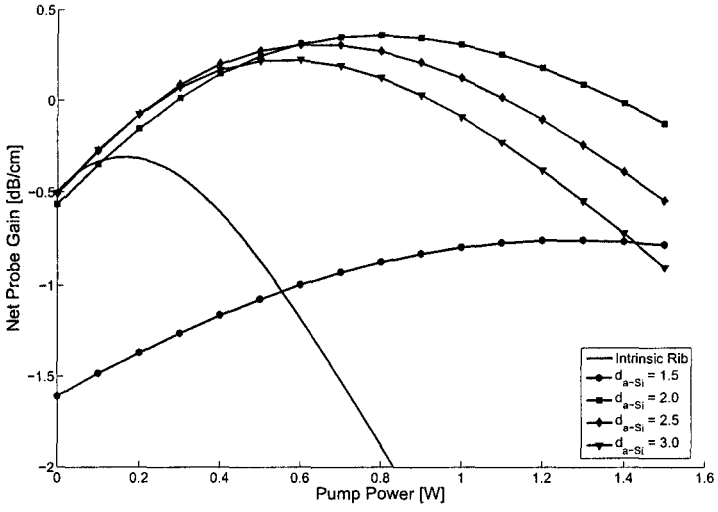

Figure 3.12: Maximum net gain for WG-1 with several defect configurations.

The important conclusion to draw from this section is that unlike the case of a uniform defect distribution, remote defect volumes can induce net Raman gain in a silicon waveguide. The lifetime reduction for well separated a-Si regions is significant enough to reduce two-photon absorption (TPA) induced free carrier absorption (FCA), while maintaining low propagation losses. Thin a-Si regions provide a higher

lifetime reduction per unit of optical loss. This is in agreement with the results of section 3.2, in which it was shown that it is possible to increase the net gain by engineering the surface recombination velocity. In this best case scenario, carrier lifetime is reduced with little optical loss due to defect absorption. Finally, since trap saturation is not limiting free carrier reduction, a more amenable material, such as *poly*-Si, which has a lower optical absorption and refractive index relative to *a*-Si but longer free carrier lifetime, should be used to improve performance.

Chapter 4

Experimental Results

The properties of SPER suppressed *poly*-Si were examined for the application of this fabrication technique to silicon Raman lasers and other silicon photonic devices.

4.1 Sample Fabrication

For the analytical experiments described here, sample preparation and fabrication followed similar, if not identical procedures. These are now summarized. SOI samples diced from a 4 inch wafer were cleaned by rinsing in acetone and methanol. This was followed by an ultra-violet (UV) oxidation process and finally a dip in buffered hydrofluoric acid (HF) to remove the top SiO_2 layer. Various SOI wafers were used in this work and their relevant physical properties are summarized in Table 4.1.

Table 4.1: SOI samples used in this study.

Name	Top Si Thickness [nm]	BOX Thickness [nm]	SOI Fabrication Technology
SOI-1	110	200	SIMOX
SOI-2	1500	3000	SmartCut®
SOI-3	2500	375	SIMOX

The ion beam induced amorphization of the silicon overlayer for all samples was

performed at the University of Western Ontario using a Tandetron accelerator. All implants used a silicon ion species (i.e. they were self-implanted) and were done at liquid nitrogen temperature (i.e. -196 °C) to maximize damage retention. Samples were oriented with 7° tilt and 20° rotation to minimize channeling effects. The implant recipes used are summarized in Table 4.2. The order of the steps for multiple energy recipes proceeded from lowest energy to highest. The predicted a-Si depth is based on the displacement criterion (i.e amorphization occurs for lattice displacements $> 1 \times 10^{21}$ cm^{-3}). The simulated displacement and Si^+ profiles are shown in figure 4.1 for several recipes.

Table 4.2: Implantation protocols used in this study.

Name	Energy [keV]	Dose [cm^{-2}]	Simulated a-Si Depth [nm]
Rec-1	100	5×10^{15}	240
Rec-2			771
	80	1×10^{15}	
	500	2×10^{15}	
Rec-3			1538
	500	1.6×10^{15}	
	900	3.0×10^{14}	
	1400	1.7×10^{15}	
Rec-4			1549
	80	5×10^{14}	
	500	2×10^{15}	
	900	9×10^{14}	
	1400	2×10^{15}	
Rec-5			2142
	Rec-4 +		
	1900	1×10^{15}	
	2500	2×10^{15}	
Rec-6			2696
	Rec-5 +		
	3100	1×10^{15}	
	3800	2×10^{15}	

Amorphization of the silicon overlayer was a non-trivial process step. On several

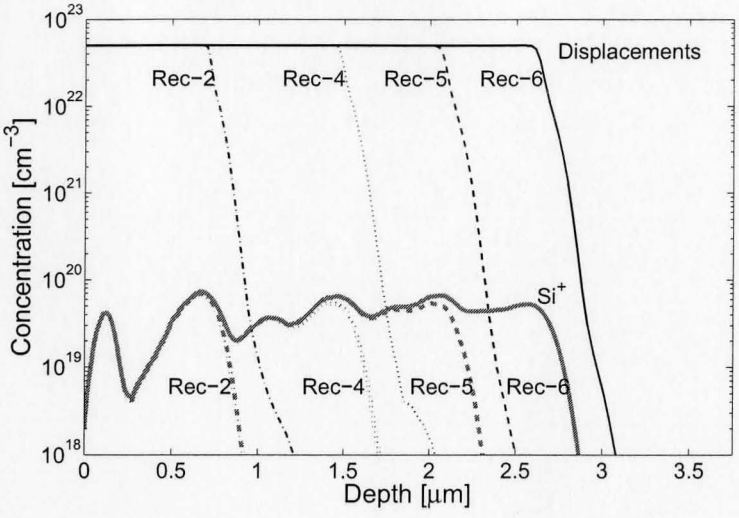

Figure 4.1: Displacement and Si^+ implant profile for selected recipes used in this study. Maximum number of lattice displacements is equal to the atomic density of silicon, 5×10^{22} cm^{-3}.

occasions attempts to completely amorphize the silicon overlayer failed and *poly*-Si did not form following post-implantation annealing. The exact cause of this is still not completely understood. In the early stages of this work, the 1500 nm Si overlayer sample was amorphized using Rec-3 and resulted in *poly*-Si after annealing. Later work, using Rec-3 and even Rec-4 failed to completely amorphize the surface layer. Initially, it was thought that thermal effects (due to beam-induced sample heating) were to blame. Samples were thus mounted using silver paste, as opposed to single surface clips, to guarantee good thermal contact with the liquid nitrogen cooled block on which the samples were mounted. This did not improve the reliability of the amorphization process and future attempts used multiple clips to assure good thermal contact. Ion channeling during implantation was also thought to contribute to this processing problem, however, the order of the multiple-energy implantation (a consideration which might impact the amount of channeling) had no impact on process reliability. To confirm this experimental observation, simulations were done

to compare the original and channel enhanced implantation profiles. It was shown that the order of the implantation resulted in marginally different implant profiles and predicted amorphous depths, however, the displacement damage was still predicted to be always saturated throughout the entire silicon overlayer. Excessive variation of the starting material, Si overlayer thickness was dismissed through SEM measurement of the SOI which showed that it was within quoted specification and was always less than 1.52 μm. The exact cause of the unreliability of the amorphization process remains unknown.

Several samples were masked during implantation in order to retain a portion of crystallinity within the silicon overlayer. For these masked samples, a thick SiO_2 layer was deposited using plasma-enhanced CVD (PECVD). A minimum thickness of 500 nm was used for all samples. For masked implants, the amorphization depth was placed as close as possible to the buried oxide in order to minimize the impact of EOR defects on subsequently regrown material. This process requires an accurate measurement of the amorphization depth, mask thickness/density and a highly uniform mask and silicon overlayer. After oxide deposition, the samples were annealed for 10 minutes at 900 °C in N_2 using a rapid thermal annealer (RTA). This was done to remove gases incorporated into the SiO_2 film during growth and increase its density for improved implant masking. The annealed film had an etch rate in HF acid approximately equal to that of a thermally grown oxide, which is half the etch rate of an as-deposited film. After implantation, the mask was removed before annealing to avoid stress induced defect formation.

Photolithography was required as an intermediary processing step for samples requiring a selective mask prior to implant, or in the case where waveguides were to be fabricated. A previously developed, standard, photolithography process for silicon samples was used. Details can be found in Ref. [122]. SOI samples were cleaned

using acetone/methanol/ozone/HF. For masks used for the definition of waveguide structures using a subsequent etching process, a thin ~100 nm PECVD oxide was deposited. For implantation masks the thickness was 500 nm. Primer and photoresist (Shipely 1808) were spun onto the sample and patterned. After developing the photoresist, the mask oxide was selectively removed with HF acid. Silicon etching (in the case of waveguide formation) was done at the University of Western Ontario using an Alcatel 601E silicon etcher utilizing a Bosch style process.

All thermal annealing was performed using a Jipelec Jetfirst 100 rapid thermal annealer (RTA) in a high purity nitrogen atmosphere. Annealing recipes were based on a slow ramp-up and hold at a low temperature (e.g. 275 °C), followed by a fast 15 second ramp-up to the desired anneal temperature. Annealing temperature was monitored using two thermocouples for low temperature anneals and a pyrometer for temperatures >1000 °C. A complete description of calibration and monitoring issues can be found in Ref. [123]. All temperatures mentioned in this work refer to the set temperature of the RTA.

In retrospect, using the RTA for this work may have resulted in variation of the sample temperature from the temperature set-point. The RTA units use intense halogen lamps to heat samples via optical absorption. Consequently, annealing SOI and *a*-SOI samples in this manner can be problematic since a) the buried oxide layer acts as a thermal insulator and b) the absorption constant of *a*-Si changes as it transforms to either *c*-Si or *poly*-Si. The RTA Jetfirst design measures the underside temperature of a silicon wafer on which the samples are placed and not the surface temperature of the sample. Complete and thorough characterization of this unit is required for an accurate representation of the annealing process.

4.2 Defect Etching

4.2.1 Background

Defects abound in silicon and are caused by standard processing techniques such as crystal growth, oxidation and etching [124]. However, optimization of processing parameters in the five decades of silicon's usage as a microelectronics material has dramatically reduced defect densities to almost negligible concentrations. This demanding, high-yield, manufacturing environment requires that these densities are maintained if not further reduced. For 2008, the ITRS requires the defect density of the initial Si wafer to be <0.022 cm^{-2} [7]. Measuring a small number of sub-micron defects on a large 300 mm wafer is a difficult task. Defect etching has been used to alleviate many of the associated problems and make defect identification fast and straightforward.

As the name implies, defect etching uses wet chemical etchants to preferentially etch defects close to the surface. This allows for quick defect characterization that can be monitored with a simple optical microscope. The etchant attacks the strained areas around a defect revealing defect location and size. The technique is somewhat qualitative since a fundamental understanding of the chemistry behind different etching solutions and the resulting etched profiles has not been established. The resulting optical images require considerable subjective interpretation since many defects yield similar etched patterns. Also, different etching solutions can cause different etched patterns for identical defects. In the past, a large number of defect etchants have been produced. These include Dash [125], Wright [126], Sopori [127], Yang [128], Secco [129] and many more. Each solution has properties, such as etch rate and preferential etch direction, that makes its applicability dependent on the sample and defect under observation.

4.2.2 Experimental Results

The *poly*-Si characteristics and lateral regrowth properties were investigated using the defect etching technique. Samples of *poly*-Si were fabricated using SOI with a silicon overlayer of 1.5 μm, implanted with REC-4 and subsequently annealed. They were cleaned using an acetone/methanol/ozone/HF procedure. To analyze the lateral regrowth, samples were created using a periodic mask, which resembles an optical grating. Standard photolithography procedures were used. A thick, ~615 nm oxide served as the implant mask. The patterned mask had a 10 μm period with 50:50 duty cycle. The *grating* lines were oriented parallel to the $\langle 011 \rangle$ planes (i.e. the natural cleave planes of (100) silicon). Masked samples were annealed for 10 minutes at 650, 750 and 900 °C. Unmasked samples were also prepared and were annealed for 30 minutes at 650 and 900 °C.

A Dash etchant solution, consisting of HF (49%), nitric acid (HNO_3) and glacial acetic acid (CH_3COOH) in a ratio of 1:3:10 was used to delineate the defects. This solution was chosen since it has a slow etch rate, is isotropic, leaves no residue and is relatively safe to handle. The etch times for various samples ranged between 10's of seconds to several minutes. The effect of the etchant is easy to observe. As-implanted samples turn black after several seconds in the solution since the etched surface is very rough. For thermally recrystallized samples, etching was done in stages after which the sample was observed using an optical microscope. Etching was continued if no defects were revealed.

The unmasked, *poly*-Si samples were annealed for 30 minutes at 650 and 900 °C and etched for 1 and 3 minutes respectively. Figure 4.2 shows the distinctive difference between etched *poly*-Si, damaged *c*-Si and regrown *c*-Si regions. Masking in this sample was accomplished via the clips required to hold the sample during ion

implantation. For the most part the clips do not make direct contact with the sample allowing damage to accumulate underneath the mask edge. However although this damage is considerable, it does not result in amorphous material and hence thermal annealing does not result in the regrowth of crystalline material and the region remains highly defective. This allows differentiation between damaged and regrown silicon. Assuming the damaged silicon interface remained fixed, the average lateral regrowth was 16.57±0.2 μm after annealing for 30 minutes at 650 °C. Relatively speaking, this is quite large in comparison to the typically reported values of 5-10 μm [130]. The minimum regrowth rate is 552±6 nm/min, although it is likely higher since the exact time the lateral regrowth was stopped by the formation of the *poly*-Si/*c*-Si interface is unknown. Regardless, at 650 °C the predicted regrowth rate according to Csepregi *et al.* for [111] and [011] growth is 16 and 112 nm/min [91]. It is noted that this discrepancy could result from an RTA temperature miscalibration of ~50 °C (assuming [011] growth), however, such a miscalibration would have also yielded a much higher grain nucleation rate; effectively reducing total lateral regrowth. Higher growth rates have been reported for tensile stressed silicon, which is the case in most SOI and the postulated stress state in these films (see section 4.4 below) [131]. It is also possible that a reduced nucleation rate due to a native oxide caused the excessive regrowth. Further study is required to determine this distinction. Noticeably, in some surface areas the damaged *c*-Si/regrown *c*-Si and regrown *c*-Si/*poly*-Si interfaces are not parallel indicating some preferential growth. This observed facet was parallel to the cleaved facet and is deemed to be the (111) plane (i.e. the predicted facet for [011] directed regrowth).

Figure 4.3 shows the etched *poly*-Si annealed at 650 and 900 °C. Estimating the grain size of relatively small grained *poly*-Si with defect etching is very difficult since both grain and grain boundaries are etched, merely at different rates. Also, Dash

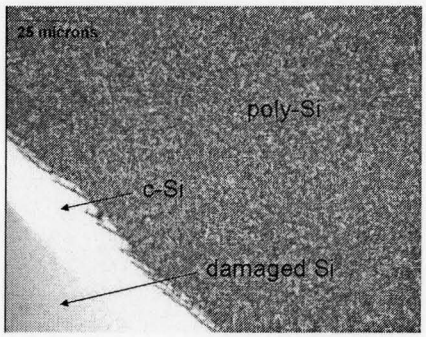

Figure 4.2: Etched *poly*-Si sample annealed for 30 minutes at 650 °C. The etchant distinctly reveals *poly*-Si, *c*-Si and damaged *c*-Si regions.

etchant is isotropic yielding rounded surfaces. Therefore unless the grain size is very large ($> 1\mu$m), an accurate measurement is not possible. The surface of the 650 °C sample is more textured than the 900 °C, possibly indicating a larger grain size. For the 900 °C annealed sample, defect etching after 3 minutes was only apparent at an already defected area; a scribe mark. Thus the 900 °C sample is of higher quality than 650 °C sample. Focused ion beam (FIB) milling and SEM analysis were attempted as a means to estimate grain size, however they yielded no definitive results. Direct observation of the *poly*-Si grains thus requires TEM or possibly SEM of a *poly*-Si sample with an annealed gold film, with the expectation that gold would preferentially diffuse along the grain boundaries.

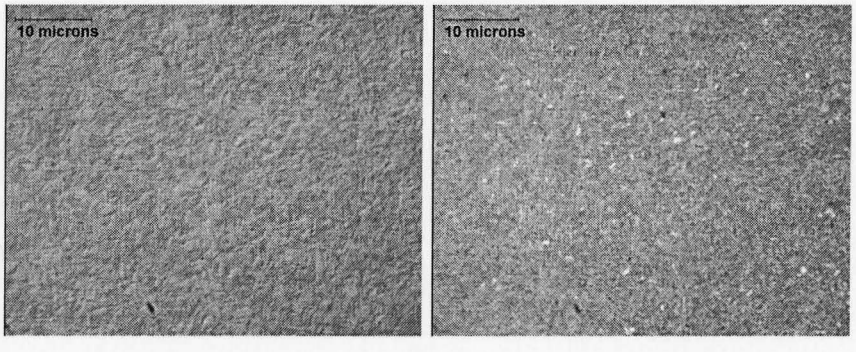

Figure 4.3: Etched *poly*-Si samples annealed for 30 minutes at 650 °C (left) and 900 °C (right).

For masked samples with grating patterns, the etched results are shown in figure 4.4. X-ray diffraction measurements were taken before etching and *poly*-Si was detected in the 750 and 900 °C samples. The 650, 750 and 900 °C samples were etched for 150, 30 and 45 seconds. Lateral regrowth is evident in all three samples. For the low temperature case, lateral regrowth exceeded 2.5 μm and so the entire surface regrew into *c*-Si. For 750 and 900 °C anneals, both RNG and L-SPER were present and can be seen by the appearance of *poly*-Si regions between masked regions. The regrown *c*-Si had an average width of 8.06±0.2 and 6.92±0.2 μm for the 750 and 900 °C samples. This gives a lateral regrowth of 1.53±0.2 and 0.96±0.2 μm.

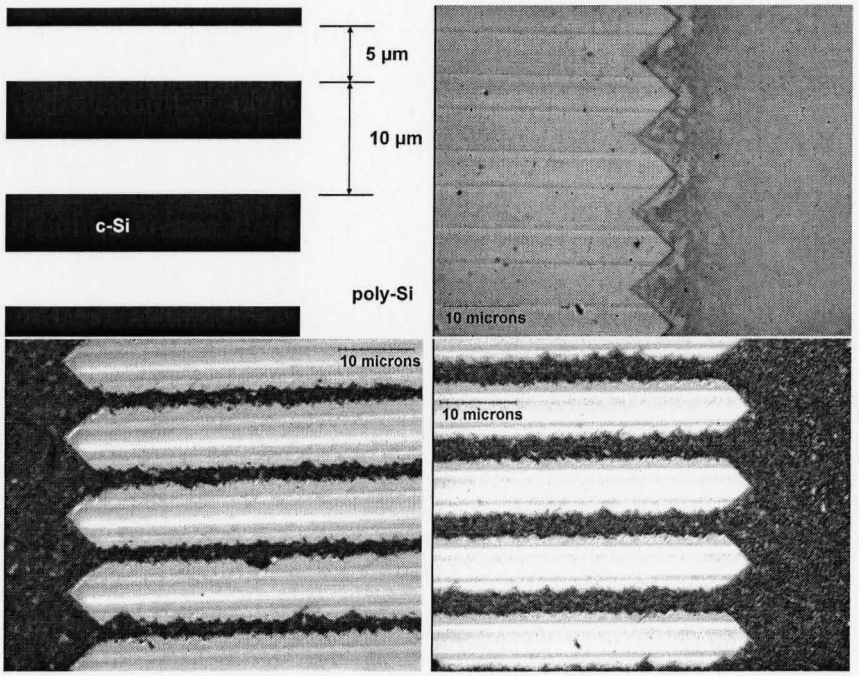

Figure 4.4: Etched *poly*-Si gratings annealed for 10 minutes. Top Left) Patterned mask. Top Right) 650 °C. Bottom Left) 750 °C. Bottom Right) 900 °C.

Evident in all three samples is the (110) faceting that occurred at the edge of the grating. This forms an almost perfect saw-tooth pattern in the case of the fully regrown sample. In the 750 and 900 °C samples, the *c*-Si/*poly*-Si interface is extremely

rough indicating that at the higher temperatures RNG proceeded fast enough to prevent faceting. For the 650 °C sample, sparsely positioned faceting is observed between grating lines (see figure 4.5). This is probably due to improper masking, since this was not apparent over the bulk of the sample. Figure 4.5 shows distinct lines between masked regions, indicative of the large number of defects present at the point of collision between regrown *c*-Si phase fronts. These are essentially grain boundaries.

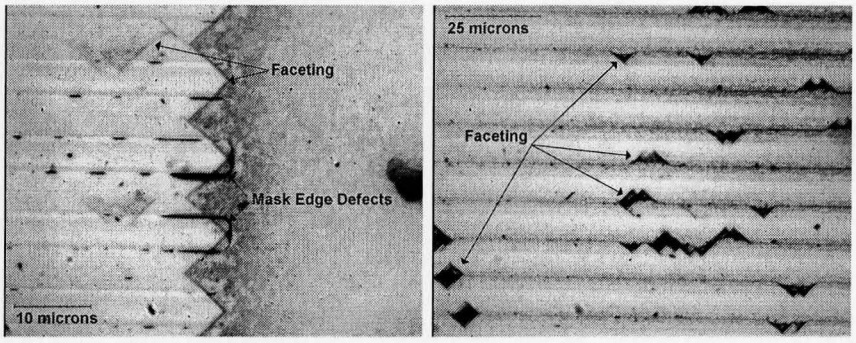

Figure 4.5: Etched *poly*-Si gratings annealed at 650 °C. Left) Mask edge defects. Right) Faceting and grain boundary-like defects.

Interestingly, the mask edge lines do show that the lateral regrowth is incomplete through the mask edge. From the lateral regrowth in the bulk grating region (described in figure 4.4), it is apparent that the regrowth should have exceeded 2.5 μm for a 10 minute anneal at 650 °C. The only difference between the bulk grating and the edge is that the straggle of the original implantation step would have created a curved *c*-Si seed. This encourages early facet formation [130]. Lateral growth likely stopped due to defect formation resulting from the implant mask or multiple plane regrowth (as seen in figure 2.8).

The different etch times are related to varying defect concentrations. The 650 °C grating sample took the longest since it was essentially *c*-Si. Although most of the 650 °C sample was *c*-Si, a small region was *poly*-Si. This is perhaps an indication

of the random nature of the regrowth/nucleation processes, or perhaps simply an enhancement in nucleation rate due to an isolated defect. For the 750 °C sample RNG stopped lateral SPER preventing complete recrystallization, but the short etch time indicates that the *poly*-Si has a lot of defects at the grain boundaries or perhaps even *a*-Si. The slightly longer etch time for the 900 °C sample indicates that it is of better quality than the 750 °C sample, but compared with the 650 °C sample, the grain boundaries are still a large source of defects.

4.3 Ellipsometry

4.3.1 Background

Ellipsometry is an optical technique used to measure the properties of thin films based on the reflection and/or transmission of polarized light. For a sample with a single interface, the reflection and transmission coefficients for the incoming light are polarization dependent and given by the Fresnel equations [132]

$$r_{\parallel} = \frac{n_2^* \cos\theta_1 - n_1^* \cos\theta_2}{n_2^* \cos\theta_1 + n_1^* \cos\theta_2} \tag{4.1}$$

$$r_{\perp} = \frac{n_1^* \cos\theta_1 - n_2^* \cos\theta_2}{n_1^* \cos\theta_1 + n_2^* \cos\theta_2} \tag{4.2}$$

$$t_{\parallel} = \frac{2n_1^* \cos\theta_1}{n_2^* \cos\theta_1 + n_1^* \cos\theta_2} \tag{4.3}$$

$$t_{\perp} = \frac{2n_1^* \cos\theta_1}{n_1^* \cos\theta_1 + n_2^* \cos\theta_2} \tag{4.4}$$

where $n_{1,2}^* = n_{1,2} + \mathbf{i}k_{1,2}$ is the complex refractive index and $\theta_{1,2}$ are the incident and refracted angles. Light with electric fields parallel to the incident plane are called p or TM polarized, whereas those perpendicular are called s or TE polarized. The intensity of the reflected light, R, is given by $R_{\perp,\parallel} = \mid r_{\perp,\parallel} \mid^2$. The ellipsometry technique used

in this work is a reflection based configuration that monitors the reflectivity of each polarization.

By using Snell's law and the Fresnel equations, it can be shown that p polarized light exhibits a minimum in reflectivity at the Brewster angle, given by $\theta_B = \tan^{-1}(\frac{n_2}{n_1})$ [132]. This can be zero or non-zero depending on whether the material is absorbing or non-absorbing. Because the differences in reflectivity are maximized near the Brewster angle, reflectivity-based ellipsometry measurements are commonly taken around this point. For an Air/Si interface, the Brewster angle is $\sim 74°$.

An ellipsometer measures changes in the polarization state of reflected light. By using complex reflection coefficients, the ratio between p and s reflection coefficients is written as [60]

$$\rho = \frac{r_p}{r_s} = \tan \Psi e^{i\Delta} \tag{4.5}$$

where Ψ represents the magnitude and Δ represents the phase difference between p and s polarizations. Using these measured values, combined with an initial model for the material under question (i.e. approximate thickness and refractive index of the materials present), the pseudodielectric function, $\epsilon = \epsilon_1 + i\epsilon_2$, can be calculated. This in turn gives the complex refractive index of the material such that [60]

$$\epsilon_1 = n^2 - k^2 \qquad \epsilon_2 = 2nk \tag{4.6}$$

4.3.2 Experimental Results

Knowledge of the refractive index of *a*-Si and SPER suppressed *poly*-Si is essential for silicon photonic applications. Besides acquisition of the absolute value, monitoring changes in the refractive index for various annealing conditions helps determine crystallization kinetics of the *a*-Si films. Samples were measured with a variable angle,

visible wavelength, spectroscopic ellipsometer at the École Polytechnique in Montréal.

Thin SOI samples (SOI-1) with a silicon overlayer thickness of 110 nm were amorphized using REC-1. For ellipsometry measurements, the thin Si layer minimizes the number of interference oscillations in the measured data and allows for easier modeling of the data. Thicker SOI samples with a 1.5 μm overlayer were also measured, however, the data were of insufficient quality to analyze due to high levels of depolarization. The thin samples were annealed for 10 minutes at 275, 475, 700 and 900 °C. Ellipsometer measurements were done at angles of 65, 70 and 75°. The resulting data were then analyzed using the parametric oscillator model. This method models the dielectric function using a sum of Lorentz oscillators that represent the fundamental electronic transitions of the crystalline material. By using the values for *c*-Si as a starting point and optimizing the peak energy, amplitude, width and symmetry of each oscillator, the dielectric function of *a*-Si and *poly*-Si can be acquired. These materials exhibit properties similar to *c*-Si, however the sharp transitions are usually broadened since they do not possess long range order. The oscillator model has previously been used to characterize *a*-Si and has been shown to produce good results [66].

The modeled refractive index is shown in figure 4.6. The 700 and 900 °C samples exhibit a refractive index profile that strongly resembles that of *c*-Si. This indicates a high crystalline fraction. Typical of amorphous materials, the sharp peak at ~400 nm broadens for the as-implanted and low temperature annealed samples. The distinct difference between low and high temperature anneals is a strong indication of the change from *a*-Si to *poly*-Si. This was confirmed with x-ray diffraction. The sharpening peak at 400 nm for the low temperature anneal represents the change from the as-implanted to the relaxed state of the *a*-Si structure.

The refractive index at 1550 nm is shown in figure 4.7. For as-implanted and

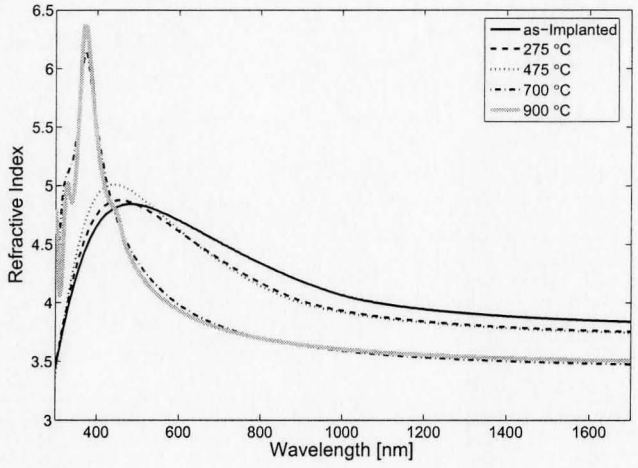

Figure 4.6: Modeled refractive index of a-SOI for 10 minute anneals at 275, 475, 700 and 900 °C.

relaxed a-Si, the modeled index was 3.86 and 3.76, respectively. This compares well with the previous reported values of 3.9 and 3.76 [63]. Unlike previous reported work, the relaxed phase formed after a relatively short, relatively low temperature anneal. Other studies have typically used longer anneal times (i.e. hours) and higher temperatures. The transition point between the as-implanted and relaxed phases has never been thoroughly studied or described and hence the refractive index throughout this transition region remains undetermined. For higher annealing temperatures, the refractive index approaches that of c-Si ($n = 3.48$), with an unexpected, relatively small rise in index between 700 and 900 °C.

4.4 X-Ray Diffraction

4.4.1 Background

X-ray diffraction (XRD) is a versatile experimental tool that can be configured to measure a variety of sample parameters. It is non-destructive, requires minimal

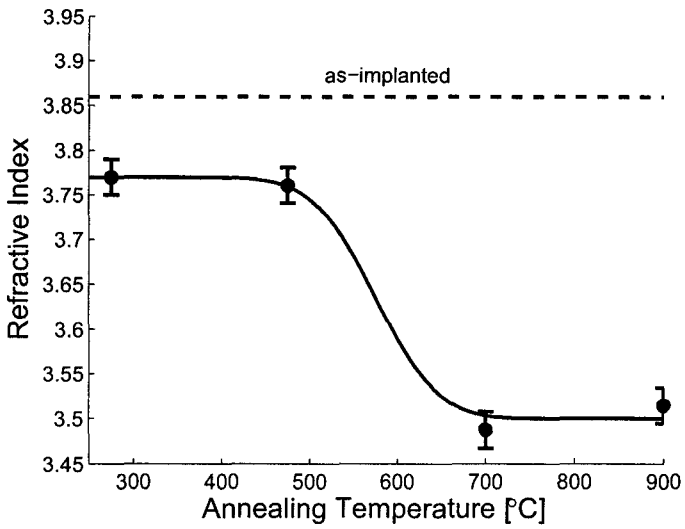

Figure 4.7: Refractive index of a-SOI at 1550 nm for 10 minute anneals at 275, 475, 700 and 900 °C. Line drawn to guide eye.

sample preparation and probes an averaged sample volume. It has been used in silicon processing to measure SOI thickness [133], implantation-induced strain [133], and physical properties of both silicon nanocrystals [134] and polycrystalline silicon. [135].

The lattice planes of a crystal serve as a diffraction grating for incident x-rays. Constructive and destructive interference of the reflected x-rays create a diffraction pattern that follows Bragg's law [136]

$$m\lambda = 2d\sin\theta \tag{4.7}$$

where λ is the wavelength of the incident x-ray, d is the spacing between the lattice planes, θ is the incident angle and m is an integer. Equation 4.7 is only satisfied for specific angles, called Bragg angles, which vary according to the lattice plane under

investigation. The planar spacing, d, for a cubic crystal is given by [136]

$$d = \frac{a_0}{\sqrt{h^2 + k^2 + l^2}} \tag{4.8}$$

where a_0 is the lattice constant (5.43095 Å for c-Si), and h,k and l are the Miller indices of the plane in question.

Fixed, glancing angle x-ray diffraction is an alternative to the standard $\theta - 2\theta$ scan. The setup is depicted in figure 4.8 and requires fixing the incident angle of the x-ray and scanning the detector over the 2θ axis. This technique then is ideal for thin films since the penetration depth of the x-ray is related to its incident angle. This creates larger signal contributions from the layer in question and less noise from the substrate. Also, unlike θ–2θ, the probed sample volume remains constant. Analogous to optical photons, a critical angle, ω_c, exists at which total reflection occurs. This is defined as [137]

$$\omega_c = 1.6 \times 10^{-3} \rho \lambda \tag{4.9}$$

where ω_c is in radians, ρ is the sample density [g/cm^3] and λ is the wavelength of the x-ray [Å]. The penetration depth, t, is given by [137]

$$t = \begin{cases} \lambda/(2\pi\sqrt{\omega_c^2 - \omega^2}) & \omega < \omega_c \\ 2\omega/\mu & \omega > \omega_c \end{cases} \tag{4.10}$$

where t is in microns and μ is the linear absorption coefficient [μm^{-1}].

XRD is an excellent technique for powder and polycrystalline samples. In this case, a small fraction of the randomly oriented grains will meet the Bragg condition for each lattice plane. This allows simultaneous analysis of all peaks with a simple 2θ scan. The method suffers from the low intensity of the measured signal since only

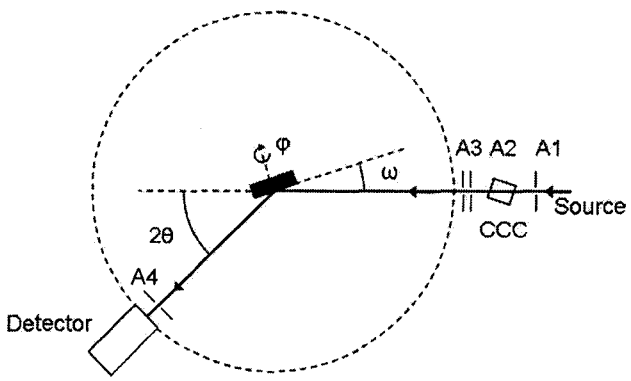

Figure 4.8: Schematic for fixed, glancing angle diffraction. Incident x-rays pass through channel cut crystal (CCC), circular apertures A1 and A2, and slit apertures A3 and A4.

a small portion of the sample will contribute to each diffraction peak.

Numerous methods are available to analyze a diffraction pattern. This can involve using the entire measured pattern, multiple diffraction peaks or simply a single peak [138]. Individual peaks can be fit with various functions such as Gaussian, Lorentzian, Voigt or pseudo-Voigt. Fit parameters such as the peak position, height, width and integral breadth can then be correlated to physical properties. Accurate characterization of instrumental effects is required to extract sample parameters from the measured data.

In general, four peak characteristics are used in describing the material under question: intensity, area, position and width. The relative integrated intensity of each peak describes the texture of the sample. In an ideal, random powder sample the integrated intensity is related to a variety of factors (e.g. crystal structure, lattice plane, temperature, etc.) and can be calculated from first principles. By looking at the relative areas of different peaks and comparing to a standard case, the texture of the material can be determined.

Sample strain is correlated with shifts in the diffraction peak position. The strain,

ε, is given by [136]

$$\varepsilon = \frac{d - d_0}{d_0} = -\cot\theta(\theta - \theta_0) \tag{4.11}$$

where θ_0 and d_0 are the Bragg angle and planar spacing of an unstrained sample, and θ and d are the Bragg angle and planar spacing of the sample under investigation. This equation describes the average strain of the sample and is referred to as macrostrain. On the other hand peak broadening is related to microstrain and crystallite size. Microstrain refers to the strain variation between grains or the variation within a single grain. The maximum strain resulting from microstrain is given by [138]

$$\varepsilon = \frac{\beta_{int}}{4\tan\theta} \tag{4.12}$$

where β_{int} is the integral breadth, defined as $\beta_{int} \equiv \frac{A}{I}$, A is the peak area and I is the peak intensity. Broadening due to crystallite size is calculated using the Scherrer formula [139]

$$d_g = \frac{K\lambda}{\beta_{int}\cos\theta} \tag{4.13}$$

where d_g is the apparent size and K is a shape constant, which is approximately 0.9 for the $\langle 111 \rangle$ peak of silicon [139]. For spherical grains, the average diameter is $\langle d_g \rangle = 4d_g/3$ [138]. Based on equations 4.12 and 4.13, wider peaks are associated with small crystallites or large strains, while narrower peaks imply large crystallites or small strains. Each broadening effect can be present and so separation is achieved by observing multiple peaks since each effect has a different θ dependence. This is called the Williamson-Hall method [138]. In this approach, the integral breadth is plotted as a function of the scattering vector, $Q = \frac{4\pi\sin\theta}{\lambda}$, and a linear fit is performed. The size and strain effects can then be distinguished from the measured integral breadth

using [138]

$$\beta_{int} = \frac{1}{D} + 2\varepsilon_g Q \tag{4.14}$$

where D is the volume averaged apparent grain diameter and ε_g is the average microstrain of the crystallites. Therefore the slope and intercept of the linear fit represent the strain and size components respectively. When only a single peak is available, the Gaussian component is associated with strain effects, while the Lorentzian component is associated with size effects.

4.4.2 Experimental Results

Fixed, glancing angle x-ray diffraction (XRD) measurements were performed to characterize the *a*-SOI films. 2θ scans were performed in a Bede D1 diffractometer to observe the emergence and growth of *poly*-Si grains upon annealing of amorphous silicon.

Thick *a*-SOI samples were prepared using SOI-2 (silicon overlayer of 1500 nm) and implant recipe REC-4. Samples were left unmasked, cleaned, implanted and annealed. Annealing was done for 10 minutes at 300, 450, 550, 600 650, 750, 900, 1050 and 1200 °C. One sample was isochronally annealed for 10 minutes at various temperatures up to 1200 °C and XRD measurements were taken after each annealing cycle.

The schematic for the experimental setup is shown in figure 4.8. The Bede D1 uses a copper source and the Kα lines as the x-ray source. Both Kα_1 ($\lambda = 0.154056$ nm) and Kα_2 ($\lambda = 0.154439$ nm) lines are present. The Kα_2 line is removed by passing the x-ray through a channel cut crystal (CCC) and apertures (A1 and A2). The parameters for a typical XRD scan are shown in Table 4.3. The low signal intensity from the *poly*-Si samples required a relatively long sampling time to increase the

signal to noise ratio.

Table 4.3: XRD parameters.

Name	Value	Name	Value
Acc. Voltage	-45 keV	Current	40 mA
A1	10 mm	A2	10 mm
A3	0.5 mm	A4	0.5 mm
ω	2.5°	φ	20°
Scan Step	0.05°	Time/Step	120 seconds

The primary purpose of this technique was to determine the presence of *poly*-Si and verify the amorphization and regrowth process worked correctly. A typical XRD measurement is shown in figure 4.9. The as-implanted and unimplanted SOI are shown for comparison. In *poly*-Si, the diffraction peaks appear for 2θ values of ~28.4, 47.3 and 56.1° corresponding to $\langle 111 \rangle$, $\langle 220 \rangle$ and $\langle 311 \rangle$ planes. The peak at 42.8° corresponds to the sample holder.

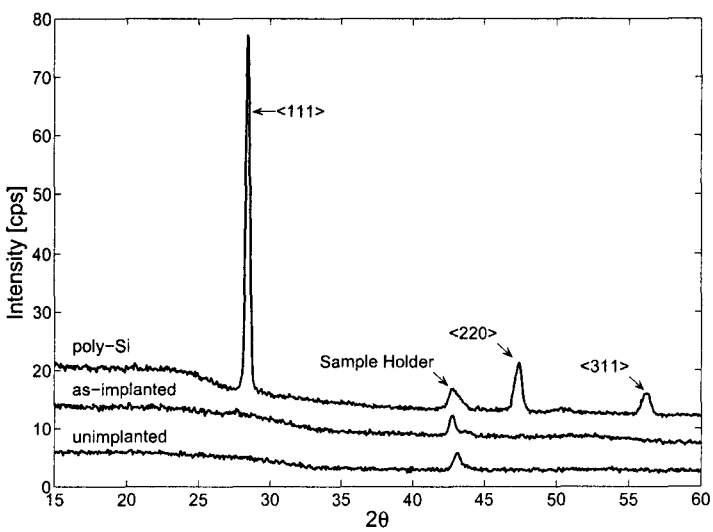

Figure 4.9: Measured XRD intensity for unimplanted and as-implanted SOI, and 900 °C isochronal sample. Offset for clarity.

Selected diffraction profiles of the isochronally annealed sample are shown in figure

4.10. Initial observation of crystallite formation was after the 575 °C anneal. Before this, the sample had undergone 10 minute anneals at 400, 475, 525 and 550 °C. The peak intensity increases quickly after the initial grain formation and then remains relatively constant. Figure 4.10 also shows the measured strain based on the ⟨111⟩ peak, equation 4.11 and an annealed powder silicon reference. If an isotropic, biaxial stress state is assumed (i.e. stress only parallel to surface), this shows the film is in tension. Tensile stressed *poly*-Si has previously been reported for recrystallized, ion-implanted, deposited *a*-Si films [140].

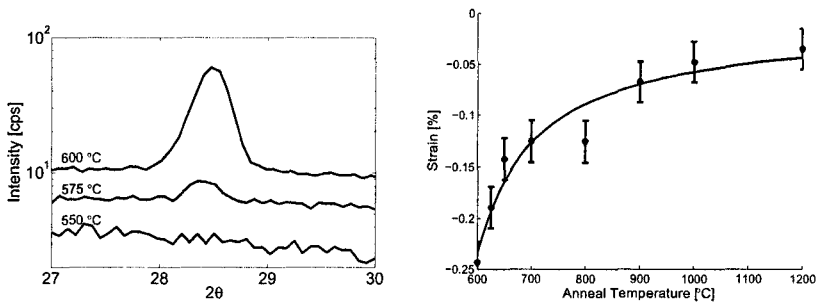

Figure 4.10: Left) Measured XRD intensity for isochronal sample after 550, 575 and 600 °C annealling steps. Right) Macrostrain of the isochronally annealed *a*-SOI. Line drawn to guide eye.

The XRD patterns for the single-step annealed samples are shown in figure 4.11. In this case, *poly*-Si formation was only observed after a 650 °C anneal. There is very little evolution in the diffraction pattern for different annealing temperatures. The maximum intensity of the diffraction peaks remains relatively constant for different temperatures; an indication that the crystal fraction in all samples is close to one. The texture of the *poly*-Si was evaluated by measuring the integrated intensities for the ⟨111⟩, ⟨220⟩ and ⟨311⟩ lines and comparing to published standards. For the samples shown in figure 4.11, the ratio for $\frac{A_{220}}{A_{111}}$ and $\frac{A_{311}}{A_{111}}$ ranged from 0.62-0.66 and 0.34-0.40. This compares well with the 0.6 and 0.35 published standards and indicates that

there is no texture in the *poly*-Si samples [141]. For the sample annealed at 1200 °C, a black film began to grow. This could not be removed with acetone/methanol/HF. It has been shown that high temperature annealing of solar-grade *poly*-silicon yielded SiC precipitates and carbon/oxygen complexes [142]. Whether this is the case here is yet to be determined.

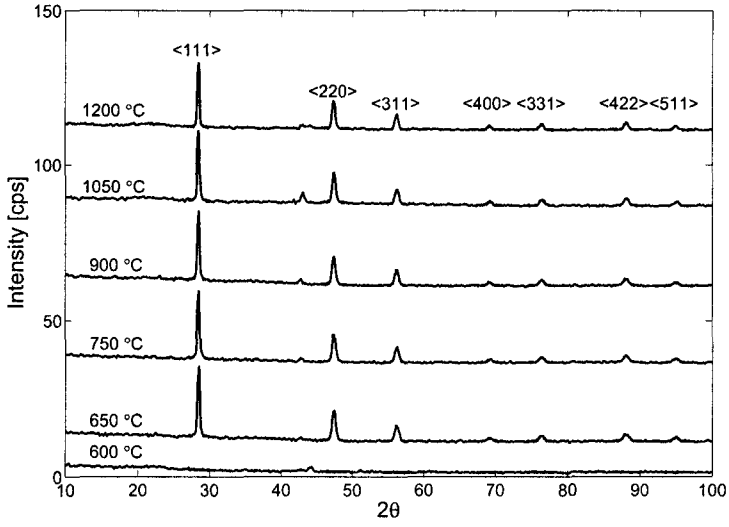

Figure 4.11: Measured XRD intensity of samples annealed for 10 minutes at various temperatures. Curves are offset for clarity.

Analysis of the grain size was done using the Hall-Williamson approach. Only the first three peaks were used in the analysis since the low intensity of the other peaks caused significant error in the fitting parameters. Peaks were fit using a Voigt function and corrected for instrumental broadening. The estimated apparent size and strain are shown in figure 4.12. The apparent size ranged from 217 to 75 nm, corresponding to an actual size of 289 to 100 nm (assuming spherical grains). This trend coincides with the idea that higher temperatures induce higher grain nucleation rates and in turn smaller crystallite sizes. Secondary grain growth, expected at high temperatures, is not shown to occur for the short, 10 minute anneal. Expectedly,

microstrain is reduced at higher temperatures.

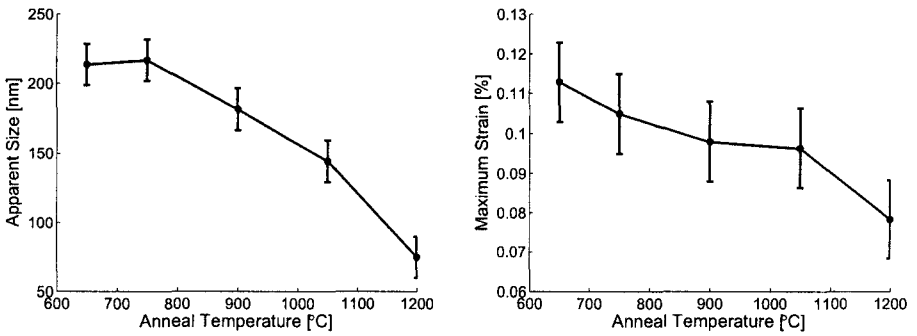

Figure 4.12: Apparent size (left) and microstrain (right) for a-SOI annealed for 10 minutes calculated using the Hall-Williamson method. Line drawn to guide eye.

4.5 Positron Annihilation Spectroscopy

4.5.1 Background

Positron annihilation spectroscopy (PAS) is used to study defects for bulk, surface and thin film applications. It is non-destructive and is particularly well-suited for vacancy-type defect studies. Depending on the technique used it can give the concentration, type and a depth profile of the present defects.

The technique requires the generation of a positron (the antiparticle of the electron) usually through the radio-active decay of ^{22}Na. This isotope is commonly used for its high yield, long half-life, low-cost and relatively safe handling requirements. The generated positrons have a broad energy spectrum, with a maximum energy of ~540 keV. Similar to ion implantation, the energetic positrons penetrate into the target to an average depth dependent on their energy. The implantation profile is

commonly described using a Makhovian distribution given by [143]

$$P(z,E) = \frac{mz^{m-1}}{z_0^m}\left(\exp\left(\frac{z}{z_0}\right)^m\right) \tag{4.15}$$

where z is the penetration depth, E is the positron energy, m is a fitting parameter commonly accepted to be 2 for silicon and z_0 is related to the average penetration depth, $\overline{z}$, and is given by [143]

$$z_0 = \frac{\overline{z}}{\Gamma(\frac{1}{m}+1)} \tag{4.16}$$

where Γ is the gamma function. This gives $z_0 = 1.11\overline{z}$. For silicon, the mean depth (given in nm's) can be related to the positron energy via [143]

$$\overline{z} = \frac{40}{\rho}E^{1.6} \tag{4.17}$$

where ρ is the material density. Since the gathered information is related to the depth and distribution of the injected positrons, depth profiling can be achieved by using a mono-energetic positron beam. This technique is commonly called variable energy positron annihilation spectroscopy (VEPAS) [28]. The mono-energetic beam is created by using a moderator, such as tungsten or nickel, in which injected positrons that thermalize and diffuse to the surface are ejected with a lower, but much sharper spectrum (~1 eV wide). The slow positrons can be accelerated to the desired energy and the implantation depth can vary depending on that energy as described by equation 4.17.

An injected positron randomly scatters until enough energy is lost to bring it into thermal equilibrium. This process takes place on the order of picoseconds. Once thermalized, the positron diffuses in the bulk, with a diffusion length dependent on the sample crystal quality (~200 nm for undefected silicon), until it annihilates with an

electron. The total energy released in this process is $2m_0c^2$=1022 keV, where m_0 is the electron mass and c is the speed of light. This typically takes the form of two γ-rays of energy 511 keV emitted in opposite directions. Due to momentum conservation, the emitted γ-rays are shifted in energy by $\Delta E = \pm\frac{cp}{2}$, where p is the momentum component of the positron-electron pair along the emission direction. This leads to a broadening of the emitted γ-ray profile around 511 keV, which is directly related to the momentum of the annihilated electron. This technique is called the Doppler broadening method [28].

Characterization of vacancy-type defects is particularly well-suited for PAS since positrons are naturally attracted to a vacancy. This is due to the lack of a repulsive energy from a positively charged ion core [28]. The broadened spectrum then reflects the momentum of the annihilated electrons surrounding the defect site. Although not used in this work, defects can also be monitored using the positron lifetime since the probability of annihilation is lower near a vacancy, and hence the average lifetime is longer.

After numerous annihilation events, an accurate representation of the γ-ray spectrum is obtained. The resulting spectrum is then described using S and W parameters. The S parameter represents the sharpness or low-momentum proportion of the distribution, while the W parameter represents the high-momentum region or wings. These parameters are schematically shown in figure 4.13. The S and W parameter are defined as [144]

$$S = \frac{A_S}{A_0} \qquad\qquad W = \frac{A_W}{A_0} \tag{4.18}$$

where A_S is the area of the low-momentum region (Region S in figure 4.13), A_W is the area of the high-momentum region (Region W in figure 4.13), and A_0 is the area

of the entire curve. The extent of each region, in terms of energy, is usually chosen so that $S{\sim}0.5$ and the energy windows used to define W are far enough away from those defining S such that there is no correlation between the two parameters.

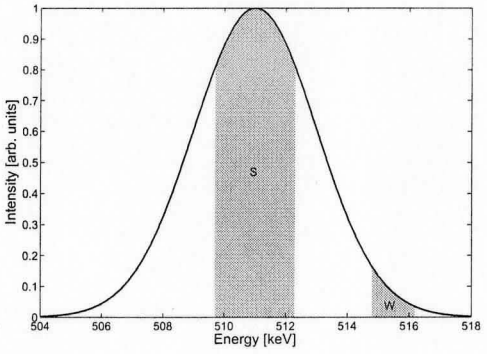

Figure 4.13: Schematic of a Doppler broadened positron measurement along with the areas used for S and W parameter extraction.

4.5.2 Experimental Results

Nine samples of 1.5 μm SOI, $\sim$1$\times$1 cm in size, were prepared using the previously described cleaning techniques. One sample was taken aside to act as a reference sample. Four samples were masked with a thick PECVD oxide, while the other four were not. The eight samples were implanted using REC-4 to amorphize the entire Si overlayer in the unmasked samples. The oxide was then removed and samples were annealed for 10 minutes at 550, 650 and 750 °C. One sample of both masked and unmasked varieties were annealed simultaneously at each temperature to ensure identical thermal histories. One sample from each group was not annealed to provide an as-implanted case. Variable energy positron annihilation spectroscopy was performed at the University of Bath using positron energies ranging from 0.5-30 keV.

From a PAS point of view, the *poly*-Si used in this work is very interesting. Since PAS data is dependent on both the system and fitting procedure used, the absolute

magnitude of the measured S and W parameters are often physically meaningless. To allow for physical interpretation of the data, a standard sample (e.g. high-quality, crystalline silicon) is measured and compared with. This makes interpretation of *poly*-Si measurements extremely difficult and unreliable since a *poly*-Si standard does not exist. By using *poly*-Si formed on SOI via amorphization and regrowth, the bare SOI can act as a standard. Although SOI may not be as defect-free as a bare Si wafer, it still provides a useful comparison and allows for better interpretation of the results.

Figures 4.14 and 4.15 show the measured S parameter for masked (regrown c-Si) and unmasked (*poly*-Si) samples. Also shown is the spectrum for intrinsic SOI, while the dashed line indicates the energy corresponding to the implantation depth consistent with the Si/buried oxide interface. For the masked samples, it is expected that following the 650 and 750 °C anneals, regrowth of c-Si should occur, whereas for the 550 °C annealed sample, some amorphous material should remain. This is clearly visible in figure 4.14 where the S parameter of the high temperature samples fall well below that of the as-implanted and 550 °C samples. The as-implanted case had a maximum S parameter of 1.06. This is higher than the reported value of 1.0391 and 1.0249 for as-implanted and relaxed a-Si and likely represents the clustering of open-volume defects in the vacancy-rich region of the defect profile (see figure 2.2) [144]. The measured difference in S parameter for the as-implanted and the 550 °C sample is 0.0141, which is virtually identical to the reported 0.0142 difference between as-implanted and relaxed a-Si [144].

For the case of the unmasked samples, the S parameter reflects the properties of *poly*-Si. XRD was used to confirm the presence (or absence) of *poly*-Si which was shown to be evident in the 650 and 750 °C samples but not in the 550 °C. Regardless, all 3 annealed samples exhibited a similar S parameter for positrons implanted to a

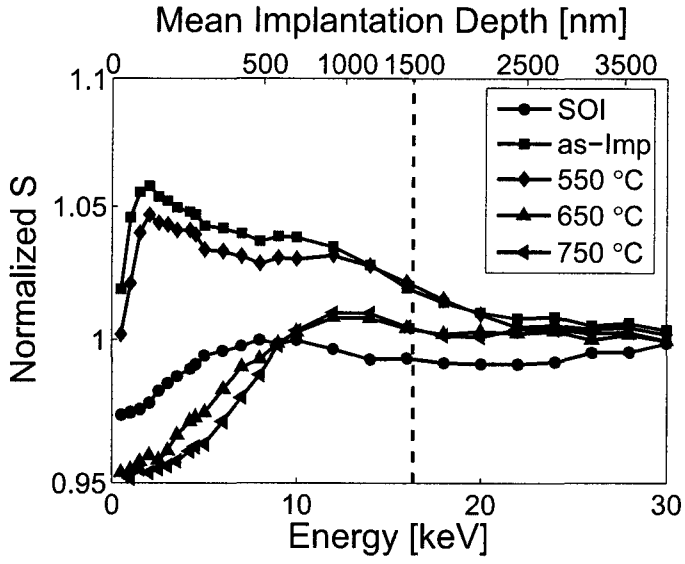

Figure 4.14: Normalized S parameter vs. energy for masked (regrown c-Si) samples. Also shown is the mean, positron penetration depth and the position of the buried oxide.

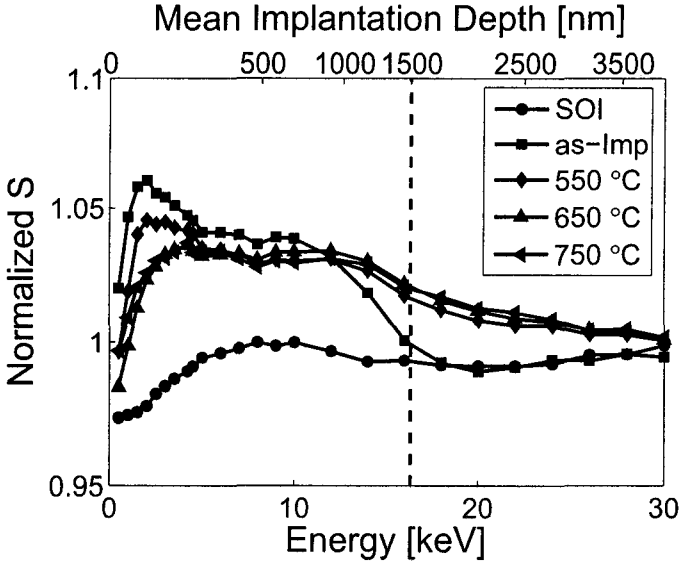

Figure 4.15: Normalized S parameter vs. energy for unmasked (*poly*-Si) samples. Also shown is the mean, positron penetration depth and the position of the buried oxide.

depth where no interaction with the surface takes place. The S parameter for the *poly*-Si was 1.036. This high S value possibly indicates that the grain boundaries are composed of a large number of vacancy-type defects. The large number of defects is

a good indication of a material with a low free carrier lifetime.

For the regrown (masked) samples, the S parameter actually falls below that of SOI for the lowest positron implantation energies. This is similar to the results of Xu *et al.* [97]. Lower S values have previously been associated with oxygen impurity complexes, in his case possibly incorporated during the implant or in the anneal, and originating from the native oxide.

4.6 Waveguide Measurements

The background information regarding optical waveguides and the implications of incorporating a-Si close to the waveguide core have been thoroughly discussed in chapters 2 and 3.

Waveguides were created using 2.5 μm SOI and a standard, silicon fabrication procedure (see Ref. [122]). The intended waveguide dimensions were $W = 3.0$, $H = 2.5$ and $h = 2.0$. These dimensions ensure single-mode behaviour based on equation 2.32. Device dimensions were chosen based on the available SOI and photolithography mask.

For this project an attempt was made to create a novel fabrication process for the *in-fab* integration of optical quality facets for SOI waveguides using the Alcatel reactive ion etcher. Success of this approach would provide significant fabrication advantages over the standard chip thinning and cleaving process currently used for facet preparation by the McMaster Silicon Photonics group. An example of an etched end facet structure is shown in figure 4.16. The facets were patterned after the waveguide itself was etched. Vertical etching of the facet was done using a Bosch-based process, for which the buried oxide acts as an etch stop. After etching, the sample was diced using the Loadpoint Microace dicing saw creating a ledge of a few

microns in width. As seen in figure 4.16 the etched surface of the facet is smooth and vertical however there is an indentation at the waveguide edges. This effect is likely caused during the photolithographical definition of the facet, which takes place on a non-uniform surface. Coupling light into this structure proved impossible. To circumvent this problem, it is possible that a thicker photoresist could be used to effectively planarize the surface. Etching could then be performed in two steps, between which the buried oxide is removed with an HF acid to avoid using the dicing saw. Although the use of this technique failed, it is reported here to aid any future attempts at forming an etch process for facet fabrication. In view of the failure of the etch process, all facets in this work were fabricated by the cleaving of thinned samples.

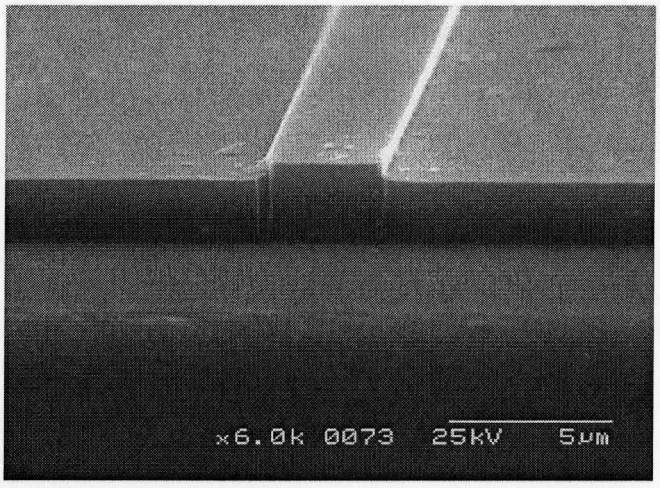

Figure 4.16: Example of an etched facet prepared using a single etch step followed by a dicing saw cut.

Three samples were prepared to measure i) the absorption of the regrown *poly*-Si ii) the loss due to adjacent *poly*-Si iii) the loss due to an *a*-Si surface layer. These will be referred to as WG-1-EXP, WG-2-EXP and WG-3-EXP respectively.

WG-1-EXP was prepared by creating standard rib waveguides followed by an ion

implantation step using REC-6 to amorphize the 2.5 μm silicon overlayer. A simple, tinfoil mask was used (placed diagonally across the sample) to create *poly*-Si regions of various lengths. Actual implanted lengths were measured afterwards using an optical microscope. The sample was then annealed at 300, 550, 650, 750 and 900 °C for 10 minutes. X-ray diffraction was used to confirm the presence of *poly*-Si.

The experimental setup for waveguide measurement has been detailed elsewhere (see Ref. [145] or [146]) and only a brief description follows. A diode laser, set at 1550 nm, was coupled into a tapered fiber and butt coupled to the sample. A 20× objective was used to collect the emitted light and was measured with an InGaAs detector. Polarization was controlled and monitored using stress inducing, polarization paddles and a polarization beam splitting cube. An infrared camera was used to monitor the output mode profile.

For WG-1-EXP (*poly*-Si absorption measurement), coupled light was first apparent after the the 650 °C anneal. The observed output was multimodal in nature when the direction of propagation was from *c*-Si to *poly*-Si, however for propagation from *poly*-Si to *c*-Si, a single-mode profile was obtained. This is shown in figure 4.17. This surprising phenomenon is thought to be caused by scattering at the Si/*poly*-Si interface and/or the relatively rough, cleaved *poly*-Si facet.

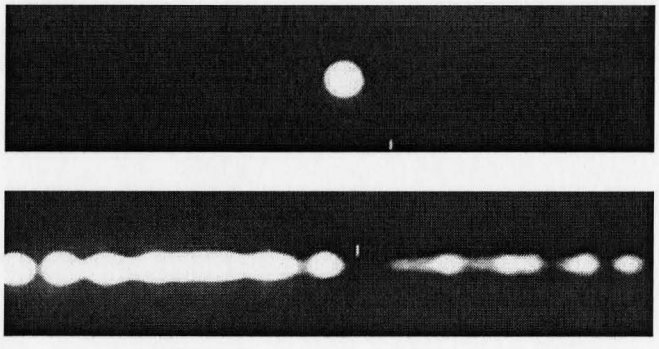

Figure 4.17: Output image when light is propagating from *poly*-Si to Si (top) and from Si to *poly*-Si.

Regardless of the poor output profile, optical loss measurements were made using the single-mode direction (i.e *poly*-Si to Si) after the 900 °C anneal. This is not the ideal condition since mode coupling takes place in the region under investigation (i.e. the *poly*-Si). Simulation of this scenario was performed using BeamPROP by launching a Gaussian-profiled source into a rib waveguide (of equal dimensions to the experimental waveguide) assuming the silicon overlayer had an absorption constant greater than zero. An exponential fit was done to the data in the region between 2500 and 7500 μm (approximately equal to the range of the actual *poly*-Si regions). The results suggest that in this configuration the measured optical loss would be $\sim 3.2\times$ higher than the actual absorption coefficient of the material itself.

The measured results are shown in figure 4.18 and a linear best fit gives a loss of 3.36 and 5.01 dB/cm for TM and TE polarizations. Assuming the simulation is correct, the actual optical loss of the *poly*-Si is 1.05 and 1.57 dB/cm for TM and TE respectively. Regardless of the experimental error and the absolute result, the optical absorption for this *poly*-Si is much less than *a*-Si and is comparable with values that are commonly used in silicon photonic applications. This is an encouraging result for potential applications of *poly*-Si.

To measure the optical loss due to adjacent *poly*-Si regions (WG-2-EXP), a ~640 nm SiO_2 film was deposited on predefined waveguide structures. Windows, placed on either side of the waveguide and located 3, 5, 8, 10, 15, 20 μm away from the rib edge, were patterned and etched. REC-5 was used to amorphize the 2.0 μm slab region and the sample was annealed at 650 °C for 10 minutes. Again, X-ray diffraction was used to confirm *poly*-Si formation. Optical loss measurements were taken and yielded no dependence of loss on *poly*-Si proximity. Based on the results of sections 4.2 and 4.3, lateral regrowth of *c*-Si should have exceeded 2.5 μm and the refractive index of the *poly*-Si is approximately that of *c*-Si, therefore the impact of an adjacent *poly*-Si

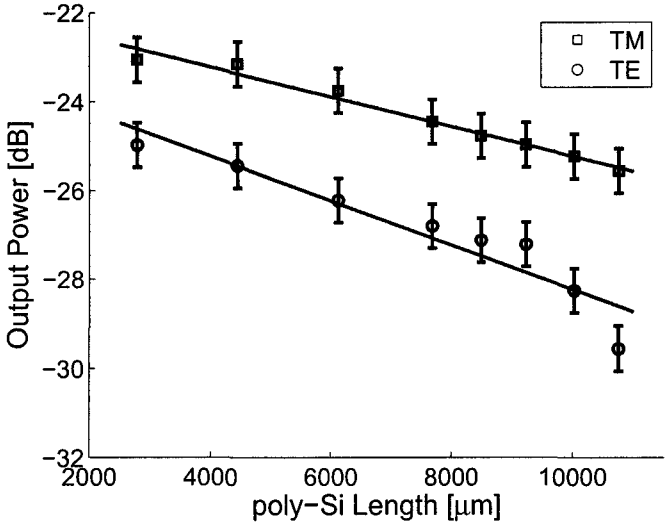

Figure 4.18: Measured output power for waveguides with various *poly*-Si lengths. Line represents best-fit.

region at least 5.5 μm away from the rib is predictably negligible. Again, this is encouraging for application of carrier lifetime control in silicon photonics.

WG-3-EXP was used to measure the optical loss of a surface amorphous layer. Predefined waveguides were masked with a ~605 nm oxide and patterned with implant windows, centered over the rib, of various lengths ranging from 2000-12000 μm. Samples were implanted using REC-2 to create an estimated 771 nm of *a*-Si. Annealing was done at 550 °C in 5 minute intervals for a total of 30 minutes, followed by a 650 °C anneal for 5 minutes.

Optical measurements were taken after each annealing step. Waveguide coupling was first observed after 10 minutes of annealing. It was multimodal and remained so until the sample had been annealed for 20 minutes. The optical absorption after each anneal stage is shown in figure 4.19. It is difficult to estimate the amount of *a*-Si remaining after each anneal step, however, based on the low optical loss, it is probable that the amorphous region regrew completely after 20 minutes of annealing.

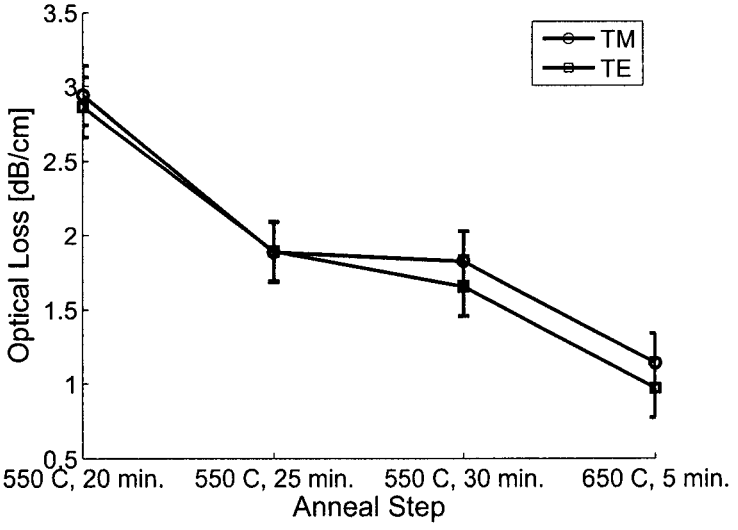

Figure 4.19: Optical absorption at various annealing stages due to persisting defects after the a-Si layer is regrown. Line drawn to guide eye.

The associated loss is therefore attributed to persisting defects below the original c/a interface and those within the regrown region. Longer annealing times and higher temperatures reduce defect concentration and in turn reduce optical absorption.

Chapter 5

Conclusions and Future Work

This work has shown the versatility of defect engineering for silicon photonic applications with an emphasis on amorphous and polycrystalline silicon. Simulations have shown that ion implantation induced *a*-Si is an excellent means to reduce free carrier lifetime in a silicon rib waveguide. For silicon Raman laser applications, this requires the *a*-Si to be limited to remote volumes to minimize the optical impact of the defected regions. This work has been simulation based and future work should focus on fabricating and testing this design. For optimal free carrier lifetime, both defect engineering and an integrated *p-i-n* diode could be used.

The experimental portion of this thesis was devoted to characterizing the properties of solid-phase epitaxial regrowth suppressed *poly*-Si. The properties of this *poly*-Si are governed by the annealing conditions; allowing for a wide range of applications depending on whether optical, electrical or structural optimization is needed.

Much of this characterization work has been preliminary and gives future researchers a parameter set and variable ranges with which to work. Ellipsometry, positron annihilation spectroscopy and x-ray diffraction techniques have been used. The optical properties of annealed *poly*-Si closely resemble those of *c*-Si, while the

defect concentration remains high due to persisting grain boundary defects. Structurally, the grain size and strain within the film have been shown to decrease with higher annealing temperatures. Fundamental studies of *poly*-Si regarding grain nucleation and growth, free carrier lifetime and refractive index modification should be performed to thoroughly characterize this material under a wide variety of annealing conditions.

Application of regrown *poly*-Si to rib waveguide applications requires careful consideration of lateral regrowth. Defect etching has shown that the annealing conditions will have direct implications on the position of the *c*-Si/*poly*-Si interface. Alignment of rib waveguides or any other structure with respect to the crystallographic orientation of the SOI substrate determines the quality and possible facet formation of the regrown *c*-Si. For low lifetime applications, it is preferable to orient the waveguides along the [011] direction since lateral regrowth consists of highly defective (111) facets. The number of processing steps can be reduced from those used in this work since the height difference between core and slab regions will guarantee a crystal seed if implant conditions are properly chosen therefore eliminating implant masking.

Besides free carrier lifetime engineering, several direct applications of this novel *poly*-Si material to silicon photonics are plausible. Stress-based engineering techniques for birefringence modification and optical modulators have recently been demonstrated [147][148]. The variable stress levels in the *poly*-Si potentially allow for such devices. A second potential application exists with the creation of silicon nanocrystals. Since grain boundaries enhance diffusion, oxidation or high dose oxygen ion implantation of small grained *poly*-Si could result in the production of nanocrystals in a SiO_2 matrix via the consumption of silicon grains in the oxidation process. If coupled with grain nucleation enhancement techniques, this could give a high-density, uniform nanocrystal distribution that could easily be integrated into silicon photonic

devices.

The results of this project have demonstrated the promising potential for SPER suppressed *poly*-Si and the application of defect engineering towards silicon photonic devices. The expected low free carrier lifetime of this novel *poly*-Si, coupled with optical properties similar to *c*-Si, make this material an ideal means to reduce free carrier lifetime. While the time for mainstream integration of silicon photonics into the microelectronics, telecommunication and biomedical industries rapidly approaches, it should be remembered that many silicon photonic specific fabrication techniques are in their infancy. The need for continuous innovation, invention and improvement is essential to make use of the increased bandwidth, reduced cost and increased systems integration that silicon photonics potentially provides. Defect engineering serves these purposes, allowing both the creation of new devices or the enhancement of old ones, making it a versatile technology that will likely be a mainstay for future silicon photonic applications.

Bibliography

[1] Miller, "An introduction to integrated optics," *Bell Systems Technical Journal*, vol. 67, no. 11, p. 1253, 1969.

[2] G. T. Reed and A. P. Knights, *Silicon Photonics: An Introduction.* John Wiley and Sons, Ltd., 2004.

[3] K. Izumi, M. Doken, E. Yamamoto, and Y. Irita, "Completely isolated CMOS ICs fabricated by oxygen ion implantation technique called 'SIMOX'," *Transactions of the Institute of Electronics and Communication Engineers of Japan Section E*, vol. E62, no. 12, pp. 921–922, 1979.

[4] M. Bruel, B. Aspar, B. Charlet, C. Maleville, T. Poumeyrol, A. Soubie, A. Auberton-Herve, J. Lamure, T. Barge, F. Metral, and S. Trucchi, "Smart Cut: a promising new soi material technology," *IEEE International SOI Conference*, pp. 178–179, 1995.

[5] J. B. Lasky, "Wafer bonding for silicon-on-insulator technologies," *Applied Physics Letters*, vol. 48, no. 1, pp. 78–80, 1986.

[6] G. K. Celler and S. Cristoloveanu, "Frontiers of silicon-on-insulator," *Journal of Applied Physics*, vol. 93, no. 9, pp. 4955–4978, 2003.

[7] SIA, "International technology roadmap for semiconductors - 2006 update," 2006.

[8] "http://www.kotura.com/."

[9] "http://www.enablence.com/."

[10] "http://www.luxtera.com/."

[11] K. Solehmainen, T. Aalto, J. Dekker, M. Kapulainen, M. Harjanne, K. Kukli, P. Heimala, K. Kolari, and M. Leskela, "Dry-etchced silicon-on-insulator waveguides with low propagation and fiber-coupling losses," *Journal of Lightwave Technology*, vol. 23, no. 11, pp. 3875–3880, 2005.

[12] J. K. Doylend and A. P. Knights, "Design and simulation of an integrated fiber-to-chip coupler for silicon-on-insulator waveguides," *IEEE Journal of Selected Topics in Quantum Electronics*, vol. 12, no. 6, pp. 1363–1370, 2006. Part 2.

[13] A. S. Liu, L. Liao, D. Rubin, H. Nguyen, B. Ciftcioglu, Y. Chetrit, N. Izhaky, and M. Paniccia, "High-speed optical modulation based on carrier depletion in a silicon waveguide," *Optics Express*, vol. 15, no. 2, pp. 660–668, 2007.

[14] A. P. Knights, J. D. B. Bradley, S. H. Gou, and P. E. Jessop, "Silicon-on-insulator waveguide photodetector with self-ion-implantation-engineered-enhanced infrared response," *Journal of Vacuum Science and Technology A*, vol. 24, no. 3, pp. 783–786, 2006.

[15] V. Sih, S. B. Xu, Y. H. Kuo, H. S. Rong, M. Paniccia, O. Cohen, and O. Raday, "Raman amplification of 40 gb/s data in low-loss silicon waveguides," *Optics Express*, vol. 15, no. 2, pp. 357–362, 2007.

[16] V. Lehmann and U. Gosele, "Porous silicon formation - a quantum wire effect," *Applied Physics Letters*, vol. 58, no. 8, pp. 856–858, 1991.

[17] L. Pavesi, L. Dal Negro, C. Mazzoleni, G. Franzo, and F. Priolo, "Optical gain in silicon nanocrystals," *Nature*, vol. 408, no. 6811, pp. 440–444, 2000.

[18] H. Park, A. W. Fang, O. Cohen, R. Jones, M. J. Paniccia, and J. E. Bowers, "A hybrid AlGaInAs-silicon evanescent amplifier," *IEEE Photonics Technology Letters*, vol. 19, no. 2-4, pp. 230–232, 2007.

[19] B. Jalali, V. Raghunathan, D. Dimitropoulos, and O. Boyraz, "Raman-based silicon photonics," *IEEE Journal of Selected Topics in Quantum Electronics*, vol. 12, no. 3, pp. 412–421, 2006.

[20] L. Liao, A. S. Liu, D. Rubin, J. Basak, Y. Chetrit, H. Nguyen, R. Cohen, N. Izhaky, and M. Paniccia, "40 gbit/s silicon optical modulator for highspeed applications," *Electronics Letters*, vol. 43, no. 22, pp. 1196–1197, 2007.

[21] J. J. Saarinen, S. M. Weiss, P. M. Fauchet, and J. E. Sipe, "Optical sensor based on resonant porous silicon structures," *Optics Express*, vol. 13, no. 10, pp. 3754–3764, 2005.

[22] C. E. Png, S. T. Lim, E. P. Li, and G. T. Reed, "Tunable and sensitive bio-photonic waveguides based on photonic-bandgap microcavities," *IEEE Transactions on Nanotechnology*, vol. 5, no. 5, pp. 478–484, 2006.

[23] W. M. Bullis, "Current trends in silicon defect technology," *Materials Science and Engineering B-Solid State Materials for Advanced Technology*, vol. 72, no. 2-3, pp. 93–98, 2000.

[24] K. S. Jones, S. Prussin, and E. R. Weber, "A systematic analysis of defects in ion-implanted silicon," *Applied Physics A-Materials Science and Processing*, vol. 45, no. 1, pp. 1–34, 1988.

[25] O. Dokumaci, P. Rousseau, S. Luning, V. Krishnamoorthy, K. S. Jones, and M. E. Law, "Transmission electron-microscopy analysis of heavily as-doped, laser, and thermally annealed layers in silicon," *Journal of Applied Physics*, vol. 78, no. 2, pp. 828–831, 1995.

[26] F. D. Auret and P. N. K. Deenapanray, "Deep level transient spectroscopy of defects in high-energy light-particle irradiated Si," *Critical Reviews in Solid State and Materials Sciences*, vol. 29, no. 1, pp. 1–44, 2004.

[27] G. D. Watkins, "Defects in irradiated silicon - EPR and electron-nuclear double-resonance of interstitial boron," *Physical Review B*, vol. 12, no. 12, pp. 5824–5839, 1975.

[28] A. P. Knights and P. G. Coleman, "Recent advances in the application of slow positron beams to the study of ion implantation defects in silicon," in *Defects and Diffusion in Semiconductors*, vol. 183-1 of *Defect and Diffusion Forum*, pp. 41–52, Switzerland: Scitec Publications, 2000.

[29] V. Raineri, A. Battaglia, and E. Rimini, "Gettering of metals by He induced voids in silicon," *Nuclear Instruments and Methods in Physics Research Section B-Beam Interactions with Materials and Atoms*, vol. 96, no. 1-2, pp. 249–252, 1995.

[30] M. Y. Tsai and B. G. Streetman, "Recrystallization of implanted amorphous silicon layers - 1. electrical-properties of silicon implanted with BF^{2+} or $Si^{++}B^{+}$," *Journal of Applied Physics*, vol. 50, no. 1, pp. 183–187, 1979.

[31] R. Siemieniec, F. J. Niedernostheide, H. J. Schulze, W. Sudkamp, U. Kellner-Werdehausen, and J. Lutz, "Irradiation-induced deep levels in silicon for power device tailoring," *Journal of the Electrochemical Society*, vol. 153, no. 2, pp. G108–G118, 2006.

[32] M. Horiuchi and M. Tamura, "Bess: A source structure that fully suppresses the floating body effects in SOI CMOSFET's," *IEEE Transactions on Electron Devices*, vol. 45, no. 5, pp. 1077–1083, 1998.

[33] W. L. Ng, M. A. Lourenco, R. M. Gwilliam, S. Ledain, G. Shao, and K. P. Homewood, "An efficient room-temperature silicon-based light-emitting diode," *Nature*, vol. 410, no. 6825, pp. 192–194, 2001.

[34] J. D. B. Bradley, P. E. Jessop, and A. P. Knights, "Silicon waveguide-integrated optical power monitor with enhanced sensitivity at 1550 nm," *Applied Physics Letters*, vol. 86, no. 24, 2005. 241103.

[35] Y. Liu, C. W. Chow, W. Y. Cheung, and H. K. Tsang, "Helium implanted silicon waveguide photodetectors for optical power monitors," *Proceedings of Optical Fiber Communication Conference and Exposition*, 2006.

[36] Y. Liu and H. K. Tsang, "Nonlinear absorption and Raman gain in helium-ion-implanted silicon waveguides," *Optics Letters*, vol. 31, no. 11, pp. 1714–1716, 2006.

[37] M. Foerst, J. Niehusmann, T. Plotzing, J. Bolten, T. Wahlbrink, C. Moormann, and H. Kurz, "High-speed all-optical switching in ion-implanted silicon-on-insulator microring resonators," *Optics Letters*, vol. 32, no. 14, pp. 2046–2048, 2007.

[38] R. Claps, V. Raghunathan, D. Dimitropoulos, and B. Jalali, "Influence of nonlinear absorption on raman amplification in silicon waveguides," *Optics Express*, vol. 12, no. 12, pp. 2774–2780, 2004.

[39] H. S. Rong, R. Jones, A. S. Liu, O. Cohen, D. Hak, A. Fang, and M. Paniccia, "A continuous-wave Raman silicon laser," *Nature*, vol. 433, no. 7027, pp. 725–728, 2005.

[40] P. Townsend, P. J. Chandler, and L. Zhang, *Optical Effects of Ion Implantation.* Cambridge Studies in Modern Optics, New York: Cambridge University Press, 1994.

[41] J. D. Plummer, M. D. Deal, and P. B. Griffen, *Silicon VLSI Technology.* New York: Prentice-Hall, 2000.

[42] "http://www.srim.org/."

[43] K. Cho, W. R. Allen, T. G. Finstad, W. K. Chu, J. Liu, and J. J. Wortman, "Channeling effect for low-energy ion-implantation in Si," *Nuclear Instruments and Methods in Physics Research Section B-Beam Interactions with Materials and Atoms*, vol. 7-8, no. MAR, pp. 265–272, 1985.

[44] J. W. Corbett, *Solid State Physics Vol. 7.* New York: Academic Press, 1966.

[45] G. Dearnaley, *Ion Implantation.* Amsterdam: North-Holland Publishing Company, 1973.

[46] J. S. Williams, S. O. Kucheyev, H. H. Tan, J. Wong-Leung, and C. Jagadish, "Ion irradiation-induced disordering of semiconductors: defect structures and applications," *Philosophical Magazine*, vol. 85, no. 4-7, pp. 677–687, 2005. Sp. Iss. SI.

[47] D. J. Eaglesham, P. A. Stolk, H. J. Gossmann, and J. M. Poate, "Implantation and transient B-diffusion in Si - the source of the interstitials," *Applied Physics Letters*, vol. 65, no. 18, pp. 2305–2307, 1994.

[48] L. Pelaz, L. A. Marques, and J. Barbolla, "Ion-beam-induced amorphization and recrystallization in silicon," *Journal of Applied Physics*, vol. 96, no. 11, pp. 5947–5976, 2004.

[49] O. W. Holland, M. K. Elghor, and C. W. White, "Damage nucleation and annealing in Mev ion-implanted Si," *Applied Physics Letters*, vol. 53, no. 14, pp. 1282–1284, 1988.

[50] K. W. Wang, W. G. Spitzer, G. K. Hubler, and D. K. Sadana, "Ion-implantation of Si by C-12, Si-29, and Sn-120 - amorphization and annealing effects," *Journal of Applied Physics*, vol. 58, no. 12, pp. 4553–4564, 1985.

[51] S. Prussin, D. I. Margolese, and R. N. Tauber, "Formation of amorphous layers by ion-implantation," *Journal of Applied Physics*, vol. 57, no. 2, pp. 180–185, 1985.

[52] S. International, "Ssuprem3 user's manual," 2006.

[53] H. Cerva and G. Hobler, "Comparison of transmission electron-microscope cross-sections of amorphous regions in ion-implanted silicon with point-defect density calculations," *Journal of the Electrochemical Society*, vol. 139, no. 12, pp. 3631–3638, 1992.

[54] H. Cerva and K. H. Kusters, "Defect formation in silicon at a mask edge during crystallization of an amorphous implantation layer," *Journal of Applied Physics*, vol. 66, no. 10, pp. 4723–4728, 1989.

[55] L. A. Christel, J. F. Gibbons, and T. W. Sigmon, "Displacement criterion for amorphization of silicon during ion-implantation," *Journal of Applied Physics*, vol. 52, no. 12, pp. 7143–7146, 1981.

[56] J. R. Dennis and E. B. Hale, "Energy-dependence of amorphizing implant dose in silicon," *Applied Physics Letters*, vol. 29, no. 9, pp. 523–524, 1976.

[57] R. D. Goldberg, J. S. Williams, and R. G. Elliman, "Amorphization of silicon by elevated temperature ion irradiation," *Nuclear Instruments and Methods in Physics Research Section B-Beam Interactions with Materials and Atoms*, vol. 106, no. 1-4, pp. 242–247, 1995.

[58] A. F. Saavedra, J. Frazer, K. S. Jones, I. Avci, S. K. Earles, M. E. Law, and E. C. Jones, "Influence of the surface Si/buried oxide interface on extended defect evolution in silicon-on-insulator scaled to 300 Angstrom," *Journal of Vacuum Science and Technology B*, vol. 20, no. 6, pp. 2243–2247, 2002.

[59] M. H. Clark, K. S. Jones, T. E. Haynes, C. J. Barbour, K. G. Minor, and E. Andideh, "Effects of amorphizing species' ion mass on the end-of-range damage formation in silicon," *Applied Physics Letters*, vol. 80, no. 22, pp. 4163–4165, 2002.

[60] S. Adachi, *Optical Properties of Crystalline and Amorphous Semiconductors: Materials and Fundamental Principles.* Norwell: Kluwaer Academic Publishers, 1999.

[61] J. C. Bourgoin, J. F. Mornhange, and R. Berserman, "On amorphous layer formation in silicon by ion implantation," *Radiation Effects*, vol. 22, pp. 205–208, 1974.

[62] J. Narayan, D. Fathy, O. S. Oen, and O. W. Holland, "Atomic-structure of ion-implantation damage and process of amorphization in semiconductors," *Journal of Vacuum Science and Technology A-Vacuum Surfaces and Films*, vol. 2, no. 3, pp. 1303–1308, 1984.

[63] C. N. Waddell, W. G. Spitzer, J. E. Fredrickson, G. K. Hubler, and T. A. Kennedy, "Amorphous-silicon produced by ion-implantation - effects of ion mass and thermal annealing," *Journal of Applied Physics*, vol. 55, no. 12, pp. 4361–4366, 1984.

[64] D. F. Edwards and E. Ochoa, "Infrared refractive-index of silicon," *Applied Optics*, vol. 19, no. 24, pp. 4130–4131, 1980.

[65] C. M. Fortmann, E. L. Jaen, N. Hata, W. A. Anderson, and A. H. Mahan, "Hot-wire deposition of photonic-grade amorphous silicon," *Thin Solid Films*, vol. 395, no. 1-2, pp. 142–146, 2001.

[66] M. Fried and A. Vansilfhout, "Optical dispersion-relations in 2 types of amorphous-silicon using Adachi expression," *Physical Review B*, vol. 49, no. 8, pp. 5699–5702, 1994.

[67] J. H. Ho, C. L. Lee, T. F. Lei, and T. S. Chao, "Ellipsometry measurement of the complex refractive-index and thickness of polysilicon thin-films," *Journal of the Optical Society of America a-Optics Image Science and Vision*, vol. 7, no. 2, pp. 196–205, 1990.

[68] J. Mullerova, S. Jurecka, and P. Sutta, "Optical characterization of polysilicon thin films for solar applications," *Solar Energy*, vol. 80, no. 6, pp. 667–674, 2006.

[69] J. E. Fredrickson, C. N. Waddell, and W. G. Spitzer, "Effects of thermal annealing on the refractive-index of amorphous-silicon produced by ion-implantation," *Applied Physics Letters*, vol. 40, no. 2, pp. 172–174, 1982.

[70] M. J. A. de Dood, A. Polman, T. Zijlstra, and E. van der Drift, "Amorphous silicon waveguides for microphotonics," *Journal of Applied Physics*, vol. 92, no. 2, pp. 649–653, 2002.

[71] E. C. Baranova, V. M. Gusev, Y. V. Martynenko, C. V. Starinin, and I. B. Haibullin, "On silicon amorphization during different mass ion implantation," *Radiation Effects*, vol. 18, pp. 21–26, 1973.

[72] D. L. Wood and J. Tauc, "Weak absorption tails in amorphous semiconductors," *Physical Review B*, vol. 5, no. 8, pp. 3144–3151, 1972.

[73] U. Zammit, K. N. Madhusoodanan, M. Marinelli, F. Scudieri, R. Pizzoferrato, F. Mercuri, E. Wendler, and W. Wesch, "Optical absorption studies of ion-implantation damage in Si on sapphire," *Physical Review B*, vol. 49, no. 20, pp. 14322–14330, 1994.

[74] G. D. Cody, T. Tiedje, B. Abeles, B. Brooks, and Y. Goldstein, "Disorder and the optical-absorption edge of hydrogenated amorphous-silicon," *Physical Review Letters*, vol. 47, no. 20, pp. 1480–1483, 1981.

[75] R. A. Soref and B. R. Bennett, "Electrooptical effects in silicon," *IEEE Journal of Quantum Electronics*, vol. 23, no. 1, pp. 123–129, 1987.

[76] L. J. Cheng, J. C. Corelli, J. W. Corbett, and G. D. Watkins, "1.8, 3.3 and 3.9 bands in irradiated silicon: Correlations with the divacancy," *Physical Review*, vol. 152, no. 2, p. 761, 1966.

[77] W. Wesch, E. Glaser, G. Gotz, H. Karge, and R. Prager, "Correlation between structural defects and optical-properties in ion-implanted silicon," *Physica Status Solidi A-Applied Research*, vol. 65, no. 1, pp. 225–232, 1981.

[78] P. J. Foster, J. K. Doylend, P. Mascher, A. P. Knights, and P. G. Coleman, "Optical attenuation in defect-engineered silicon rib waveguides," *Journal of Applied Physics*, vol. 99, no. 7, 2006. 073101.

[79] H. J. Stein, F. L. Vook, D. K. Brice, J. A. Borders, and S. T. Picraux, "Infrared studies pf the crystallinity of ion implanted Si," *Radiation Effects*, vol. 6, p. 19, 1970.

[80] L. Liao, D. R. Lim, A. M. Agarwal, X. M. Duan, K. K. Lee, and L. C. Kimerling, "Optical transmission losses in polycrystalline silicon strip waveguides: Effects of waveguide dimensions, thermal treatment, hydrogen passivation, and wavelength," *Journal of Electronic Materials*, vol. 29, no. 12, pp. 1380–1386, 2000.

[81] N. Mott, *Conduction in Non-Crystalline Materials.* Oxford: Claredon Press, 1987.

[82] P. M. Fauchet, D. Hulin, R. Vanderhaghen, A. Mourchid, and W. L. Nighan, "The properties of free-carriers in amorphous-silicon," *Journal of Non-Crystalline Solids*, vol. 141, no. 1-3, pp. 76–87, 1992.

[83] P. A. Stolk, F. W. Saris, A. J. M. Berntsen, W. F. Vanderweg, L. T. Sealy, R. C. Barklie, G. Krotz, and G. Muller, "Contribution of defects to electronic, structural, and thermodynamic properties of amorphous-silicon," *Journal of Applied Physics*, vol. 75, no. 11, pp. 7266–7286, 1994.

[84] J. Y. W. Seto, "Electrical properties of polycrystalline silicon films," *Journal of Applied Physics*, vol. 46, no. 12, pp. 5247–5254, 1975.

[85] H. C. Card and E. S. Yang, "Electronic processes at grain-boundaries in polycrystalline semiconductors under optical illumination," *IEEE Transactions on Electron Devices*, vol. 24, no. 4, pp. 397–402, 1977.

[86] A. S. Grove, *Physics and Technology of Semiconductor Devices.* New York: Wiley, 1967.

[87] S. K. Ghandhi, *The Theory and Practice of Microelectronics.* New York: Wiley, 1968.

[88] F. Y. Meng, T. T. Sun, and R. Q. Cui, "Recombination properties of grain boundaries in polycrystalline silicon under illumination," *Semiconductor Science and Technology*, vol. 15, no. 9, pp. 926–930, 2000.

[89] T. Rudenko, A. Rudenko, V. Kilchytska, S. Cristoloveanu, T. Ernst, J. P. Colinge, V. Dessard, and D. Flandre, "Determination of film and surface recombination in thin-film SOI devices using gated-diode technique," *Solid-State Electronics*, vol. 48, no. 3, pp. 389–399, 2004.

[90] P. C. Yang and S. S. Li, "Measurements of film carrier lifetimes in silicon-on-insulator wafers by a contactless dual-beam optical modulation technique," *Applied Physics Letters*, vol. 61, no. 12, pp. 1408–1410, 1992.

[91] L. Csepregi, E. F. Kennedy, J. W. Mayer, and T. W. Sigmon, "Substrate-orientation dependence of epitaxial regrowth rate from Si-implanted amorphous Si," *Journal of Applied Physics*, vol. 49, no. 7, pp. 3906–3911, 1978.

[92] R. Drosd and J. Washburn, "Some observations on the amorphous to crystalline transformation in silicon," *Journal of Applied Physics*, vol. 53, no. 1, pp. 397–403, 1982.

[93] G. L. Olsen and J. A. Roth, "Kinetics of solid phase crystallization in amorphous silicon," *Material Science Reports*, vol. 3, p. 1, 1988.

[94] C. Licoppe and Y. I. Nissim, "Impurity-induced enhancement of the growth-rate of amorphized silicon during solid-phase epitaxy - a free-carrier effect," *Journal of Applied Physics*, vol. 59, no. 2, pp. 432–438, 1986.

[95] J. M. Poate, S. Coffa, D. C. Jacobson, A. Polman, J. A. Roth, G. L. Olson, S. Roorda, W. Sinke, J. S. Custer, M. O. Thompson, F. Spaepen, and E. Donovan, "Amorphous Si - the role of Mev implantation in elucidating defect and thermodynamic properties," *Nuclear Instruments and Methods in Physics Research Section B-Beam Interactions with Materials and Atoms*, vol. 55, no. 1-4, pp. 533–543, 1991.

[96] J. Narayan and O. W. Holland, "Solid-phase-epitaxial growth in ion-implanted silicon," *Physica Status Solidi A-Applied Research*, vol. 73, no. 1, pp. 225–236, 1982.

[97] J. Xu, E. G. Roth, O. W. Holland, A. P. Mills, and R. Suzuki, "Vacancy defects in solid-phase epitaxial grown layers of self-implanted Si," *Applied Physics Letters*, vol. 74, no. 7, pp. 997–999, 1999.

[98] M. Horiuchi, M. Tamura, and S. Aoki, "3-dimensional solid-phase-epitaxial regrowth from As^+-implanted Si," *Journal of Applied Physics*, vol. 65, no. 6, pp. 2238–2242, 1989.

[99] H. Ishiwara, H. Yamamoto, S. Furukawa, M. Tamura, and T. Tokuyama, "Lateral solid-phase epitaxy of amorphous Si films on Si substrates with SiO_2 patterns," *Applied Physics Letters*, vol. 43, no. 11, pp. 1028–1030, 1983.

[100] H. Yamamoto, H. Ishiwara, and S. Furukawa, "On the mechanisms of lateral solid-phase epitaxial-growth of amorphous Si films evaporated on SiO_2 patterns," *Japanese Journal of Applied Physics Part 1-Regular Papers Short Notes and Review Papers*, vol. 24, no. 4, pp. 411–415, 1985.

[101] H. Cerva and W. Bergholz, "Implantation defects below mask edges in silicon - structure and effect on device," *Journal of the Electrochemical Society*, vol. 140, no. 3, pp. 780–786, 1993.

[102] Y. Kunii, M. Tabe, and K. Kajiyama, "Amorphous-Si crystalline-Si facet formation during Si solid-phase epitaxy near Si/SiO_2 boundary," *Journal of Applied Physics*, vol. 56, no. 2, pp. 279–285, 1984.

[103] K. Kusukawa, M. Moniwa, E. Murakami, T. Warabisako, and M. Miyao, "Grown-facet-dependent characteristics of silicon-on-insulator by lateral solid-phase epitaxy," *Applied Physics Letters*, vol. 52, no. 20, pp. 1681–1683, 1988.

[104] M. Horiuchi and M. Tamura, "Lateral SPE recovery of implanted source/drain in thin SOI MOSFETs," in *Proceedings of the International Conference on Ion Implantation Technology*, vol. 1, (Kyoto, Jpn), pp. 14–17, IEEE, Piscataway, NJ, USA, 1999.

[105] T. Warabisako, T. Tokuyama, M. Tamura, and M. Miyao, "Seeded lateral epitaxy in silicon-on-insulator structures," *Journal of Vacuum Science and Technology A-Vacuum Surfaces and Films*, vol. 5, no. 4, pp. 1393–1394, 1987. Part 2.

[106] C. Spinella, S. Lombardo, and F. Priolo, "Crystal grain nucleation in amorphous silicon," *Journal of Applied Physics*, vol. 84, no. 10, pp. 5383–5414, 1998.

[107] H. Kumomi and T. Yonehara, "Selective nucleation-based epitaxy (sentaxy): A novel approach for thin film formation," *Japanese Journal of Applied Physics Part 1-Regular Papers Short Notes and Review Papers*, vol. 36, no. 3B, pp. 1383–1388, 1997.

[108] M. J. Adams, *An Introduction to Optical Waveguides.* New York: John Wiley and Sons, 1981.

[109] R. A. Soref, J. Schmidtchen, and K. Petermann, "Large single-mode rib waveguides in GeSi-Si and Si-on-SiO_2," *IEEE Journal of Quantum Electronics*, vol. 27, no. 8, pp. 1971–1974, 1991.

[110] S. P. Pogossian, L. Vescan, and A. Vonsovici, "The single-mode condition for semiconductor rib waveguides with large cross section," *Journal of Lightwave Technology*, vol. 16, no. 10, pp. 1851–1853, 1998.

[111] R. Knox and P. Toulios, "Integrated circuits for the millimeter through optical frequency range," in *Symposium on submillimetre waves*, pp. 497–516, Polytechnic Press, New York, NY, USA, 1970.

[112] M. D. Feit and J. A. Fleck, "Light-propagation in graded-index optical fibers," *Applied Optics*, vol. 17, no. 24, pp. 3990–3998, 1978.

[113] A. Anderson, *The Raman Effect.* New York: Marcel Dekker, 1971.

[114] M. Cardona, *Light Scattering in Solids.* New York: Springer-Verlag, 1983.

[115] A. S. Liu, H. S. Rong, R. Jones, O. Cohen, D. Hak, and M. Paniccia, "Optical amplification and lasing by stimulated Raman scattering in silicon waveguides," *Journal of Lightwave Technology*, vol. 24, no. 3, pp. 1440–1455, 2006.

[116] G. P. Agrawal, *Nonlinear Fiber Optics*. New York: Academic, 2nd ed., 1995.

[117] O. Boyraz and B. Jalali, "Demonstration of a silicon Raman laser," *Optics Express*, vol. 12, no. 21, pp. 5269–5273, 2004.

[118] D. Dimitropoulos, S. Fathpour, and B. Jalali, "Limitations of active carrier removal in silicon Raman amplifiers and lasers," *Applied Physics Letters*, vol. 87, no. 26, 2005. 261108.

[119] D. Dimitropoulos, R. Jhaveri, R. Claps, J. C. S. Woo, and B. Jalali, "Lifetime of photogenerated carriers in silicon-on-insulator rib waveguides," *Applied Physics Letters*, vol. 86, no. 7, 2005. 071115.

[120] A. S. Liu, H. S. Rong, and M. Paniccia, "Net optical gain in a low loss silicon-on-insulator waveguide by stimulated Raman scattering," *Optics Express*, vol. 12, no. 18, pp. 4261–4268, 2004.

[121] R. A. Soref and J. P. Lorenzo, "All-silicon active and passive guided-wave components for λ=1.3 and 1.6 μm," *IEEE Journal of Quantum Electronics*, vol. 22, no. 6, pp. 873–879, 1986.

[122] J. D. B. Bradley, "Integrated optical power monitors with enhanced infrared response in silicon-on-insulator waveguides," Master's thesis, McMaster University, 2005.

[123] D. Blakie, "Coupled luminescence centres in erbium-doped silicon rich silicon oxide thin films deposited by ecr-pecvd," Master's thesis, McMaster University, 2006.

[124] B. O. Kolbesen, W. Bergholz, H. Cerva, B. Fiegl, F. Gelsdorf, and G. Zoth, "Process-induced defects in VLSI," *Nuclear Instruments and Methods in Physics Research Section B-Beam Interactions with Materials and Atoms*, vol. 55, no. 1-4, pp. 124–131, 1991.

[125] W. C. Dash, "Copper precipitation on dislocations in silicon," *Journal of Applied Physics*, vol. 27, no. 10, p. 1193, 1956.

[126] M. W. Jenkins, "New preferential etch for defects in silicon-crystals," *Journal of the Electrochemical Society*, vol. 124, no. 5, pp. 757–762, 1977.

[127] B. L. Sopori, "A new defect etch for polycrystalline silicon," *Journal of the Electrochemical Society*, vol. 131, no. 3, pp. 667–672, 1984.

[128] K. H. Yang, "An etch for delineation of defects in silicon," *Journal of the Electrochemical Society*, vol. 131, no. 5, pp. 1140–1145, 1984.

[129] F. S. d'Aragona, "Dislocation etch for (100) planes in silcon," *Journal of the Electrochemical Society*, vol. 119, no. 7, p. 948, 1972.

[130] E. Murakami, M. Moniwa, K. Kusukawa, M. Miyao, T. Warabisako, and Y. Wada, "Seed shape dependence of si solid-phase epitaxy - preferential facet growth," *Journal of Applied Physics*, vol. 63, no. 10, pp. 4975–4978, 1988.

[131] C. R. Olson, E. Kuryliw, B. E. Jones, and K. S. Jones, "Effect of stress on the evolution of mask-edge defects in ion-implanted silicon," *Journal of Vacuum Science and Technology B*, vol. 24, no. 1, pp. 446–449, 2006.

[132] F. Pedrotti and L. Pedrotti, *Introduction to Optics, 2nd Ed.* New York: Prentice-Hall, 1993.

[133] G. M. Cohen, P. M. Mooney, H. Park, C. Cabral, and E. C. Jones, "High-resolution x-ray diffraction for characterization and monitoring of silicon-on-insulator fabrication processes," *Journal of Applied Physics*, vol. 93, no. 1, pp. 245–250, 2003.

[134] D. Comedi, O. H. Y. Zalloum, E. A. Irving, J. Wojcik, T. Roschuk, M. J. Flynn, and P. Mascher, "X-ray-diffraction study of crystalline Si nanocluster formation in annealed silicon-rich silicon oxides," *Journal of Applied Physics*, vol. 99, no. 2, 2006. 023518.

[135] D. Bisero, M. Dapor, and B. Margesin, "X-ray-diffraction study of p-doped polycrystalline Si thin-films used in ULSI devices," *Materials Letters*, vol. 14, no. 5-6, pp. 303–306, 1992.

[136] B. Cullity and S. R. Stock, *X-Ray Diffraction.* Upper Saddle River: Prentice-Hall, 2001.

[137] G. Lim, W. Parrish, C. Ortiz, M. Bellotto, and M. Hart, "Grazing incidence synchrotron x-ray diffraction method for analyzing thin films." *Journal of Materials Research*, vol. 2, no. 4, pp. 471–477, 1987.

[138] R. L. Snyder, J. Fiala, and H. Bunge, *Defect and Microstructure Analysis by Diffraction.* New York: Oxford University Inc., 1999.

[139] D. L. Williamson, "Microstructure of amorphous and microcrystalline Si and SiGe alloys using X-rays and neutrons," *Solar Energy Materials and Solar Cells*, vol. 78, no. 1-4, pp. 41–84, 2003.

[140] S. Boultadakis, S. Logothetidis, and S. Ves, "Comparative-study of thin poly-Si films grown by ion-implantation and annealing with spectroscopic ellipsometry, Raman-spectroscopy, and electron-microscopy," *Journal of Applied Physics*, vol. 72, no. 8, pp. 3648–3658, 1992.

[141] M. Morris, *Powder Diffraction Data.* Swarthmore: Joint Committee on Powder Diffraction Standards, 1976.

[142] B. Pivac, "High-temperature complex structures in solar-grade poly-Si," *Journal of Physics D-Applied Physics*, vol. 23, no. 1, pp. 53–55, 1990.

[143] P. Asoka-Kumar, K. G. Lynn, and D. O. Welch, "Characterization of defects is Si and SiO_2-Si using positrons," *Journal of Applied Physics*, vol. 76, no. 9, p. 4935, 1994.

[144] E. Ottewitte and A. H. Weiss, *Slow Positron Beam Techniques for Solids and Surfaces.* New York: American Institute of Physics, 1992.

[145] C. Brooks, "Polarization rotating waveguides in silicon-on-insulator," Master's thesis, McMaster University, 2005.

[146] M. Bulk, "Ion implanted bragg gratings in silicon-on-insulator rib waveguides," Master's thesis, McMaster University, 2008.

[147] W. N. Ye, D. X. Xu, S. Janz, P. Cheben, M. J. Picard, B. Lamontagne, and N. G. Tarr, "Birefringence control using stress engineering in silicon-on-insulator (SOI) waveguides," *Journal of Lightwave Technology*, vol. 23, no. 3, pp. 1308–1318, 2005.

[148] R. S. Jacobsen, K. N. Andersen, P. I. Borel, J. Fage-Pedersen, L. H. Frandsen, O. Hansen, M. Kristensen, A. V. Lavrinenko, G. Moulin, H. Ou, C. Peucheret, B. Zsigri, and A. Bjarklev, "Strained silicon as a new electro-optic material," *Nature*, vol. 441, no. 7090, pp. 199–202, 2006.